UNIVERSIDADE FEDERAL DO RIO GRANDE DO SUL INSTITUTO DE GEOCIÊNCIAS PROGRAMA DE PÓS-GRADUAÇÃO EM GEOCIÊNCIAS

AN OCEAN WIND-WAVE CLIMATOLOGY FOR THE SOUTHERN BRAZILIAN SHELF

Renato Oliveira Cecilio

Dissertation submitted in partial fulfillment of the requirements for the degree of Doctor of Science.

Supervisor: Prof. Dr. Sergio R. Dillenburg

UNIVERSIDADE FEDERAL DO RIO GRANDE DO SUL INSTITUTO DE GEOCIÊNCIAS PROGRAMA DE PÓS-GRADUAÇÃO EM GEOCIÊNCIAS

AN OCEAN WIND-WAVE CLIMATOLOGY FOR THE SOUTHERN BRAZILIAN SHELF

Renato Oliveira Cecilio

Supervisor: Prof. Dr. Sergio R. Dillenburg

Examining committee:

Prof. Dr. Ricardo de Camargo (IAG/USP)

Prof. Dr. Lauro Julio Calliari (IO/FURG)

Prof. Dr. Elirio E. Toldo Jr. (CECO/UFRGS)

UNIVERSIDADE FEDERAL DO RIO GRANDE DO SUL

Reitor: Carlos Alexandre Netto

Vice-Reitor: Rui Vicente Oppermann INSTITUTO DE GEOCIÊNCIAS

Diretor: André Sampaio Mexias

Vice-Diretor: Nelson Luiz Sambaqui Gruber

Cecilio, Renato Oliveira

An ocean wind-wave climatology for the Southern Brazilian Shelf . / Renato Oliveira Cecilio. - Porto Alegre: IGEO/UFRGS, 2015. [104 f.] il.

Tese (Doutorado).- Universidade Federal do Rio Grande do Sul. Graduação em Geografia. Instituto de Geociências. Porto Alegre, RS -BR, 2015.

Orientador(es):Sergio Rebello Dillenburg

1. Wave Modeling 2. Wave Climate 3. Shoreface 4. Antepraia I. Título.

CDU 911

Catalogação na Publicação Biblioteca Instituto de Geociências - UFRGS Sibila Francine T. Binotto CRB 10/1743

Universidade Federal do Rio Grande do Sul - Campus do Vale Av. Bento Gonçalves, 9500 - Porto Alegre - RS - Brasil CEP: 91501-970 / Caixa Postal: 15001.

Fone: +55 51 3308-6329 Fax: +55 51 3308-6337

E-mail: bibgeo@ufrgs.br

I dedicate this thesis to you, my reader, in the hope that it might help you to do some science.

Contents

| | RES | UMO | ix |
|---|------|-------------------------------------------|------|
| | ABS | STRACT | X |
| | PRE | FACE | xiii |
| 1 | Intr | oduction | 1 |
| 2 | Atm | ospheric conditions | 5 |
| | 2.1 | Mean Circulation | 5 |
| | 2.2 | Synoptic-scale winds | 10 |
| | 2.3 | Intraseasonal and interannual modulations | 16 |
| | 2.4 | Concluding remarks | 23 |
| 3 | Mod | lel description and validation | 24 |
| | 3.1 | Numerical models | 24 |
| | 3.2 | Experiments grids and settings | 25 |
| | 3.3 | Model validation | 27 |
| | | 3.3.1 Basin-scale | 27 |
| | | 3.3.2 Regional-scale | 36 |
| | 3.4 | Concluding remarks | 46 |
| 4 | Wav | ve variability in time and space | 50 |
| | 4.1 | Large-scale wave patterns | 50 |
| | 4.2 | SBS Offshore wave conditions | 61 |
| | 4.3 | SBS Shoreface wave conditions | 74 |
| | 4.4 | Concluding remarks | 86 |
| 5 | Con | clusion | 89 |
| 6 | Refe | erences | 90 |

List of Figures

| 1.1 | South America (left) and Southern Brazilian Shelf and Coastal Plain (right) reliefs. | 2 |
|------|--------------------------------------------------------------------------------------|----|
| 2.1 | Seasonal means of Long Term (1981-2010) mid-tropospheric (500 hPa) omega | |
| | and high-level (250 hPa) geopotential height contours | 6 |
| 2.2 | Seasonal means of Long Term (1981-2010) high-level (250 hPa) winds | 6 |
| 2.3 | Seasonal means of Long Term (1981-2010) precipitation rates and sea level | |
| | pressure | 7 |
| 2.4 | Seasonal means of Long Term (1981-2010) low-level (850 hPa) winds | 7 |
| 2.5 | Seasonal means of Long Term (1981-2010) low-level (850 hPa) winds over SBS | |
| | and SBCP | 11 |
| 2.6 | Seasonal means of Long Term (1981-2010) surface (10 m) winds over SBS and | |
| | SBCP | 11 |
| 2.7 | Hovmoller diagram in longitude/time domain of the six-hourly meridional 250 | |
| | hPa wind anomalies | 12 |
| 2.8 | Succession of sea level high and low pressure systems moving across South | |
| | America | 14 |
| 2.9 | Six-hourly zonal and meridional surface wind data during 2012 and its 40 days | |
| | low-passed series | 15 |
| 2.10 | Western South Atlantic cyclogenesis climatology reproduced from Reboita (2008). | 17 |
| 2.11 | Forty days low-passed series of six-hourly sea level pressure between 1990/2012 | |
| | and its 2 years low-passed series | 19 |
| 2.12 | Comparison between the SO index and the interannual signal at the extremities | |
| | of SBS | 20 |
| 2.13 | Amplitude variation of sea level pressure for individual synoptic-scale events | |
| | between 1990/2012 and its 90 days running means | 22 |
| 2.14 | Period of individual synoptic-scale events between 1990/2012 and its 90 days | |
| | running means | 22 |
| 3.1 | Bathymetric grids used in the simulations | 26 |
| 3.2 | Time series of daily mean sig. wave height for the north, central and south | |
| | portions of the shelf break of SBS | 29 |
| 3.3 | Annual mean of sig. wave height, modeled and observed | 30 |
| 3.4 | Annual mean absolute error and annual mean of relative absolute error | 31 |

| 3.5 | Time series of daily mean sig. wave height for the north, central and south por- | |
|------|-----------------------------------------------------------------------------------|----|
| | tions of the shelf break of SBS | 32 |
| 3.6 | Annual mean of sig. wave height, modeled and observed | 33 |
| 3.7 | Annual mean absolute error and annual mean of relative absolute error | 34 |
| 3.8 | Density scatter plot of daily mean sig. height for the north, central and south | |
| | portions of the shelf break of SBS | 35 |
| 3.9 | Density scatter plot of wave statistics between our simulations on the Shelf grid | |
| | versus the two observed wave-buoy datasets | 37 |
| 3.10 | Bidimensional diagrams of wave statistics comparing the dataset of Rio Grande | |
| | and our simulations on the Shelf grid | 39 |
| 3.11 | Bidimensional diagrams of wave statistics comparing the dataset of Tramandai | |
| | versus our simulations on the Shelf grid | 40 |
| 3.12 | Density scatter plot of sig. height with the four experiments ran on the Coastal | |
| | grid versus the two observed wave-buoy datasets | 42 |
| 3.13 | Density scatter plot of peak period with the four experiments ran on the Coastal | |
| | grid versus the two observed wave-buoy datasets | 43 |
| 3.14 | Density scatter plot of peak direction with the four experiments ran on the | |
| | Coastal grid versus the two observed wave-buoy datasets | 44 |
| 3.15 | Bidimensional diagrams of wave statistics for model results at Rio Grande, as | |
| | obtained in exp. 2 with wind grow and in exp. 4 without wind grow | 47 |
| 3.16 | Bidimensional diagrams of wave statistics for model results at Tramandai, as | |
| | obtained in exp. 2 with wind grow and in exp. 4 without wind grow | 48 |
| 4.1 | Long-term mean (1990-2012) of sig. height and peak period as obtained on the | |
| | S. Atlantic grid | 50 |
| 4.2 | Examples of wave patterns generated by the cyclogenesis centered at 27 °S | 52 |
| 4.3 | Examples of wave patterns generated by the cyclogenesis centered at 35 °S | 53 |
| 4.4 | Examples of wave patterns generated by the cyclogenesis centered at 48 °S | 54 |
| 4.5 | Two examples of post-frontal SE waves and one example of pre-frontal change | |
| | from ENE to N/NW waves. | 55 |
| 4.6 | Example of ENE wave patterns generated by the eastward moving high pressure | |
| | cell | 56 |
| 4.7 | Example of E/ESE waves patterns generated by the eastward moving high pres- | |
| | sure cell | 57 |
| 4.8 | Long-term SVD of daily mean sig. height and peak period as obtained on the | |
| | S. Atlantic grid (modes 1 to 3) | 58 |
| 4.9 | Long-term SVD of daily mean sig. height and peak period as obtained on the | |
| | S. Atlantic grid, after 20 days high-pass filtering (modes 1 to 3) | 59 |
| 4.10 | Long-term SVD of daily mean sig. height and peak period as obtained on the | |
| | S. Atlantic grid, after 20 days high-pass filtering (modes 4 to 6) | 60 |
| 4.11 | Southern Brazilian Shelf grid bathymetry (m) | 62 |

| 4.12 | Long-term (1990-2012) mean wave power spectrum at shelf-break | 63 |
|------|------------------------------------------------------------------------------|----|
| 4.13 | Long-term (1990-2012) mean wave power spectrum at mid-shelf | 64 |
| 4.14 | Long-term distribution (1990-2012) of the annual mean power spectrum, inte- | |
| | grated over frequencies, at shelf-break | 65 |
| 4.15 | Long-term distribution (1990-2012) of the annual mean power spectrum, inte- | |
| | grated over frequencies, at mid-shelf | 66 |
| 4.16 | Long-term distribution (1990-2012) of the annual mean power spectrum, inte- | |
| | grated over frequencies only between 30° and 120°, versus the SO index | 67 |
| 4.17 | Long-term distribution (1990-2012) of the monthly mean power spectrum, in- | |
| | tegrated over frequencies, at shelf-break | 68 |
| 4.18 | Long-term distribution (1990-2012) of the monthly mean power spectrum, in- | |
| | tegrated over frequencies, at mid-shelf | 69 |
| 4.19 | Intra-annual distribution of the six-hourly long-term (1990-2012) mean power | |
| | spectrum, integrated over frequencies, at shelf-break | 70 |
| 4.20 | Intra-annual distribution of the six-hourly long-term (1990-2012) mean power | |
| | spectrum, integrated over frequencies, at mid-shelf | 71 |
| 4.21 | Long-term (1990-2012) monthly mean maps of sig. wave height over the SBS. | 72 |
| 4.22 | Long-term (1990-2012) mean map of sig. wave height over the SBS | 73 |
| 4.23 | Curvilinear Coastal grid bathymetry (m) | 75 |
| 4.24 | Long-term (1990-2012) mean maps of sig. wave height over the SBS shoreface. | 77 |
| 4.25 | Long-term (1990-2012) mean maps of relative sig. wave height over the SBS | |
| | shoreface | 78 |
| 4.26 | Long-term (1990-2012) mean wave power spectrum at upper shoreface | 80 |
| 4.27 | Long-term distribution (1990-2012) of the annual mean power spectrum, inte- | |
| | grated over frequencies, at upper shoreface | 82 |
| 4.28 | Long-term distribution (1990-2012) of the annual mean power spectrum, inte- | |
| | grated over frequencies, at upper shoreface | 83 |
| 4.29 | Long-term distribution (1990-2012) of the monthly mean power spectrum, in- | |
| | tegrated over frequencies, at upper shoreface | 84 |
| 4.30 | Long-term distribution (1990-2012) of the monthly mean power spectrum, in- | |
| | tegrated over frequencies, at upper shoreface | 85 |

List of Tables

| 3.1 | Statistics of the time series comparison between observed and modeled sig. | |
|-----|----------------------------------------------------------------------------|----|
| | wave heights | 45 |
| 3.2 | Statistics of the time series comparison between observed and modeled peak | |
| | wave periods | 45 |
| 3.3 | Statistics of the time series comparison between observed and modeled peak | |
| | wave directions | 45 |

RESUMO

Inicialmente, expusemos como feições geomorfológicas e medições visuais de onda, apresentadas em trabalhos anteriores, apontam para a possível existência de gradientes de energia de onda ao longo da costa sobre a Plataforma Continental Sul (PCS). Examinamos também as condições atmosféricas da PCS e encontramos que oscilações intrasazonais podem não somente modular diretamente os ventos e a pressão como também indiretamente modular o período e amplitude dos eventos de escala sinótica. Uma boa correlação entre a pressão e o índice da oscilação sul foi encontrada em escala de tempo interanual, atestando a modulação pelo ENSO.

Em seguida, após descrever os dois modelos utilizados, as grades e as configurações, o presente estudo avaliou a validação dos resultados do modelo em escala de bacia versus a altimetria orbital e a validação dos resultados do modelo regional versus os dois dados de ondógrafo disponíveis sobre a PCS, discutindo o quanto o modelo reproduz a realidade local. Excluindose os erros localizados, os resultados de altura sig. do modelo WW3 na grade global e na grade do Atlântico Sul pode ser considerado como em muito boa concordância com as observações, apresentando semelhanças notáveis com os dados de altimetria. Em relação à modelagem regional, tanto a altura sig. quanto os períodos de pico como obtidos na grade de plataforma foram considerados como em boa concordância com as observações. As direções de pico, no entanto, foram classificados como pobre concordância. No entanto, as ondas de S ou SSE foram bem reproduzidas e são as ondas de ESE que foram erradamente representadas como E ou ENE pelo modelo. Os resultados na grade costeira também foram considerados como em muito bom acordo com observações para altura sig. e períodos de pico, mas apresentaram os mesmos conflitos sobre direções de pico. Acreditamos que essas ondas E ou ENE já foram produzidas de forma incorreta pelo modelo WW3 e em seguida transferidas através das condições de contorno. O aumento da resolução certamente desempenhou um papel e não pode ser descartada, uma vez que mostra melhores estatísticas e maior variabilidade dos resultados, mas foi a redução de atrito que representou a maior melhoria nas simulações da grade costeira curvilinear.

Por fim, utilizamos nossos resultados do modelo para mostrar como o bloqueio das ondas geradas pelos ventos de oeste pela América do Sul, caracterizando as plataformas do oeste do Atlântico Sul com um clima de ondas de baixa energia. Períodos de pico médios mais baixos foram encontrados sobre a PCS indicando duas regiões de geração de ondas. Em seguida, mostramos exemplos de ondas extremas induzidas por ciclones. Condições pré e pós-frontais particulares também foram mostradas para caracterizar as mudanças nas direções de onda em escala sinótica. Os espectros médios costa afora mostraram uma predominância das ondas S/SSW com um pico de energia secundária composta por ondas ENE/E, corroborando com a afirmação de que a PCS é essencialmente bimodal em direções de onda. A potência das ondas S/SSW diminui para o norte e das ondas ENE/E secundariamente diminui para o sul, o que nos permite afirmar que a PCS esta localizada entre a influência dos ventos de oeste e ciclones e a influência da Alta do Atlântico Sul. A distribuição interanual mostrou períodos distintos de ascensões da energia das ondas ENE/E e ESE, que são moduladas pelo ENSO. A distribuição intra-anual mostrou um núcleo de ondas S/SSW ocorrendo centrado no inverno entre abril e

setembro. Há também um núcleo ENE/E que ocorre durante as primaveras em oposição as potências mais baixas encontradas durante o inverno. Máximas ondas de SE ocorrem durante abril e maio e, secundariamente, durante a primavera e estão associadas com os ciclones.

Gradientes de energia de ondas junto à costa já são vistos na grade de plataforma, com maior energia localizada ao largo de ambos os cabos e da projeção costeira norte e apenas secundariamente ao largo da projeção costeira sul. Por outro lado, mínimo de energia é encontrado entre as projeções costeiras em Rio Grande e, secundariamente, entre os cabos e projeções costeiras. As declividades da plataforma média e externa não são refletidas nesse padrão de energia. Mais perto da costa, no entanto, em profundidades menores de 40 m o padrão de energia segue os contornos batimétricos após uma queda considerável da energia causada por atrito. Com base nestes resultados, sugere-se a profundidade de 40 m como o nível base de ondas dos dias de hoje e, consequentemente, o limite inferior da antepraia. O aumento da resolução na grade costeira permitiu-nos reconhecer que a energia das ondas possui uma relação mais direta com a largura da antepraia. Além disso, permitiu uma separação geomorfológica clara entre a enorme antepraia inferior e as maiores declividades da pequena antepraia superior e banco do Albardão. A energia das ondas na antepraia superior varia abruptamente ao longo da costa, diminuindo da metade norte para a metade sul, em uma relação clara com as declividades da plataforma média. Assim, a herança geológica expressa através da largura da antepraia e das declividades da plataforma média poderia ser mais importante para gerar variabilidade de onda do que as próprias variações de onda costa afora ao longo da costa.

Uma refração quase completa é observada entre os espectros bimodais costa afora e os espectros na antepraia superior que foram encontrados principalmente como ondas ESE/SSE com maior importância da onda SE e em um espectro quase unimodal. Esses resultados mostram como a grande e rasa antepraia da PCS é responsável por uma refração intensa das ondas, forçando-as a aproximar-se do sistema praial com pequenos ângulos de ataque. Além disso, a semelhança entre os espectros na antepraia superior indicou o efeito de abrigo causado pelos cabos e projeções costeiras e uma "janela de refração" sobre a propagação de ondas até a costa, uma vez que ondas normais à costa chegam com energia maior do que ondas em ângulo. Entre cabos e projeções costeiras, onde as energias de onda mais baixas foram encontradas, há uma assimetria norte/sul notável com energias superiores para o norte por causa dessas janelas de refração, a qual se ajusta perfeitamente a posição relativa dos diferentes tipos de barreiras costeiras do Holoceno.

Com isso, é possível afirmar que o atrito desempenha papel importante na diferenciação de onda ao longo da antepraia da PCS seja agindo sobre diferentes quantidades de refração ou agindo sobre as diferentes larguras da antepraia. Neste sentido, estes resultados permitem-nos definir que a orientação da linha de costa, a largura da antepraia e as declividades da plataforma média como os principais fatores que determinam o espectro de energia das ondas que chegam à costa da PCS. Os padrões gerais do clima de ondas da PCS puderam ser determinados aqui com a utilização de modelos numéricos, permitindo a quantificação dos gradientes de energia das ondas sobre a PCS e a argumentação sobre as razões de sua existência.

ABSTRACT

We initially expounded how geomorphologic features and sparse visual wave measurements, presented in previous works, point out to the possible existence of alongshore wave energy gradients over the Southern Brazilian Shelf (SBS). We have also examined the atmospheric conditions of the SBS, finding that intraseasonal oscillations can not only directly modulate the surface winds and sea level pressure but also indirectly modulate the period and amplitudes of synoptic-scale events. A good correlation between sea level pressure and the southern oscillation index on interannual timescales was also found, which attested the ENSO modulation.

Then, after briefly describe the two models utilized and the model grids and settings, the present study evaluated the proposed validation of the basin-scale model results against orbital altimetry and the validation of the regional-scale model results against the two available wavebuoy data over the SBS, discussing the extent to which the model reproduced local reality. Excluding localized errors, the WW3 model results of sig wave height on the Global and on the S. Atlantic grid could be considered as in very good agreement with observations, presenting remarkable similarities with observed altimetry data. Regarding the regional-scale modeling, both sig. height and peak periods as obtained on the Shelf grid were considered as in a very good agreement with observations. The peak directions, however, were classified as in poor agreement with observations. Nevertheless, the S or SSE waves were closely reproduced and it is only the ESE wave that was erroneously represented as approximately E or ENE by the model. The model results on the curvilinear Coastal grid were also considered as in very good agreement with observations for sig. height and peak periods but presented the same conflicting results regarding peak directions. We believe that these E or ENE waves were already incorrectly produced by the basin-scale model WW3, which then transferred this error downwards through the boundaries conditions. Increased spatial resolution certainly played a role and cannot be discarded, once it shows overall better statistics and greater variability of results, but it was the lowering of bottom friction that represented the major improvement in the curvilinear grid simulations.

Finally, we used our model results to show how the S. America blocks the waves generated by the westerlies, characterizing the western and southwestern S. Atlantic shelves with a general low energy mean wave climate. Lower mean peak periods were also found over the SBS indicating two important wave generation regions. We then showed examples of the extreme wave patterns induced by the presence of cyclones. Particular pre and post frontal conditions were also shown to fully characterize the synoptic-scale changes in the wave directions. The long-term mean offshore spectra showed a predominance of the S/SSW waves with a secondary power peak composed by ENE/E waves, corroborating with the statement that SBS is essentially bimodal in wave directions. The power of S/SSW waves diminish northward and the power of ENE/E waves secondarily diminish southward, allowing us to state that SBS is located in the encounter between the influence of the westerlies and cyclones and the influence of the SAH. The interannual distribution as annual means showed distinctive rises periods in ENE/E wave power and secondarily in the ESE wave power, which are modulated by ENSO. The six-hourly

intra-annual distribution showed a core of S/SSW waves occurring centered in wintertime between April and September. There is also an ENE/E core that occurs mainly during the springs in opposition to the lower powers found during wintertime. Highest SE waves occur mainly during April and May and secondarily during the spring and are associated with the cyclones.

Along-shelf wave energy gradients near the coast are already seen on the 2 km resolution shelf grid, with higher energy located off both capes and off the northern coastal projection and only secondarily off the southern coastal projection. On the other hand, energy minimum is found between coastal projections off Rio Grande and secondarily between capes and coastal projections. The offshore outer and mid-shelf declivities are not reflected on this energy pattern. Nearer to the coast, however, over depths shallower than 40 m the energy pattern does follow the bathymetric contours after a considerable drop of wave energy caused by bottom friction. Based on these results, we suggest the 40 m depth as the present day mean wave base and consequently the lower limit of the present SBS shoreface. The increased resolution of the Coastal grid allowed us to recognize that mean wave energy is in a more direct relation with the local shoreface width. It also permitted a clear geomorphological separation between the huge lower shoreface and the greater declivities of the tiny upper shoreface and the Albardão ridge. The upper shoreface mean wave power varies abruptly, decreasing from the half north to the half south points, in a clear response to offshore mid-shelf declivities. Thus, the geological inheritance expressed through the shoreface width and offshore mid-shelf declivities might indeed most times be more important to generate wave variability than the offshore wave power along-shelf variations itself.

Almost full refraction is observed between the bimodal offshore spectra and the upper shoreface spectra that were mostly found as ESE/SSE waves with increased SE wave importance and in an almost unimodal spectra. These results showed how the large and shallow SBS shoreface is responsible for an intense refraction of the waves, thus forcing them to approach the beach system with very small angles of attack. Additionally, the similarity between the mean power spectra of upper shoreface points indicated the sheltering effect caused by the capes and coastal projections and a windowing on the wave propagation until the shore, once shore normal waves reach the coast with higher energy than angled incoming waves. At between capes and coastal projections, where lower wave energies were found, there is a remarkable north/south asymmetry with higher energies to the north because of this refraction windowing, which closely fits the relative positioning of the different types of Holocene coastal barriers.

Altogether, it is possible to state that bottom friction plays a major role on wave differentiation along the SBS shoreface either by acting over different amounts of refraction or by acting over the different shoreface widths. In this sense, these results allow us to define the shoreline orientation, the shoreface width and the offshore mid-shelf declivities as the key factors determining the wave power spectra that ultimately reach the shore of the SBS. The general patterns of the SBS wave climate could indeed be successfully determined here with the use of numerical models, allowing the quantification of the wave energy gradients over the SBS and the argumentation about the reasons of their existence.

PREFACE

Once upon a time, not long ago, the full quantification of ocean properties and processes could be considered as virtually impossible. Those days are over.

Initially, the prohibitively high costs of synoptic ocean measurements and the difficulty to maintain it through long periods led to gapped observations in both space and time. However, with the advent of modern computers, the quantified interpolations and extrapolations of observed patterns were made possible by the use of empirically adjusted equations discretized in space and time, in a method called numerical modeling.

Nowadays, a great number of numerical models are public available producing an exponential growth of model users and quantified results. However, the quality of modeling results largely depends on proper model recalibrations to particular geometries and forcings, called sensitivity tests.

This time-demanding process of calibration is hardly available in modern days of competitiveness for the number of scientific publications or tight academic schedules. Usually, published experiments restarts from scratch with new geometries and forcings leaving no room for modeling continuity, which consequently generates the spreading of poor skilled model results.

During my doctorate, I dared to try and fit a handful of different numerical models of geophysical fluid dynamics and sediment transport in order to quantify coastal processes over the entire Southern Brazilian Shelf (SBS). Under huge computational efforts these models were subjected to intense sensitivity testing of geometries or numerical parameters. Whenever possible the model results were compared with existent field observations, quantifying its validation.

The La Plata river plume dynamics and its annual incursion over Brazilian waters, the summer upwelling jets and the bottom currents over the SBS are examples of results already obtained for hydrodynamics. Bedload sediment transport up to the 35 m isobath with 10^3 kg/m³ concentrations on the upper shoreface was also found, with sediment thickness indicating transport to the shore by wave asymmetry.

However, due to expected difficulties like the huge matrix sizes for high-resolution modeling and the absolute lack of field observations for model validation, the present thesis focused on the wave modeling effort.

Nevertheless, the project is currently ongoing and this work is considered just the first step into a fully 3D coastal area modeling for the entire shelf. This ocean modeling system shall be kept up to date and public available at project's website (www.renatocecilio.org).

Chapter 1

Introduction

The geological timescale evolution of a wave-build sand-rich shoreface, with its well known exponential shape, is believed to be dependent upon the incident wave power spectra and their gradients, relative sea level changes and sediment budget. Thus, the occurrence of sand abundance under a possible condition of standstill sea level leads to a situation where wave gradients become the major forcing controlling coastal evolution.

As we will see, this idealized situation happens to resemble with the present day situation over the Southern Brazilian Shelf (SBS) and Coastal Plain (SBCP), presented in Figure 1.1. Both SBS and SBCP, as understood in the present work, lie between 28.6 °S and 34.4 °S of Eastern South America at Cape Santa Marta (Brazil) and Cape Polonio (Uruguay), respectively. They share an approximately 800 km long almost continuous gentle undulating shoreline, with a general NE-SW orientation, that forms two coastal projections.

The shoreface floor all along the coast consists mainly of sandy sediments, turning into well-sorted fine sand over the beach system (Martins, 1967; Martins and Correa, 1996). It also presents the typical exponential shape of sandy wave-dominated coasts, also referred as the shoreface profile of equilibrium (e.g. Fachin, 1998; Gruber et al., 2003).

The long shoreline is only interrupted by shallow channels of some lagoons and some small rivers near highlands in the north. Exception is made to the 20 m depth of Patos lagoon mouth (32 °S / 52 °W) where is located the access channel to the Port of Rio Grande, considered the second most important port of Brazil. This great shoreline continuity is a direct consequence of its extreme microtidal condition, with tidal ranges that barely reach half a meter. More significant sea level oscillations are imposed by storm surges and wind set-up when it can rise up to 1.9 m (Calliari et al., 1998; Saraiva et al., 2003 and Parise et al., 2009).

Over land, the huge low-relief coastal plain (SBCP) is practically fully-clastic, extends over about 40,000 km²with millions of inhabitants and presents two major lagoons (Patos and Mirim), along with a series of smaller ones. This region was first described by Villwock et al. (1986) as being composed by four successive barrier-lagoon depositional systems formed by the cycles of glacio-eustatic sea level variations that occurred during the Late Quaternary (last 400 ky) leaving a wave-build sandy barrier at the transgressive maxima of each event. Full geological setting can be found in Tomazelli et al. (2000).

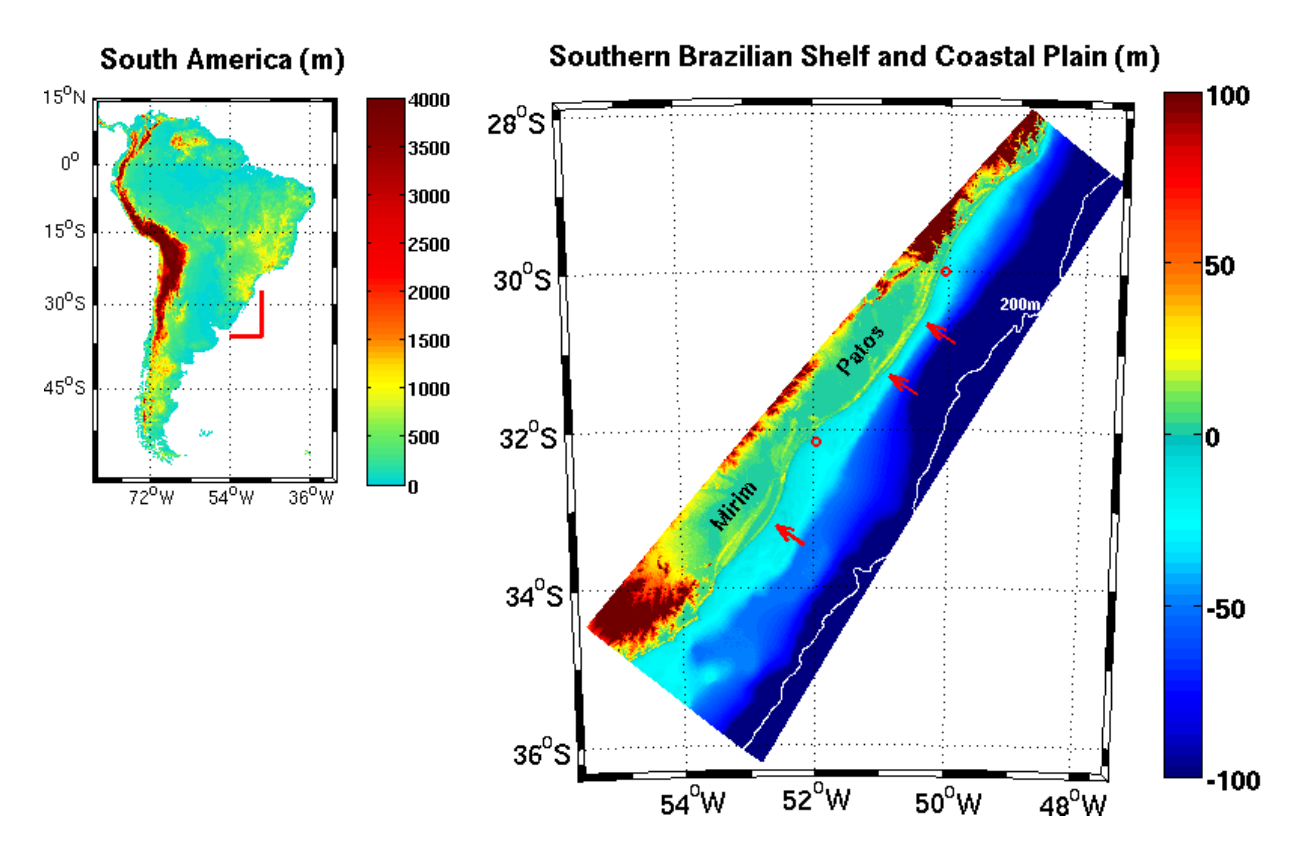


Figure 1.1: South America (left) and Southern Brazilian Shelf and Coastal Plain (right) reliefs. Red arrows indicate the approximate positions of higher wave energy and red circles the positions of wave-buoy measurements used in the validation process (Rio Grande and Tramandai). See text for further details.

In spite of the origin and evolution of this important and extensive area to be closely bound to the wave-driven process of shoreface/barrier maintenance and of its particular sensitiveness to any possible change in wave climate, the wave energy reaching the shore of the SBCP has not yet been properly quantified.

This is because wave data over the SBS are scarce in both space and time. For the entire 20th century the only buoy data of ocean waves was presented by Wainer (1963) that, for reasons of port engineering, used an inverted echo-sounder (registering in thermal paper roll) between October 1962 and September 1963 at 17.5 m depth off Tramandaí.

The author determined the occurrence spectra finding the maximum significant wave height as 4.8m in April 1963 with predominant occurrence of 1.5 m and 8 s period. The direction of wave incidence was acquired visually, indicating that incident swell and sea were respectively from southwest and east with crests almost parallel to the coast when entering shallow water.

In the turn of the century and again for port engineering purposes, Strauch (2001) presented the measurement carried out with a directional wave-rider located close to the mouth of the Patos lagoon at 17 m depth between 1996 and 1999. The data indicate that at least in front of Rio Grande, the predominant waves have mean significant wave height of 1.0 m in the 100° direction (ESE) with mean wave period of 8 s and mean significant height of 1.5 m in the 160° direction (SSE) with mean wave period of 12 s.

More recently, Strauch et al. (2009) presents a comparison between the previously obtained data from Rio Grande with new wave-buoy data obtained at 17.5 m off Tramandaí during 2006

and 2007. They relate a great similarity between the behavior of the wave regime over fall and summer for these two locations.

At the surroundings outside SBS, also only few measurements were taken. Araujo et al. (2003) provided a statistical description of wave conditions based on measurements with a directional wave-rider deployed just 150 km northward from the SBS at approximately 80 m depth. Their results indicate swell predominance over local sea conditions during autumn and winter with sea conditions prevailing during the spring. In the summer, there is a balance between these two states. Their analysis showed a well-defined 12 s swell from the South and 8 s sea-waves from the East.

South from SBS, between the Uruguayan and Argentinean coasts, the same lack of data exists and also with several gaps in the records (Dragani et al., 2008; 2013). There, the SE, E and S are the main directions of propagation, with 43.7 %, 24.9 % and 14.4 % of the occurrences, respectively. Heights were predominantly between 0.5 and 2 m with more waves from S when height exceeds 2 m. For the more common SE waves, one relative maxima with 10 s periods and 0.8 m heights and other with 5 s and 1.25 m, could be clearly identified.

This almost inexistence of wave data along the coast, however, does not hide the effects of the waves over coastal geomorphology. According to the Holocene sea-level curve proposed by Angulo et al. (1999, 2006) for an adjacent area, the sea level behavior can be considered stable or quasi-stable for the last 5000 years, because the rate of sea-level change is relatively low (-0.4 mm/y).

Thus, Dillenburg et al. (2003), assuming stable sea-level, sand abundance and in analogy to the conceptual model of May and Tanner (1973) for littoral sediment transport, stated the hypothesis that observed geomorphologic and stratigraphic differences in the Holocene barrier types along the coast (Dillenburg et al., 2009) should have been caused by alongshore wave energy gradients. They proposed that convex coastal projections with higher shelf declivity (up to 70 m) would concentrate the wave energy, resulting in coastal erosion, while a concave coastal embayment with gentle shelf declivity would diverge the wave energy and consequently induce sediment deposition.

Toldo et al. (2006), although observing extensive shore retreat along the northern coastal projection of the SBCP, report two hotspot accretions occurring for the last 30 years and associated it to the reduction of longshore sand transport due to changes in the shoreline orientation. That reduction would then produce a "jam" of sand that induces deposition and increases the upper-shoreface width from less than 1 km to more than 3 km.

Their results show that, at least at engineering timescales, the behavior of the SBCP shoreline might be predominantly controlled by wave convergences or divergences and, therefore, by the gradients on the wave power spectra along the coast.

With all observations pointing to the existence of an alongshore wave gradient and its potential impact over sand dynamics, Martinho et al. (2009) compiled the few consistent visual observations of waves from the shore (Calliari and Klein, 1993 and Barletta, 2000) in the search for a large scale pattern.

Calliari and Klein (1993) visually obtained the breaking wave height (Hb) and the wave period (T), during one year (March 1991-1992), at beaches of the southern part of the SBCP shore. The data were collected by measuring the difference between wave crest height and trough at a determined point inside the breaking zone. Barletta (2000), from 1996 to 1999, visually collected Hb and T data along the central part of the SBCP shore also using a qualitative visual method.

Then, Martinho et al. (2009) completed the scenario by collecting Hb and T data from the northern part during an one year period (September 2004–2005). The visual measurement method utilized was the "line of sight" method, named by Patterson and Blair (1983) and originally described by Ingle (1966).

However, during the compilation of the three parts, these differences in the methods for observation of parameter Hb and the different periods of observations forced the authors to remain into a qualitative classification of wave energy, making it impossible the absolute comparison between the wave energies reaching the northern and southern projections, for instance.

Nevertheless, they were able to identify three main points of higher wave energy (red arrows in Figure 1.1). Those wave energy concentrations occurred at coastal projections as predicted by Dillenburg et al. (2003) and, along the northern coastal projection, approximately where Toldo et al. (2006) observed extensive shore retreat and hotspot accretions.

The present work aims to fill this need for a quantitative description of the wave gradients along the entire Southern Brazilian Shelf and its variability over time, therefore corroborating the thesis of their existence. The wave fields obtained this way shall be used to feed a fully 3D sediment transport model for the coastal evolution of SBS and SBCP.

In chapter 2, we characterize the atmospheric conditions driving the ocean waves that ultimately reach the shore of SBS, showing typical winds and the sea level pressure variability over different timescales. In chapter 3 we first describe the ocean wave models utilized and the experiments grids and settings and then we present the model validation against orbital altimetry and wave-buoy data, in order to discuss the extent to which the model reproduces reality. Finally, in chapter 4 we describe the bathymetric features of the SBS and present the spatial and temporal variability of modeled wave fields, identifying typical waves and its origins. At last, we expect to propose an ocean wind-wave climatological field for the SBS to be used on geological timescale modeling efforts.

This ocean wind-wave modeling system shall be kept up to date and public available at project's website (www.renatocecilio.org). Every new consistent data collected over the region will be used to revalidate the model in order to quantify any possible drift in model skill.

Hopefully, it might assist coastal geology or engineering and possibly be used to help monitor any change in SBS wave climate. Moreover, the problem of quantifying the wave climate, understanding the interaction of waves with structures or sediments and predicting the associated responses underlies almost every problem in coastal and ocean engineering (Dean and Dalrymple, 1991).

Chapter 2

Atmospheric conditions

The atmospheric phenomena giving rise to the ocean wind-waves that ultimately reach the shore of SBS occur as synoptic-scale events (2 to 12 days) embedded in the mean atmospheric circulation. However, strong intraseasonal and interannual modulations make the synoptic events rather different from each other, forcing them to be treated statistically or as particular events case studies.

2.1 Mean Circulation

The general atmospheric circulation, detailed in most text books of atmospheric sciences (e.g. Marshall and Plumb, 2008), can be seen in the mean annual variability of high-level geopotential heights and mid-tropospheric vertical motions (Figure 2.1), high-level winds (Figure 2.2), sea level pressure and precipitation rate (Figure 2.3) and low-level winds (Figure 2.4) presented as seasonal mean maps obtained from NCEP/NOAA Reanalysis Long Term monthly means (1981-2010) retrieved from website (www.esrl.noaa.gov/psd) with 2.5° horizontal resolution (Kalnay et al., 1996).

The warming and expansion of the tropical atmosphere and the cooling and contraction over the poles, driven by latitudinal gradients of the incoming solar radiation, leads to a large-scale slope of the pressure surfaces and hence pressure gradient forces directed from equator to pole. This slope is seen in the geopotential heights of 250 hPa, presented as black isolines in Figure 2.1, that show five contours from 11 km at tropics to 10 km near pole, with 0.25 km intervals (10 km height contour is absent during DJF).

The maximum upward motion and precipitation occurs over the tropical oceans along the belt of low sea-level pressure and surface wind convergence, called Intertropical Convergence Zone (ITCZ), which migrates annually in agreement with maximum incoming solar radiation.

As this uplifted saturated air flows poleward in the upper atmosphere in response to the pressure gradient forces, the radiative loss of heat cause large-scale subsidence over broad areas of the subtropical oceans maintaining the very persistent low-level cells of high sea-level pressure, dry air and anticyclonic circulation over South Atlantic and South Pacific, with only minor seasonal variations.

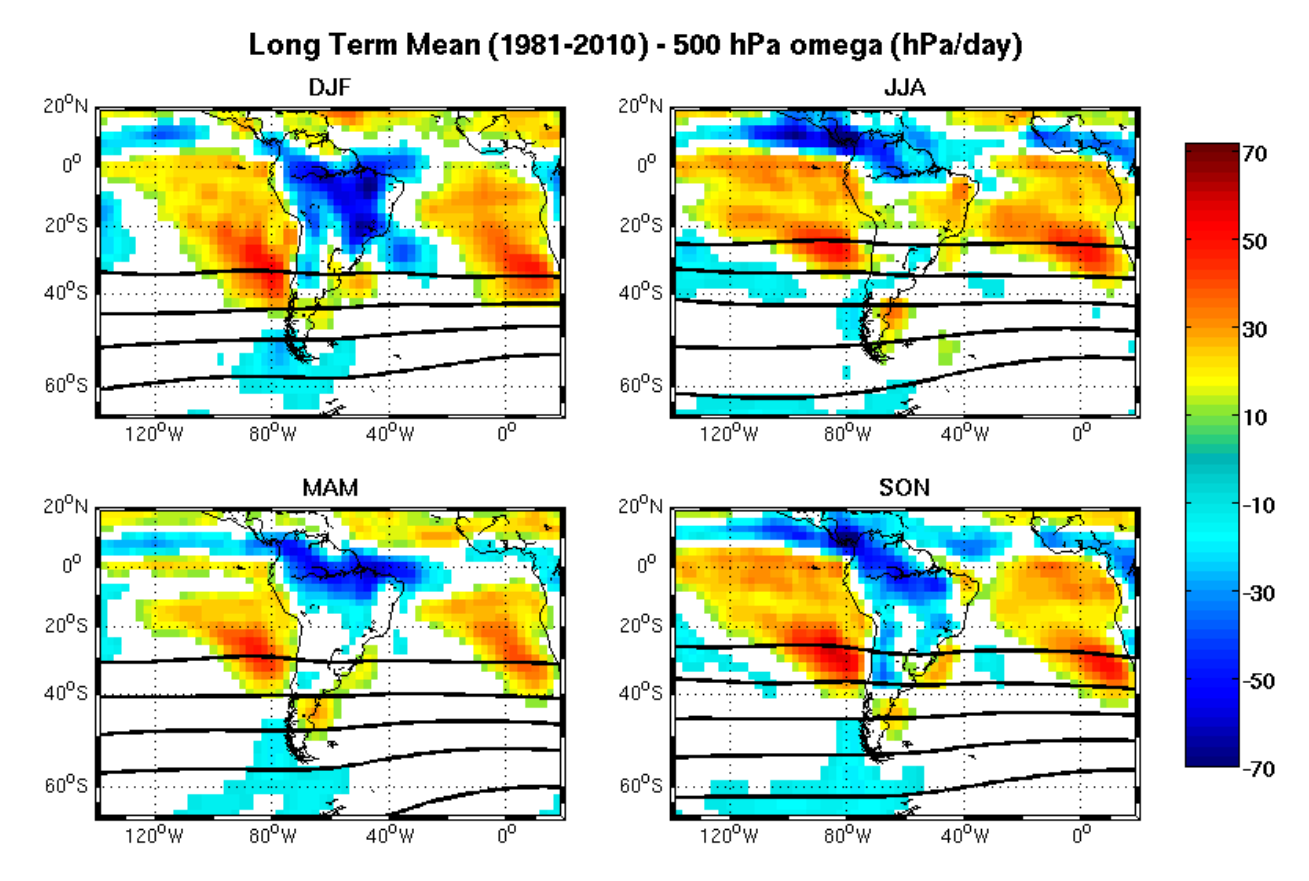


Figure 2.1: Seasonal means of Long Term (1981-2010) mid-tropospheric (500 hPa) omega as proxy of vertical motions. Black lines are the high-level (250 hPa) geopotential height contours from 10 to 11 km with 0.25 km intervals.

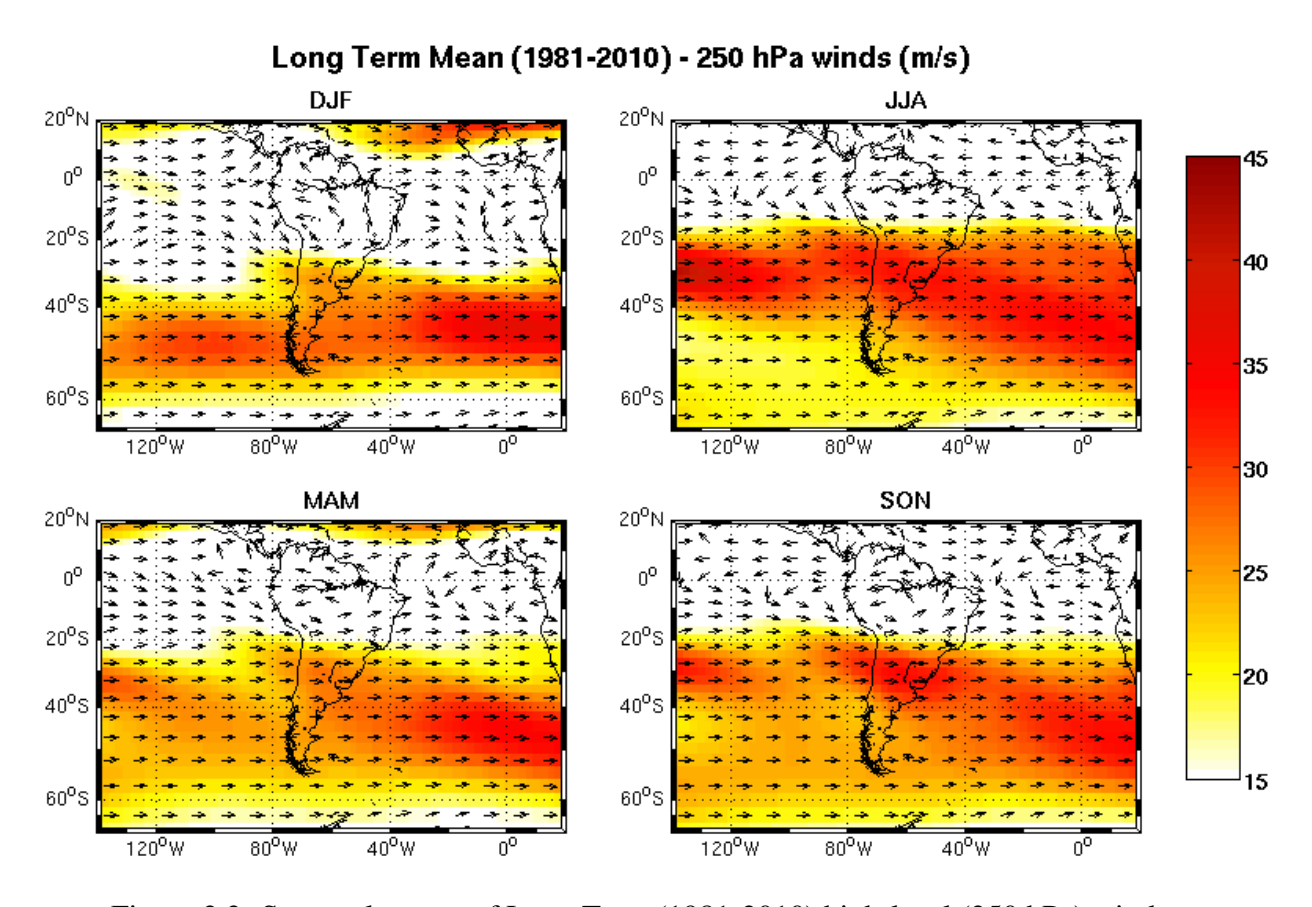


Figure 2.2: Seasonal means of Long Term (1981-2010) high-level (250 hPa) winds.

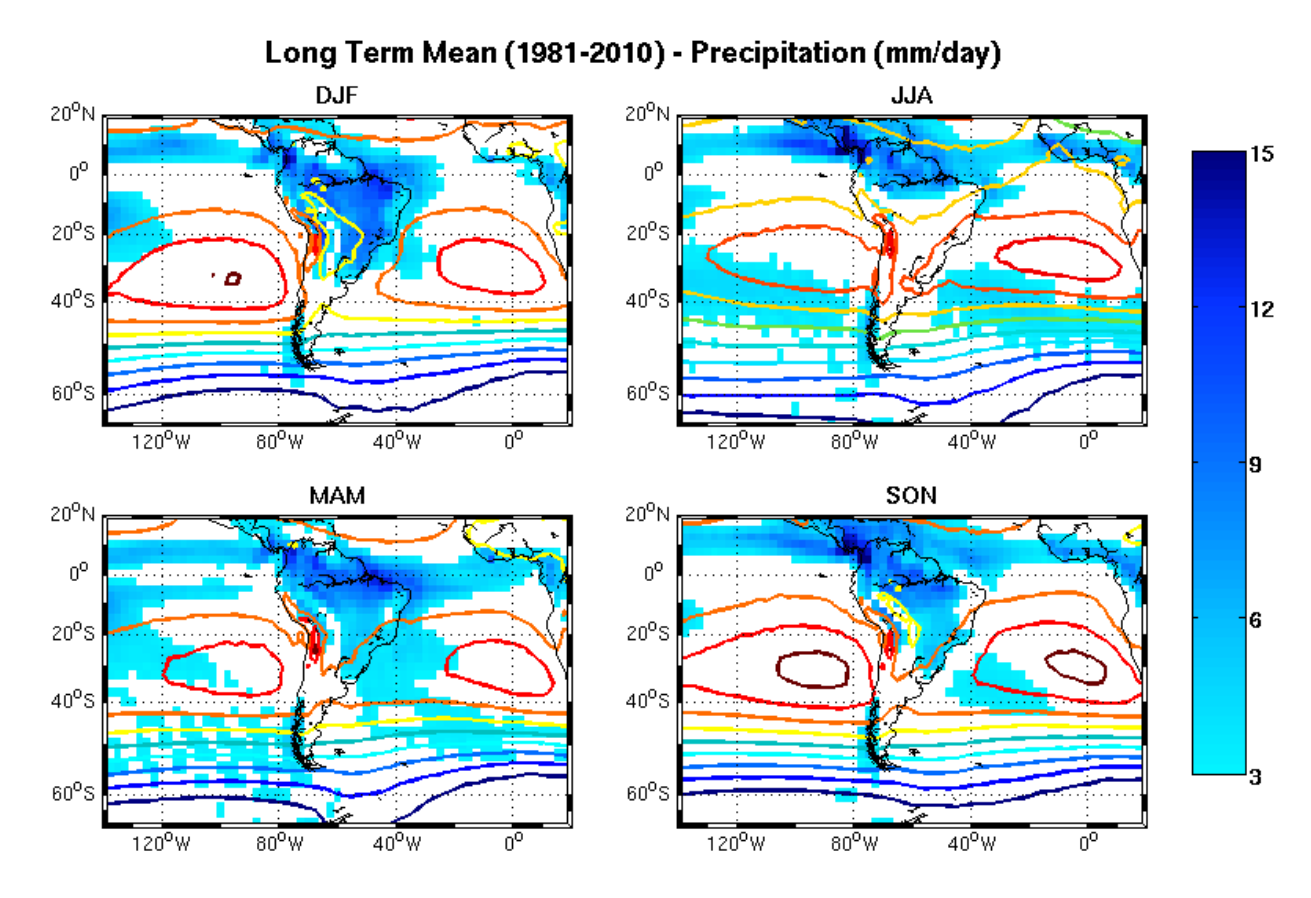


Figure 2.3: Seasonal means of Long Term (1981-2010) precipitation rates. Contours show sea level pressure from 990 (dark blue) to 1026 (dark red) hPa with 4 hPa intervals.

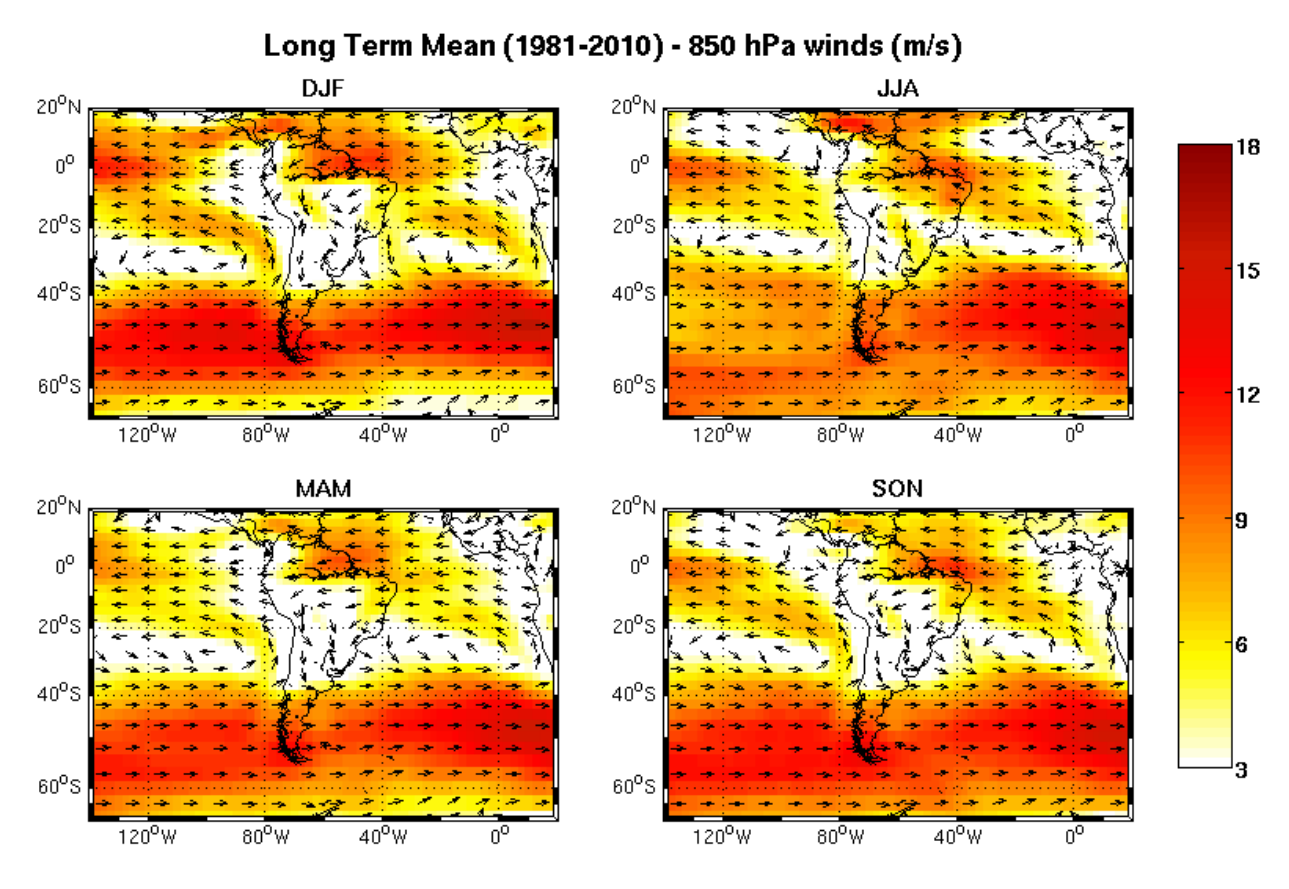


Figure 2.4: Seasonal means of Long Term (1981-2010) low-level (850 hPa) winds.

Over the continent, mean upward motion prevails and sea-level pressure is lower than over the adjacent oceans throughout the year, forcing the trade winds over the tropical South Atlantic to change direction, completing the observed low-level anticyclonic circulation.

Together with the subtropical subsidence, the low-level southeast trade winds and the ascent over the ITCZ, this higher levels poleward winds at the tropics complete the Hadley cell, a major feature of the atmosphere's general circulation.

Poleward from the equator, the enhancement of planetary vorticity with latitude forces the geostrophic adjustment and the circulation in upper atmosphere acquires increasing eastward orientation with increasing southern latitude. At the same time, as the warmer tropical air moves into the colder subtropics, the strengthening of meridional temperature gradients and the associated baroclinic pressure gradient generates the subtropical jet stream, which delineates the southern boundary of the Hadley cell over South Atlantic (Figure 2.2).

This subtropical jet stream has mean velocity of 30 m/s with one of its cores located approximately between 25/40 °S of South America. During most of the year, this core assumes NW/SE orientation and is clear distinguishable in the high-level winds just upstream of the SBCP and SBS. During winter, the presence of westerly winds at 25 °S is noteworthy, but the jet stream can still be seen.

South of 30 °S, planetary vorticity gets greater than unity and the circulation becomes predominantly normal to the pressure gradient. There, these westerly winds, which increases with height mainly by thermal wind balance rather than friction, are more often seen throughout the depth of the thinner mid-latitude atmosphere.

These westerlies (Figures 2.2 and 2.4) have a dominant whole-year influence at mid latitudes and are responsible for the high precipitation in southern Chile, due to the enhanced uplift over the western slope of the Andes, and for the downstream dry conditions in Argentinean Patagonia (Figure 2.3). During summer, the westerlies contract to the south and show stronger wind velocities than during winter, when the wind velocities in the core zone decrease as it migrates northward.

Farther south, around about 50 °S, the convergence of these mid-latitude westerlies with the easterlies generated by the freezing large-scale subsidence over South Pole form the subpolar front and subsequently the subpolar jet stream with stronger mean cores over South Atlantic than over South Pacific.

As above mentioned, exception be made to the more persistent subtropical high pressure cells, all other patterns of the mean atmospheric circulation show accentuated northward displacements during fall and early winter with subsequent southward return during spring and early summer, in clear agreement with the annual variability of incoming solar radiation caused by the tilt of the Earth's rotation axis.

However, as depicted in Figures 2.1 to 2.4, the highest annual variability is observed over the continent. Over South America, the diverse patterns of weather and climate variability arise from the long meridional span of the continent with the continuous western coast Andes cordillera representing a formidable obstacle for tropospheric flow as it reaches elevations in

excess of 4 km from the equator to about 40 °S (Garreaud and Aceituno, 2007).

During most of the year, the positioning of the ITCZ over the North Atlantic Ocean forces a relatively lower incidence of deep convection over the central part of the continent, which characterizes the dry season, interrupted occasionally by the passage of modified frontal systems from southern mid-latitudes. The onset of the wet season supporting the Amazonia rainforest typically occurs during austral spring, approximately when the ITCZ reaches the equator, enabling boreal northeasterly trade winds to transport ocean moisture toward the Amazon Basin.

By late November, when the ITCZ advances over the greater zonal extent of the continent (~5 °S), deep convection covers most of central South America from the equator to 20 °S, but is absent over northeastern Brazil and the subtropical plains. The decay phase of this wet season typically occurs during early fall and is related with the return of ITCZ to the Northern Hemisphere.

These markedly seasonal circulation systems, called monsoon, develop over low-latitude continental regions adjacent to an ocean as a direct response to seasonal changes in the ocean/land thermal contrast. Works like Zhou and Lau (1998), Nogués-Paegle et al. (2002), Vera et al. (2006), Marengo et al. (2010), Liebmann and Mechoso (2011), and references therein, made considerable advance in the characterization of the South American Monsoon System (SAMS).

The upper-level circulation during this wet season includes a well-defined anticyclonic circulation, referred as the "Bolivian High", firmly established over the central part of the continent (15 °S / 65 °W) and persistent enough as to appear in the long-term summer mean at the 250 hPa level. An upper-level trough also develops downstream, forcing the dryer region near the coast of northeast Brazil.

At low levels, the thermally driven "Chaco Low", reinforced through the barrier role of the mountains (Gandu and Silva Dias 1998, and references therein), is the most conspicuous summertime feature and can be considered together with the Bolivian High as the regional response of the tropospheric circulation to the strong convective heating over the Amazon and central Brazil.

The presence of this very deep continental low forces the tropical easterly winds passing over the Amazon basin to turn southward, transporting large amounts of moisture that feeds summertime convective storms over the subtropical plains as far south as 35 °S.

The works of Paegle (1998), Saulo et al. (2000, 2007), Salio et al. (2002), Campetella and Vera (2002) and Marengo et al. (2004) discuss how this northerly flow, after being constrained by the eastern slope of the Andes, often exhibits throughout the year a low-level jet structure (LLJ, ~17 °S), with its core at about 1 km above the ground.

Although it is, in fact, a mesoscale atmospheric phenomenon, this name has been extended to identify, from a large-scale perspective, the moisture corridor that exists along the eastern slope of the Andes resulting from the split of the trade winds upon approaching the mountains (Silva Dias, 2000).

The low-level convergence of these tropical northerly winds with mid-latitude westerlies, modulated by the variability of LLJ and the mid-latitude synoptic-scale activity, generates a

southeastward band of cloudiness and precipitation extending from southern Amazonia toward western South Atlantic. That convection band, known as the South Atlantic Convergence Zone (SACZ, Kodama, 1992, 1993; Figueroa et al. 1995; Liebmann et al. 1999 and Carvalho et al. 2004), can eventually be seen throughout the year, but is strikingly more intense and longer lasting during summer when it becomes a distinctive feature of the SAMS, although it seldom persists for more than 10 days at a time.

In summary, the large-scale atmospheric mean circulation presents itself as a strong annual oscillation of a convergence zone of tropical northwesterly and mid-latitudes westerly low-level winds reaching the SBS and SBCP from the continent and carrying embedded all synoptic-scale phenomena eastward or southeastward into the South Atlantic (Figure 2.5).

Over the ocean, the South Atlantic Subtropical High (SAH) moves eastward during summer, reflecting the pressure reduction over the continent. Because of the presence of friction in the atmospheric boundary layer, the surface wind also shows a significant ageostrophic component directed from high pressure to low pressure.

The resultant pattern is shown in Figure 2.6 with the seasonal means of surface (10 m) winds as interpolated from the Long Term mean (1981-2010) gaussian grid with approximately 1.9° at mid-latitudes to the same 2.5° resolution presented in earlier figures. It is clear the predominance of northeasterly winds along the Brazilian coast, throughout the year but in winter, being responsible for carrying heat and moisture from the tropical South Atlantic southwestward. Over SBS and SBCP, surface winds assume an almost easterly direction, blowing onshore winds on the coast for most of the year.

It is worth to mention that these surface winds are the same responsible for wind-wave growth and, therefore, in a hypothetical total absence of synoptic-scale phenomena the SBS wind-wave climate would most probably be unimodal low-amplitude ENE waves, once westerlies from the continent do not have sufficient ocean area (fetch) in order to develop high waves.

2.2 Synoptic-scale winds

In the extratropical atmosphere, traveling weather systems with synoptic timescale (2 to 12 days) arise from the hydrodynamic instability of the thermal wind shear of westerlies, with the flow spontaneously meandering or breaking down into eddies and readily generating meridional motion through a mechanism known as baroclinic instability. Those meridional motions are then readily forced to restoration by the planetary vorticity gradient, triggering the propagation of short-wavelength planetary Rossby waves.

Berbery et al. (1992), Hoskins and Ambrizzi (1993), Ambrizzi et al. (1995), Ambrizzi and Hoskins (1997), Mo and Paegle (2001), Marengo et al (2002) and, more recently, Müller and Ambrizzi (2007, 2010) discuss these planetary Rossby waves propagation and the associated teleconnection patterns in the southern hemisphere showing that the main Rossby wave activity takes place in the region of the subtropical and subpolar jet streams, whose strong gradients act as wave guides.

Long Term Mean (1981-2010) - 850 hPa winds (m/s)

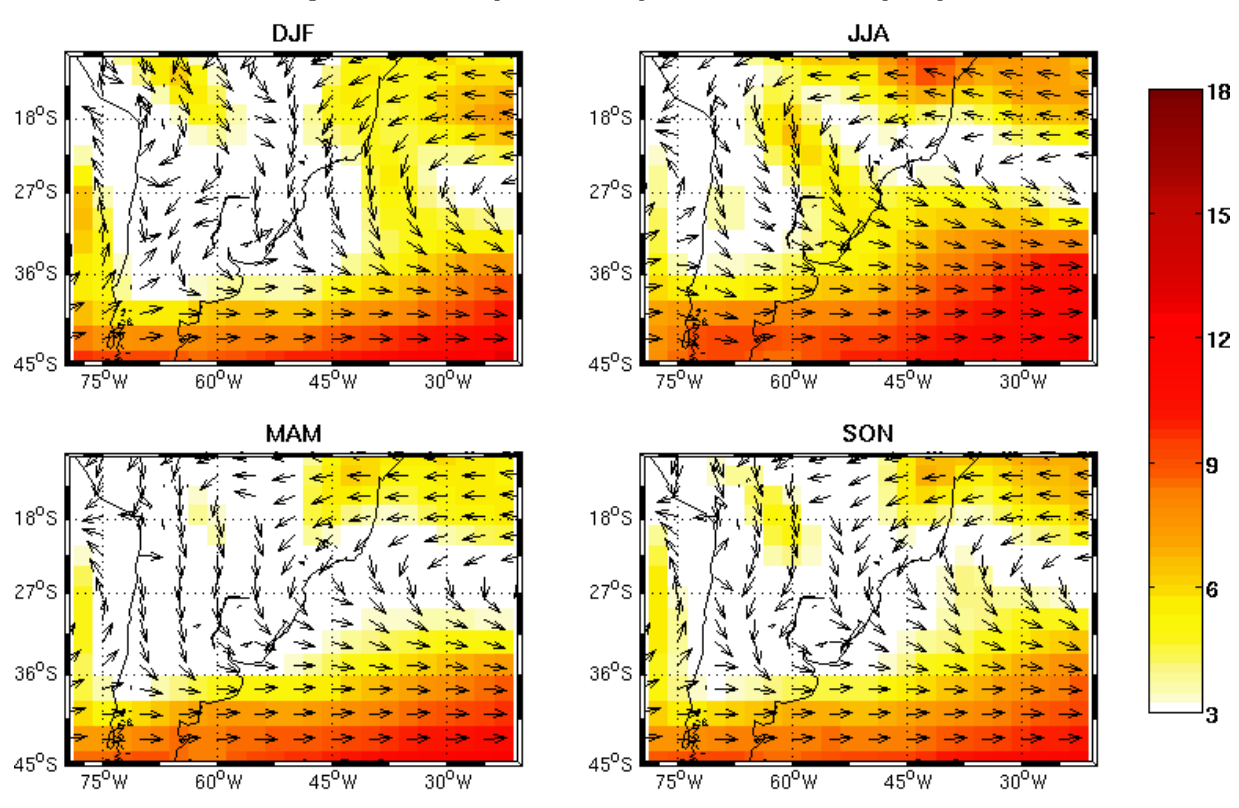


Figure 2.5: Seasonal means of Long Term (1981-2010) low-level (850 hPa) winds over SBS and SBCP.

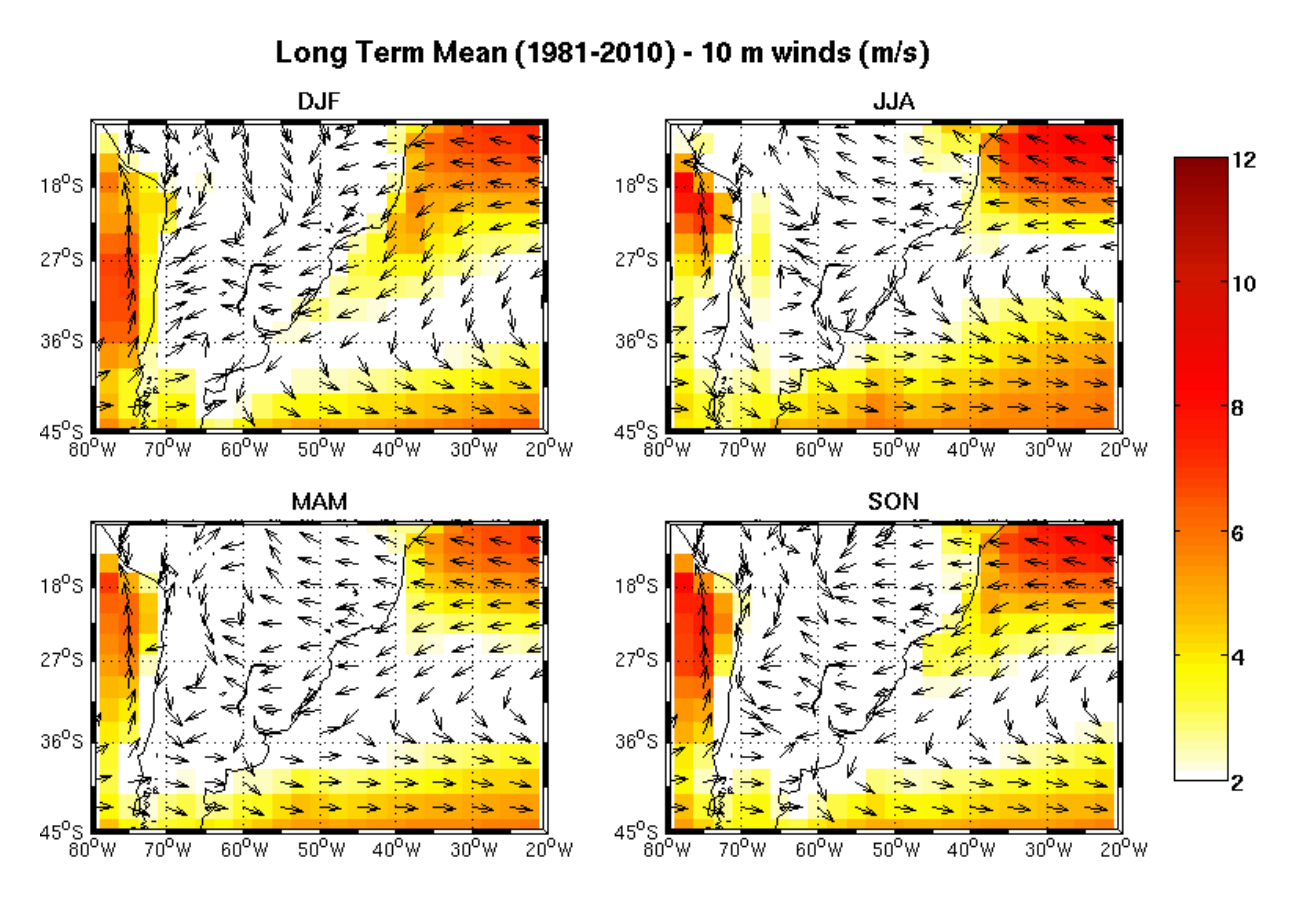


Figure 2.6: Seasonal means of Long Term (1981-2010) surface (10 m) winds over SBS and SBCP.

In order to illustrate these Rossby waves, we present in Figure 2.7 a Hovmoller diagram in longitude/time domain of the six-hourly meridional 250 hPa wind anomalies for the last year of the wave simulations (2012). These anomalies were produced by removing the seasonal mean circulation through the use of a high-pass filter with sharp edge and 90 days cutting frequency. The values along the longitudes were obtained with latitudinal averages within 45-55 °S (left) and 30-40 °S (center and right) in an attempt to frame the subpolar and subtropical jet streams, respectively. Velocities smaller than 10 m/s were omitted for clarity.

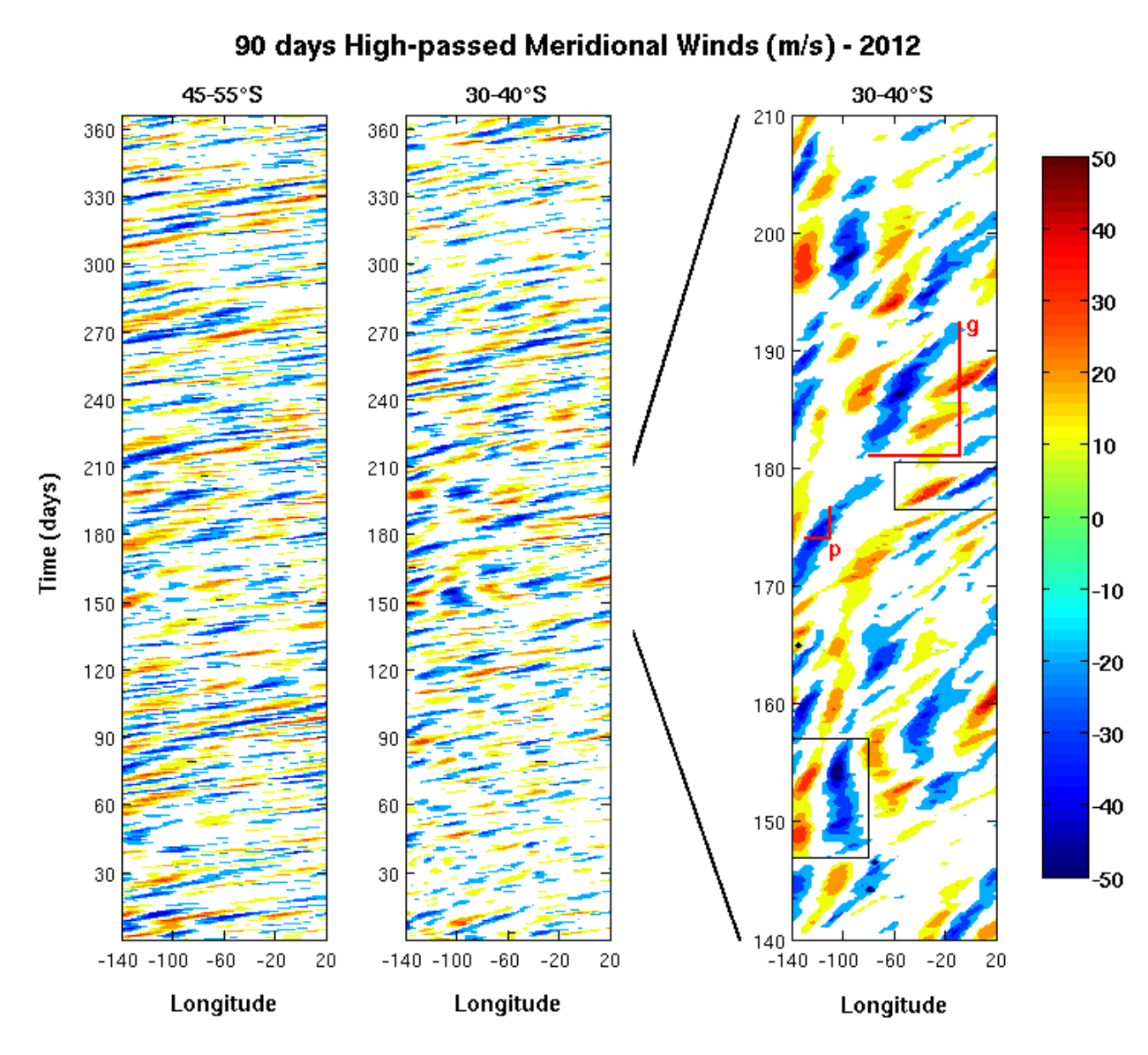


Figure 2.7: Hovmoller diagram in longitude/time domain of the six-hourly meridional 250 hPa wind anomalies after 90 days high-pass filtering. See text for details.

The planetary Rossby waves are seen as eastward inclined patterns of opposite meridional wind anomalies that form their upper-level troughs and ridges. In the 30-40 °S frame the wind velocities are greater mostly during winter and in the 45-55 °S frame the greater wind velocities are more evenly distributed throughout the year, in agreement with the annual variability of the westerlies.

Both frames present strong discontinuities as the velocity bands get in and out of the frames

used in the averaging processes, but discontinuities are certainly greater in the frame 30-40 °S. This is probably because the subtropical jet is aloft the Andes cordillera (~70/65 °W) and has a more meridional orientation (NW/SE), forcing the high-level troughs and ridges to occur at slightly different mean latitudes and therefore to escape from framing, while the more zonal subpolar jet is over the flat Southern Ocean or over the southern tip of South America where the Andes relief is lower.

Although this might considerably complicate the fully tracking of such Rossby waves, it is still possible to get an initial estimate of its phase and group velocities by the longitudinal and temporal dimensions as shown in red lines in Figure 2.7 (right). In this case, phase (p) and group (g) velocities yield 7.15 and 6.25 longitudinal degrees per day, respectively, with approximately 60° of wavelength or wavenumber equal 6. Black line boxes show a more quasi-stationary case in South Pacific (left box) and a higher intensity and smaller dimension eddy with greater group velocity in South Atlantic (right box).

At surface, those eastward short-wavelength Rossby waves manifest themselves as a succession of high and low pressure systems moving across South America, where they experience a marked anticyclonic turning and equatorward elongation while becoming disconnected from the upper-level trough and ridge, which continue to move eastward (e.g., Gan and Rao, 1994; Garreaud, 2000; Vera et al., 2002 and Seluchi et al., 2006).

Figure 2.8 illustrates the process with the event centered in 27th September of 2012. The utilized sea level pressure six-hourly data of NCEP Reanalysis were also 90 days high-passed, the same way as previously done with the 250 hPa wind.

Initially, an anticiclonic high pressure approaches from the west, while an extratropical cyclone forms over South Atlantic. East of the Andes, the lee trough induced by adiabatic warming causes northerly winds (Figure 2.8, top).

A couple of days later the surface high starts to displace the low, but anticyclonic winds are blocked by the eastern flank of the Andes and the resulting ageostrophic winds then advect the high pressure northward, causing cold air surges with frontal systems on its leading edge. When the high is northward advected, a clear long fetch establishes over western and southwestern South Atlantic that results in the possibility of high S/SW waves (Figure 2.8, center).

Once the high migrates over South Atlantic, easterly and southeasterly winds from the high pressure blow the ocean moisture back to southeast South America, against the mean circulation, and possibly generate E/SE waves (Figure 2.8, bottom).

The above mentioned succession of high and low pressure systems moving across South America ultimately results in alternate surface winds over the ocean. To illustrate the phenomenon, we present six-hourly zonal and meridional surface (10 m) wind data of NCEP Reanalysis for a location representative of the northern part of SBS and again for the last year of wind-waves simulations (Figure 2.9, black lines).

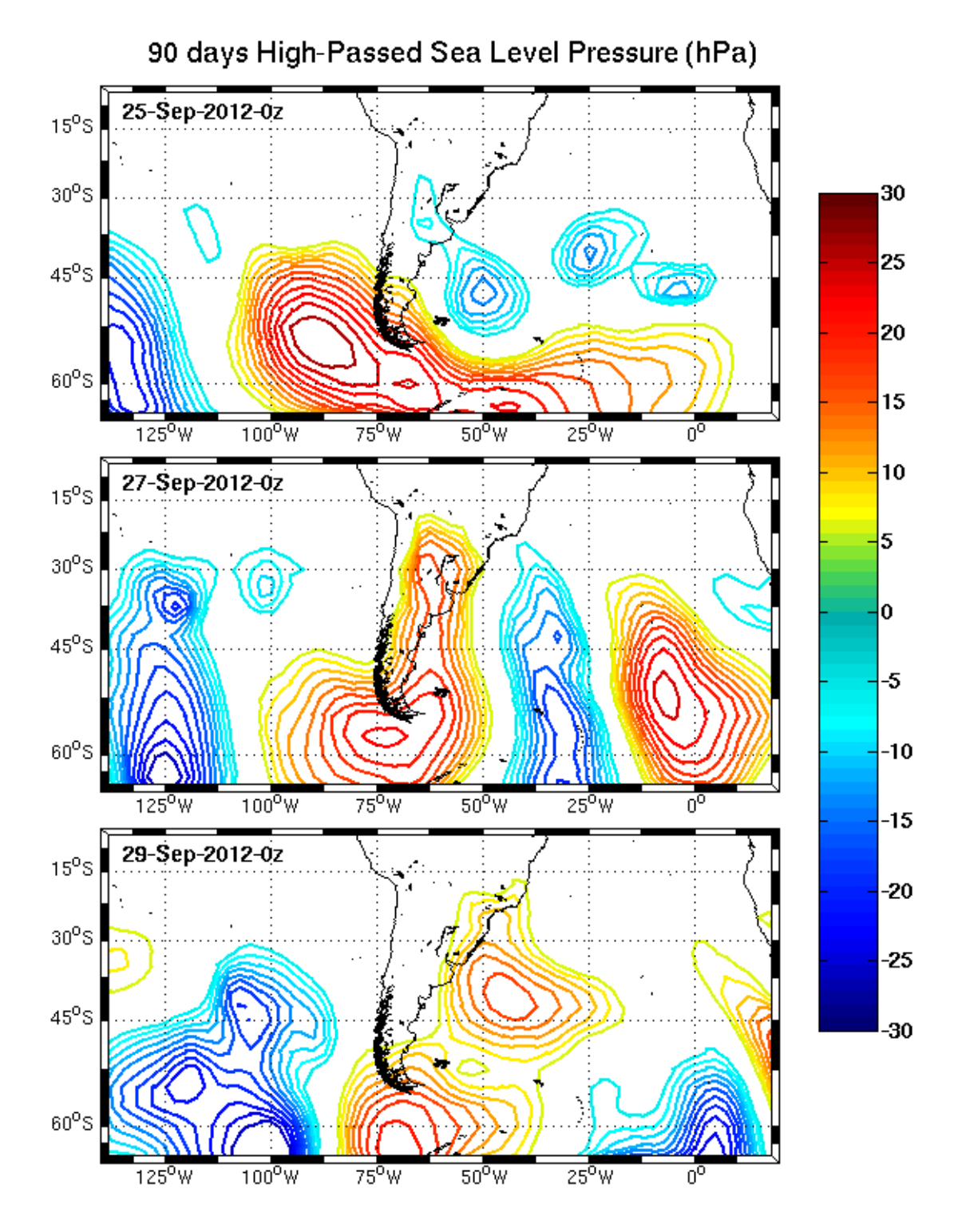


Figure 2.8: Succession of sea level high and low pressure systems moving across South America. See text for details.

Although some small amplitude diurnal oscillations can be seen, it is the strong synoptic-scale oscillations with amplitudes up to 20 m/s that prevail in the series. They are seen in both directions and around its own 40 days low-passed series (red lines).

As can be also indirectly depicted from pressure maps in Figure 2.8, under typical conditions the surface winds go from the mean northeastern to a pre frontal continental northwestern and then to southwest during the advance of the system. Later the wind rotates to south and finally southeast/east, before returning to the mean northeastern under SAH influence again.

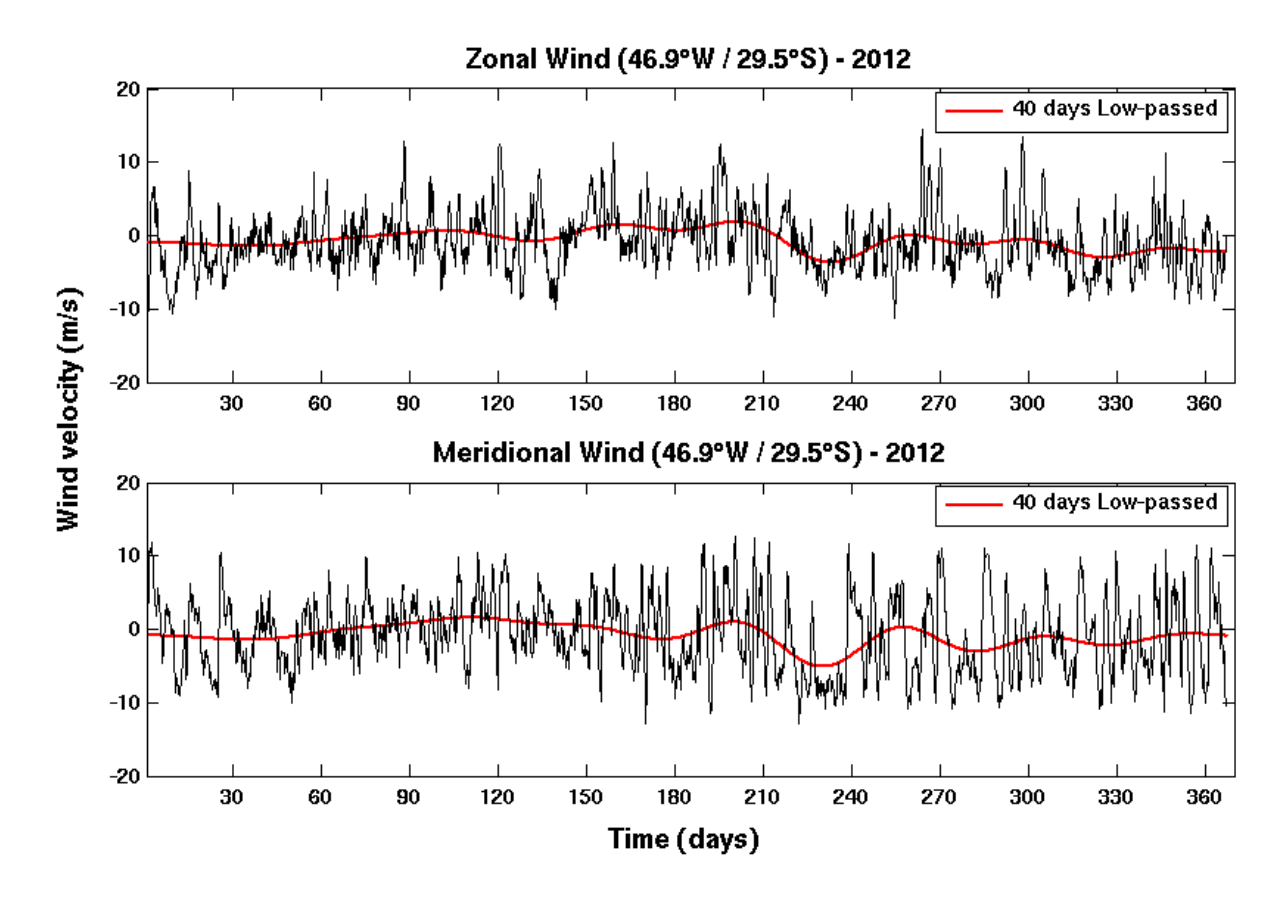


Figure 2.9: Six-hourly zonal and meridional surface wind data (black lines), for a location representative of the northern part of SBS during 2012. Red lines show the 40 days low-passed series.

Both E/SE and S/SW wind-waves are then possibly generated under this typical condition of synoptic succession of pressure systems, but it is actually under extratropical cyclogenesis that stronger winds and higher wind-waves are seen.

The extratropical cyclogenesis over the southern hemisphere has been highlighted since the historical works of van Lonn (1965) and Taljaard (1967) that utilized subjective visual analysis of sea level pressure maps to characterize these systems and defined some important features like the cyclogenesis over South America, with its higher occurrence during wintertime and its eastern or southeastern propagation embedded in the mean circulation.

Specifically over South America, the works of Necco (1982 a,b) and Satyamurty et al. (1990) made important contributions to the matter but it was their conflicting results that motivated the consistent climatology of Gan and Rao (1991) and Gan (1992). These authors subjectively examined over 14000 pressure charts finding that the majority of events happen during winter near 32.5 °S (Uruguay) with a secondary maximum near 42.5 °S (Argentina) during summer.

With the advance of computers in the 90's, automatic procedures could be applied for finding and tracking these systems, either by identifying minimum sea level pressures (e.g. Murray and Simmonds, 1991 a,b) or minimum relative vorticity (e.g. Sinclair, 1994), permitting the handling of a much larger amount of information in a fraction of the time and the objective comparison between different works. Other works on climatology of cyclogenesis over the

southern hemisphere include those of Sinclair (1995, 1997), Simmonds and Keay (2000 a,b), Pezza and Ambrizzi (2003) and Hoskins and Hodges (2005).

Based on this tracking technique advancement, it is now possible to define preferential patterns of storm tracks, not only for lower levels but also for upper-levels as in Hoskins and Hodges (2005, their figures 10 and 11) that present track density and mean intensity of cyclonic features for 250 and 850 hPa levels, respectively.

In the summer, there is a rather circular and well defined high-latitude storm track, approximately in 55 °S. In winter, it splits into a more asymmetric high-latitude track that migrates poleward and a mid-latitude track especially over the South Pacific. This behavior is in total agreement with the behavior of seasonal mean westerlies, as presented in Figure 2.2 and 2.4, and with the Rossby waves appearances and disappearances in the Hovmoller diagram of averaged frames (Figure 2.7).

After defining the principal cyclogenesis regions, the authors presented isolated statistics for each of the regions and in details for the systems initiated near 32 °S of South America (Hoskins and Hodges, 2005, their figures 7 and 6, respectively). Two facts drawn greater attention on their figure 6: the remarkable compactness of the distribution for a 45-yr period data and its positioning exactly over the SBS and SBCP.

The present picture of cyclogenesis over Western South Atlantic, reviewed in Reboita (2008), is then the existence of three very distinct regions of principal occurrence: a) south of Argentina (48 °S), more frequent during summer; b) off La Plata river (35 °S), more frequent in winter and spring and c) southeastern coast of Brazil (27 °S), more frequent during summer and with association to the convergence zone (SACZ).

In Figure 2.10 we reproduce these three clearly distinguishable regions of cyclogenesis, as obtained in the climatology presented by Reboita (2008) for the period between 1990/1999 and for systems with initial relative vorticity inferior to -1,5 x 10⁻⁵ s⁻¹. Densities are expressed as occurrences/km², in which unity represents approximately 25 systems.

This climatology was generated with the same NCEP Reanalysis surface wind data used in the present study and, therefore, these regions also represent the expected locations for the highest occurrences of wind-wave generation by the cyclones on our wave-model results.

2.3 Intraseasonal and interannual modulations

The low-passed series of surface winds, presented in Figure 2.9, show a marked intraseasonal signal with approximately 40 to 50 days period. In this particular year, this signal presents smaller amplitudes but it got increased to 10 m/s amplitude during the strong northeastern winds in springtime when the meridional winds attained approximately -10 m/s around day 230.

In this sense, this 40-50 days intraseasonal signal seems to modulate the synoptic events by making the events of positive phases (e.g. around day 200) to be completely different from the events of negative phases (e.g. around day 230), once the later almost do not generate the typical south/southwesterly winds.

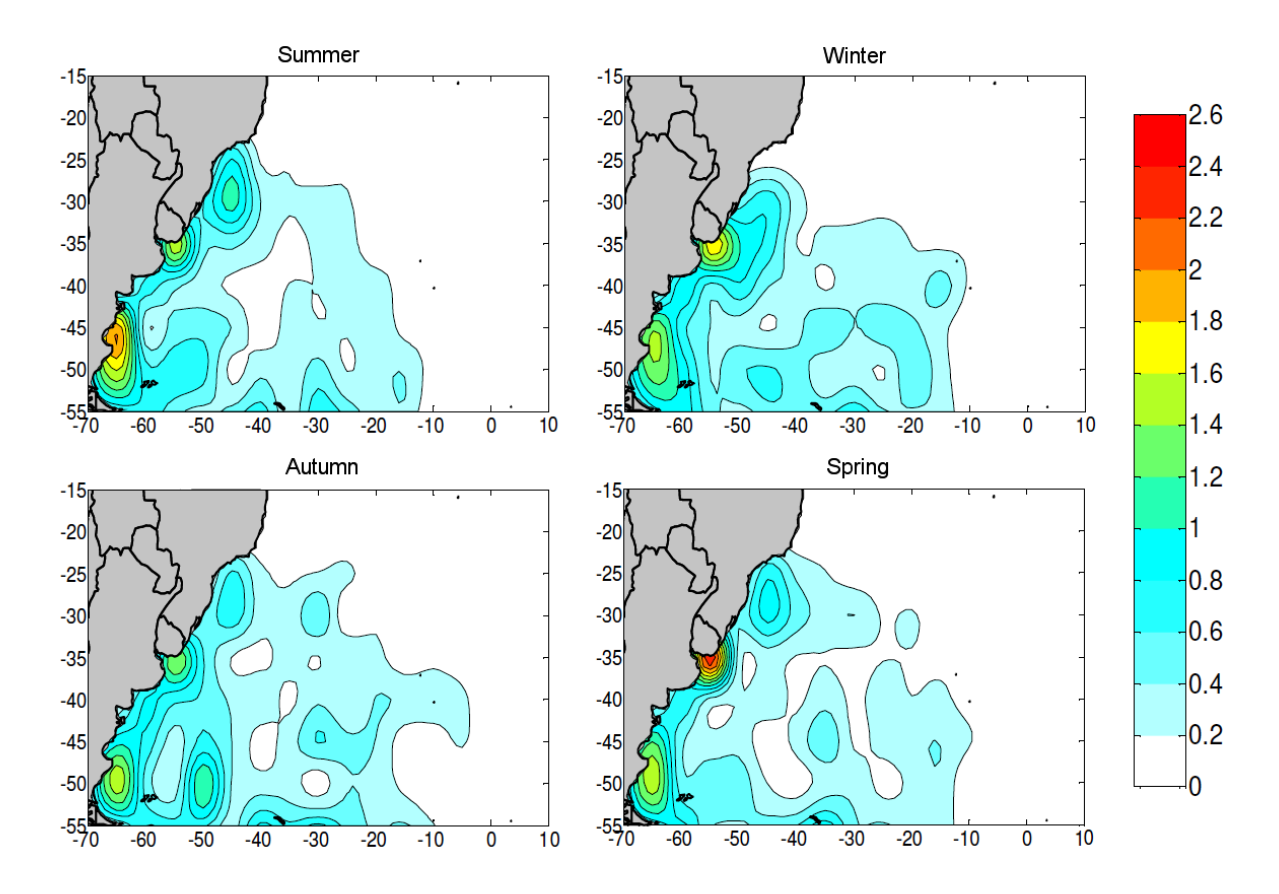


Figure 2.10: Western South Atlantic cyclogenesis climatology generated with NCEP Reanalysis surface wind data for the period between 1990/1999 and for systems with initial relative vorticity inferior to -1,5x10⁻⁵ s⁻¹. Densities are expressed as occurrences/km², in which unity represents approximately 25 systems. Reproduced from Reboita (2008).

Although the term intraseasonal (IS) variability actually refers to atmospheric oscillations with periods ranging from the synoptic scale up to 90 days, it has been the planetary-scale tropical oscillation with a 40 to 50 day period, called Madden-Julian Oscillation (MJO, Madden and Julian, 1994), which received the most substantial research, once it is considered the dominant mode of IS atmospheric variability within the tropical troposphere. These MJO-related circulation anomalies at low-latitudes are circumglobal and eastward flowing from the Indian Ocean, being primarily forced by heat exchanges with anomalies in tropical sea surface temperature (SST). A more recent MJO review is for instance found on Zhang (2005).

Regardless of this general greater global importance of MJO, over South America it was the impact over the SACZ of the higher frequency 15-20 days period oscillation, which is most times called submonthly in order to not be mistaken as the MJO, that received early attention. Casarin and Kousky (1986) reported the eastward propagation of outgoing longwave radiation anomalies in the region of SACZ and a cyclonic anomaly in the east coast. However, it was Nogués-Paegle and Mo (1997, their figure 9) who clearly defined the seesaw pattern with 15-20 days period on the SACZ.

Events with strong convective activity over the SACZ are associated with precipitation deficits over the subtropical plains of South America. In contrast, when the SACZ weakens, precipitation over these plains is abundant. Opposite patterns of low-level wind anomalies can

also be seen. Works like Liebmann et al. (1999), Nogués-Paegle et al. (2000), Herdies et al. (2002) and Carvalho et al. (2004) also discuss this submonthly oscillation of the SACZ.

Zhou and Lau (1998) and later Carvalho et al. (2002) and Jones and Carvalho (2002) reported the observed reversal between westerly and easterly wind regimes over Brazil within IS timescales. The later reported yet its occurrence in both frequencies: 10-30 and 30-70 days.

During westerly regimes, wind anomalies are observed from equator toward southeast Brazil closing the low-level cyclonic circulation. In contrast, during the easterly regimes an anticyclonic anomalous circulation is observed off the coast of Argentina and Uruguay with the wind anomalies crossing from southeast Brazil northwestward to the equator (Jones and Carvalho, 2002, their figure 7).

More recently, Souza and Ambrizzi (2006) described the IS modulation of precipitation over tropical Brazil and South Atlantic by the MJO. They also found that these features occur in association with a significant evolution of the lower-level wind and SST patterns. In their figure 8, we can see how easterly winds can occur aloft SBS and SPCP as a part of this cycle.

In order to define the local importance of the 40-50 days IS signal, we present in Figure 2.11 the distribution of the 40 days low-passed series of sea level pressure over the 23 years of our simulations (1990-2012) at two locations representatives of the northern and southern extremities of the SBS (black lines).

Superimposed over the major annual oscillations, which presents wintertime pressure maxima and summertime pressure minima, these long-term series of sea level pressure present the intense oscillations on IS timescale (40-50 days) that certainly affect the surface winds of SBS and which are even more frequent on the southern location. As far as we know, no previous work has pointed out the role of such wind oscillations over ocean wind-waves.

Whether or not this large signal of 40-50 days oscillations found in surface winds and sea level pressure over the SBS is exclusively due to the MJO remains an open question, though its timescale suggests so. Nevertheless, the recurrent observation of IS anomalous circulation extending from equator to the mid-latitudes of South America and western South Atlantic is a clear indicative of possible teleconnections between tropical and extratropical atmospheric circulations in this frequency.

In Figure 2.11, although we can say that IS oscillations are well distributed all along the series, it is also possible to see a variability on the annual oscillations, as some years appear as single peaks with sharp edges (e.g. 1992) in opposition to peaks cut off by strong IS oscillations that sometimes force the peaks to get even opposite to the typical annual winter pattern (e.g. 1997).

Measurements of the global MJO activity showed large year-to-year variations, with periods of strong activity followed by long periods in which the oscillation is weak or absent (Hendon et al., 1999; Zhang, 2005). As the Southern Oscillation (SO), also known as the coupled ocean-atmosphere El Niño Southern Oscillation (ENSO), is the principal mode of tropical interannual variability in the atmosphere, it was natural to expect for ENSO modulations on MJO.

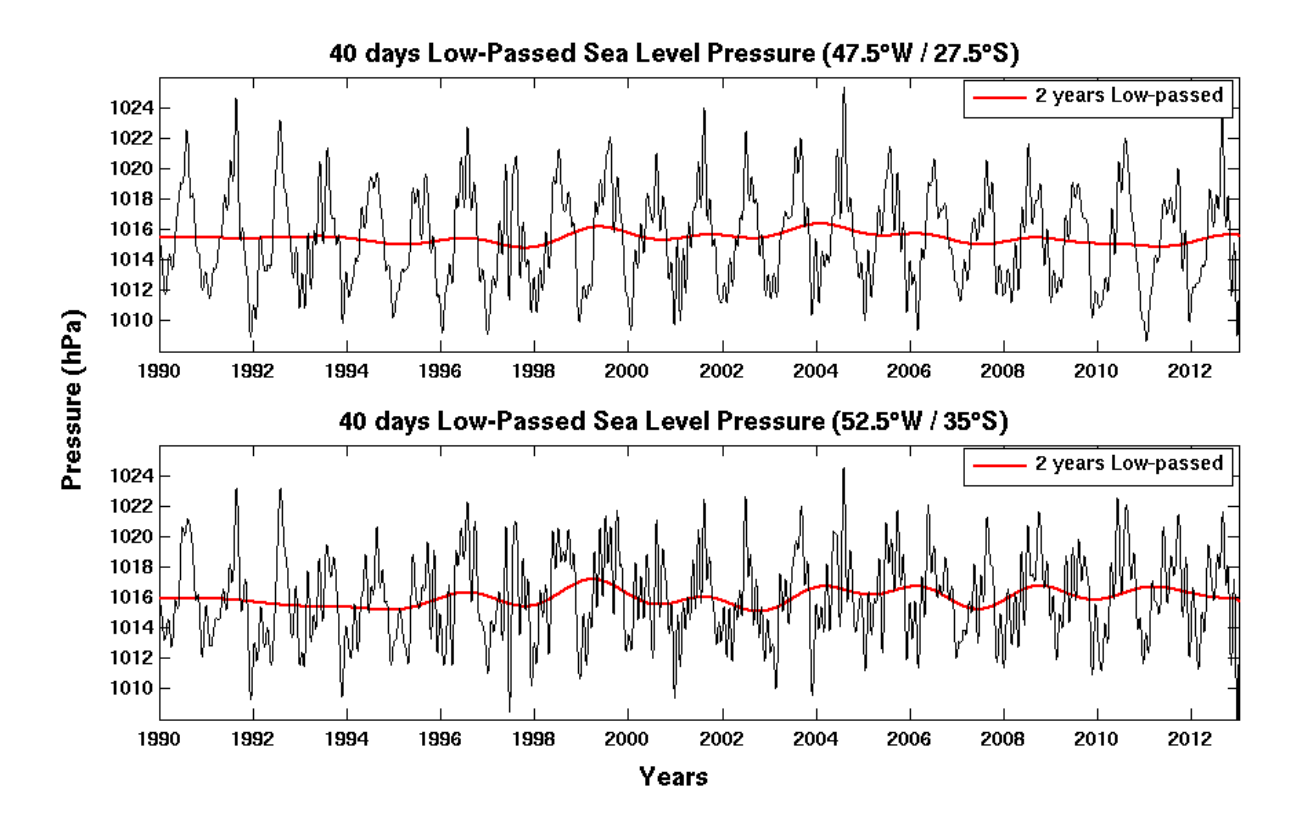


Figure 2.11: Forty days low-passed series of six-hourly sea level pressure between 1990/2012 (black lines), for locations representatives of the northern (top) and southern (bottom) extremities of SBS. Red lines show the 2 years low-passed series.

Initially, it was found that MJO anomalies propagation extends about 20° of longitude farther east during El Niño events, retreating westward during La Nina (e.g. Hendon et al., 1999; Kessler, 2001). However, interannual variation of the level of MJO activity during austral summer was found to exhibit little systematic relationship with ENSO (Hendon et al., 1999).

Later, observational and theoretical works showed that increased MJO activity actually often precedes and may significantly influence the establishment of ENSO (Hendon et al., 2007). Strong oscillating winds associated with MJO activity over the Pacific lead to a cooling of the western equatorial Pacific by increasing the ocean-atmosphere heat flux and upper-ocean mixing. At the same time they promote the advection of warmer waters eastward, weakening the zonal SST gradient (Kessler and Kleeman, 2000).

The most important consequence is the easterlies weakening, which help to complete the shift of the warmer waters eastward at the onset of El Niño. Similarly, the reduced MJO activity has been suggested to be associated with a strengthening of the easterlies and a contraction of warmer waters in the western Pacific, thus promoting the development of La Niña (Lau, 2005). Recent studies about MJO-ENSO relationship include yet McPhaden et al. (2006), Tang and Yu (2008), Moon et al. (2011) and Hoell et al. (2014), among others.

Whichever their relationship might be, in fact the statement that MJO activity is increased during strong ENSO events is found to be true for the SBS. Although the 40-50 days signals described here might not be fully MJO-related, they show the greatest oscillations exactly during the super El-Niño of 1997/98, which could be pointing to the existence of an influence from the

MJO-related anomalies.

Regarding direct interannual modulations, the interannual signal of sea level pressure (Figure 2.11, red lines), presents modest oscillation amplitudes during the whole 23 years period, with maximum amplitude of only 1.7 hPa between 1998/99. In Figure 2.12, we present the relation between both signals and the SO index (SOI), which is the monthly average sea level pressure difference between Tahiti and Darwin, demeaned and normalized by its standard deviation. Negative values of the SOI occur during El Niño (EN), positive values during La Niña (LN). To assist the subjective comparison, the adimensional SOI values (obtained at www.bom.gov.au) were smoothed with a 13 months running mean and divided by ten.

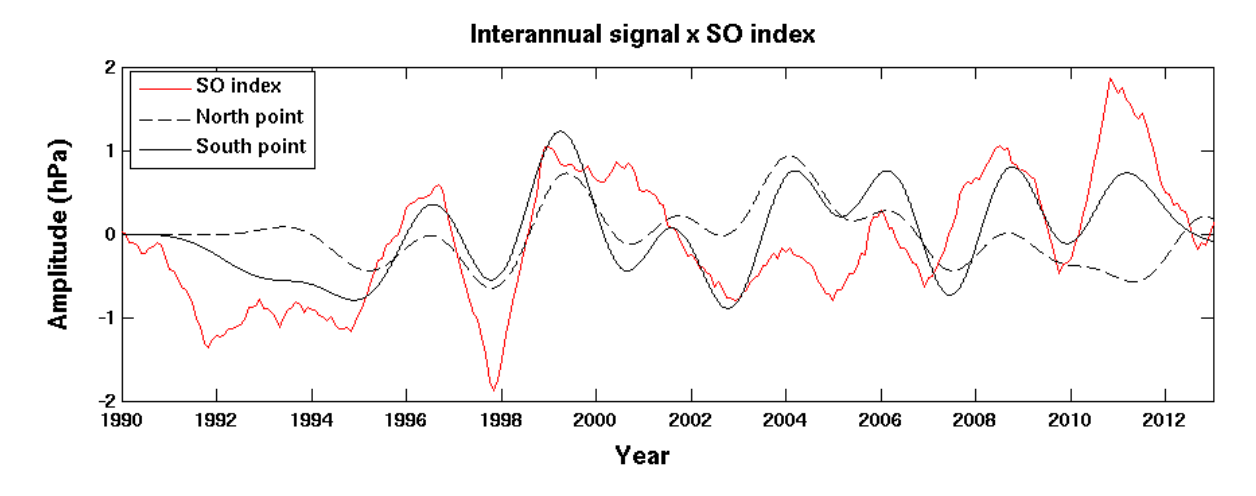


Figure 2.12: Comparison between the SO index (red) and the interannual signal at the two selected locations (black) representatives of the northern (dashed) and southern (line) extremities of SBS.

Even though the ENSO might be accepted as the dominant mode of interannual variability over southeastern South America, it certainly cannot explain all local variability and another forcings might have an influence. Correlations were then also tried with the Antarctic Oscillation (AAO), which is the leading mode of interannual variability in higher latitudes on the Southern Hemisphere (e.g. Mo, 2000; Thompson and Wallace, 2000) and known to occur over South America (Silvestre and Vera, 2003), but no significant cross-correlations with the NCEP AAO index was found.

Although the North and South points are "only" a thousand kilometers apart, the series responded very differently in near zero-lag cross-correlations against the SOI, with a good (0.65) correlation for the South point and none correlation (0.02) for the North point. Visual inspection, however, show that despite some general trending opposition (e.g. 2004-2012) that certainly lowered North point correlation, both series and the SOI present concomitant positive and negative peaks with 3 years periods, attesting the ENSO modulation. The higher correlation score of South point seems to be due to its better correlation with what looks like a 12 or 13 years cycle, whose maximums are approximately in 1999 and 2011 (LN) and minimums in 1993 and 2005 (EN).

During EN, subsidence prevails over central Brazil due to perturbed Walker circulation

while a pair of cyclonic (anticyclonic) nearly equivalent barotropic anomalies are produced by Rossby waves propagation over western (eastern) subtropical South America. At upper levels, these anomalies strengthen the subtropical jet stream and enhance the cyclonic advection over southeastern South America, providing dynamical support for ascending motion. Meanwhile, at lower levels the anticyclonic anomalies produce moisture divergence in central Brazil and enhance the LLJ east of the Andes and its northerly advection of moisture directed to western South Atlantic, producing strong precipitations on southern Brazil and Uruguay. Opposite anomalies prevail during LN episodes (Grimm et al., 2000 and Grimm, 2003, 2004).

Regarding the wind-wave generation over the SBS, it is reported that during summer EN events the easterly component of the surface flow is enhanced over Uruguay and central Argentina due to the southward shift of the SAH. Also, EN strengthening of the subtropical jet stream and subsidence over central Brazil act together, blocking the propagation of frontal systems farther north, for instance.

Both IS and interannual oscillations, together with the strong annual signal, are then expect to modulate the frequency and intensity of synoptic-scale events. The attempts to indentify this interannual variability of frontal systems, however, have mainly found a clear annual variation with a higher frequency of occurrence during winter than during summer (Cavalcanti and Kousky, 2009).

The interannual variation, reported by Andrade (2005) as 80 occurrences maximum (1984) and 51 occurrences minimum (2001) between 1980 and 2002, even though it does represent 36% of reduction, remains without correlation to an interannual index. No attempt has been made to address the role of IS oscillations, as averaging periods were usually seasonal or annual.

For the purpose of identify the variability of synoptic-scale events we present in Figures 2.13 and 2.14 the counting of events occurred at the same two locations used before. The full 23 years of six-hourly sea level pressure data was first demeaned with 30 hours running mean to remove the daily signal, then it was high-pass filtered with a 15 days cutting frequency and the events were counted by simple upward zero-crossing. The periods between the zero-crossings and the amplitudes of pressure change were then daily-interpolated and smoothed with a 15 days running mean, for clarity (black lines). Red lines show the 90 days running mean to help visualize longer variability.

In both figures it is possible to see the strong occurrence of higher frequency oscillations on the periods and amplitudes, when compared to the 90 days mean, making it clear the importance of IS modulations over synoptic-scale variability.

The annual signal is more evident in the amplitudes (Figure 2.13), which are generally lower farther north and present higher values in winter, between 11 and 15 hPa, than in summer, between 4 and 7 hPa, respectively for North and South points. This annual variability is not always easy to indentify, as some years even get opposite patterns during the center of winter (e.g. 1993) or no annual signal (e.g. 2002/03), which reveals the great interannual variations.

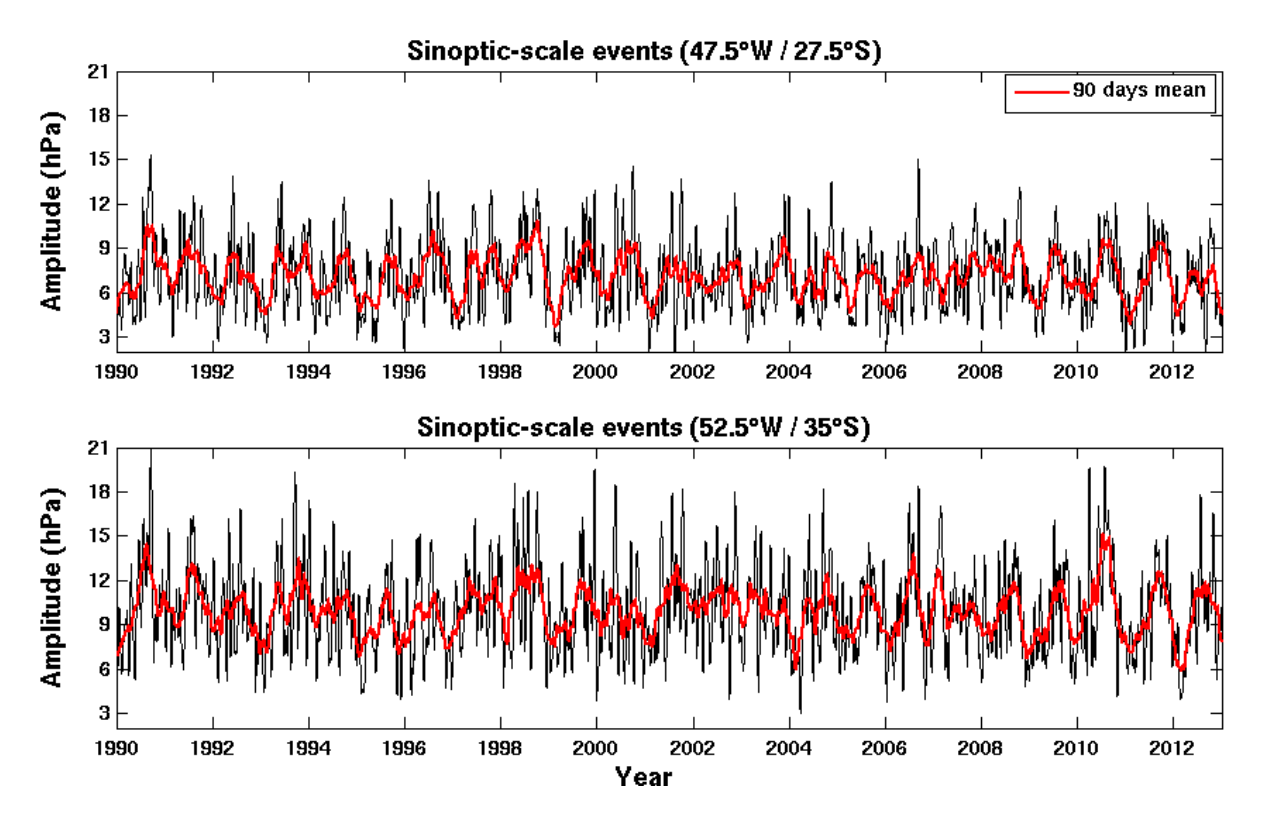


Figure 2.13: Amplitude variation of sea level pressure for individual synoptic-scale events between 1990/2012 (black lines) at two locations representatives of the northern (top) and southern (bottom) extremities of SBS. Red lines show the 90 days running means.

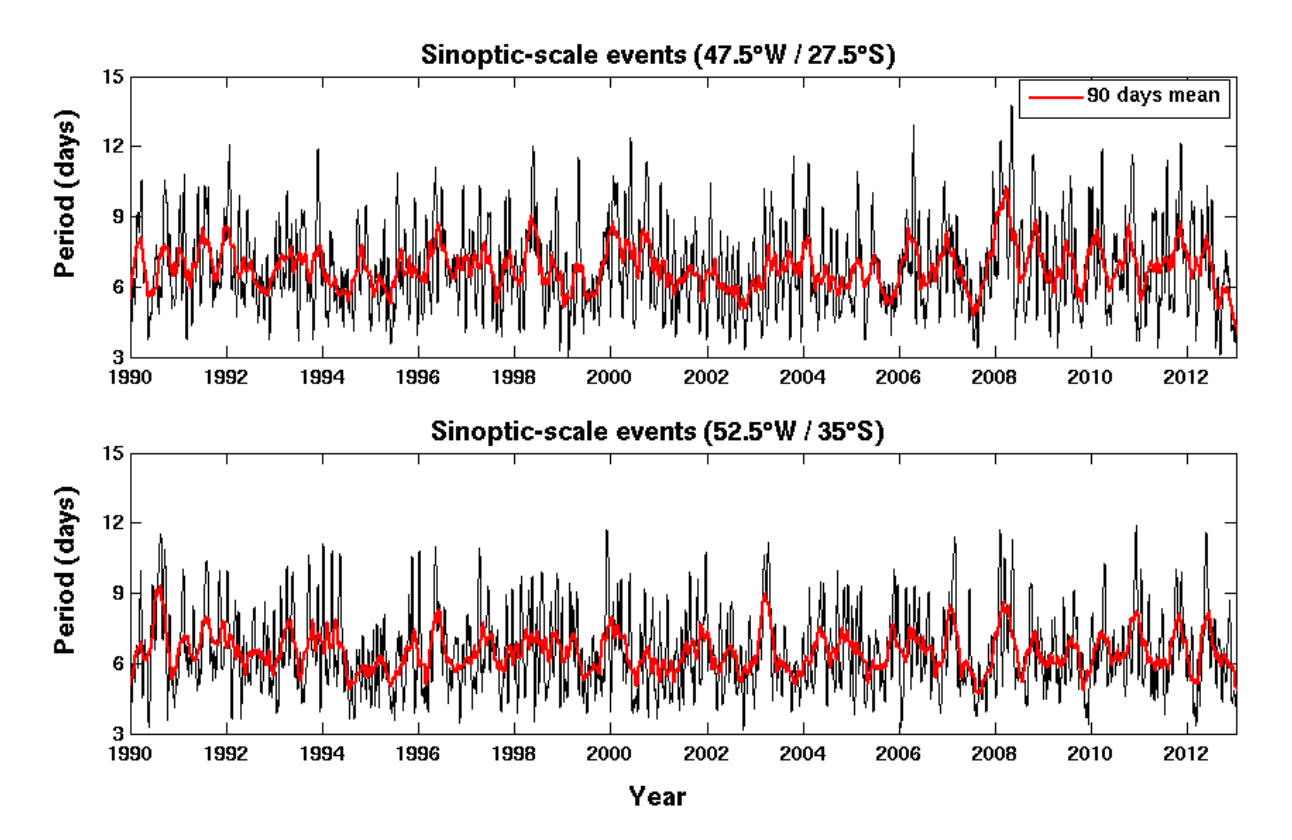


Figure 2.14: Period of individual synoptic-scale events between 1990/2012 (black line) at two locations representatives of the northern (top) and southern (bottom) extremities of SBS. Red lines show the 90 days running means.

The periods (Figure 2.14) vary between 5 and 10 days and no evident annual signal could be found. They present even stronger interannual variations compared with the amplitudes, showing sometimes rapid change of conditions (e.g. 2007/08 North point) or slow decay episodes (e.g. 2000/02 North point). As far as this counting is considered, no evident interannual pattern emerges from this synoptic-scale variability, which corroborates with previous works.

2.4 Concluding remarks

After presenting the scientific necessity of an ocean wind-wave climatology for the SBS, the present study examined the atmospheric conditions of SBS using diverse variables from the NCEP reanalysis long term mean (1981-2010) and also the six-hourly wind and sea level pressure data for the same period of the wind-wave simulations that will be presented in the following chapters (1990-2012).

Initially, we described the mean circulation over South America and western South Atlantic showing the strong influence of the monsoon and the subtropical convergence zone. After that, we typified the synoptic-scale events showing how eastward short-wavelength Rossby waves manifest themselves at surface as a succession of high and low pressure systems moving across South America, where they experience a marked anticyclonic turning and equatorward elongation while becoming disconnected from the upper-level trough and ridge, which continue to move eastward. A review on the three clearly distinguishable regions of cyclogenesis maxima over the western S. Atlantic was also presented, remarking the extreme proximity of two of them to the SBS.

We then showed how IS oscillations can not only directly modulate the surface winds and sea level pressure but also indirectly modulate the periods and amplitudes of the synoptic-scale events. Regarding the counting of synoptic-scale events, we have found strong annual variation in the amplitudes of pressure change and a northward decrease of its values. Periods however did not show this annual pattern. High interannual variability was certainly found in both amplitudes and periods but no evident pattern emerged.

We have also found a good correlation for sea level pressure and the SO index on interannual timescales, which attests the ENSO modulation, although the signal amplitude is considered low. There seems to be a 3 years period marked pace between the mean sea level pressure over SBS and the SO index and yet a secondary relation in larger timescales.

These results suggest that wind-waves over SBS at a given moment might indeed be controlled by IS modulations of both winds and synoptic-scale events, which has never been suggested before. Future works shall define the origins of this IS signal found over SBS and find out why the otherwise noticeable ENSO influence on frontal systems have not been found neither in our countings nor in previous works.

Chapter 3

Model description and validation

3.1 Numerical models

The high-resolution needed to correctly represent the shallow bathymetric features of the SBS makes it impossible the application of basin-scale wind-wave numerical models. Due to their use of explicit propagation schemes in geographical and spectral spaces, which are subject to the CFL criterion for numerical stability, spatial resolutions in the order of 100 m would require extremely short time steps.

To overcome this problem, we used the version 40.81 of wind-wave model "Simulating WAves Nearshore" (SWAN, Booij et al., 1999 and Ris et al., 1999) developed at Delft University of Technology (www.swan.tudelft.nl). SWAN is a third-generation fully spectral numerical wind-wave model based on the wave action balance equation with sources and sinks.

The bidimensional wave energy spectrum $E(\sigma, \vartheta)$, defined in frequency-direction domain, is usually described in wave models by this action density (N= E/σ), once it is conserved during propagation in the presence of currents. The evolution of the action density N (e.g. Komen et al., 1994) is governed by the action balance equation, which may be expressed in cartesian co-ordinates by:

$$\frac{\partial N}{\partial t} + \frac{\partial c_x N}{\partial x} + \frac{\partial c_y N}{\partial y} + \frac{\partial c_\sigma N}{\partial \sigma} + \frac{\partial c_\theta N}{\partial \theta} = \frac{S}{\sigma}$$

On the left-hand side of this equation the first term is the local derivative, the second and third terms denotes the propagation in two-dimensional geographical space and the fourth and fifth terms represent respectively the effects of frequency shifting and refraction, both due to depth or currents. The quantities c_x and c_y are the group velocities in geographical space and c_{σ} and c_{θ} are the propagation velocities in spectral space. All other physical processes are determined by source and sink terms directly inserted as empirical formulations in the term S on the right-hand side of the equation.

SWAN sources and sinks incorporate complete formulations for the deep water processes of wave generation, dissipation and interactions along with formulations for shallow water processes like setup, diffraction, bottom friction, non-linear interactions and depth-induced breaking.

Although it might possibly be used on any scale relevant for wind-waves, SWAN is just not efficient at larger scales. Actually, it was developed to provide users with robust and efficient calculations of wave processes in a regional high resolution spatial domain while accounting for incoming waves provided by boundary conditions. To accomplish this, it makes use of implicit numerical schemes which are unconditionally stable and therefore not subject to the CFL criterion.

As a direct consequence of its design for regional modeling, SWAN creates the necessity of wave spectra estimatives, to be used as boundary conditions. In the present study, these were obtained from former ran experiments using the third-generation basin-scale wind-wave model WAVEWATCH III version 2.22 (WW3, Tolman, 2002 and Tolman et al., 2002), retrieved from NCEP/NOAA (polar.ncep.noaa.gov). Aside from possible different source/sink term formulations, the WW3 governing equations also differ from SWAN's as the former solves the action balance equation in the wave number space, instead of frequency.

Both these models are presently utilized as valuable operational and research tools in different time and spatial scales, with relatively good skills (e.g. Rusu, 2011). Recent SWAN short-term applications on the SBS are found in Cuchiara et al. (2009) and Guimarães et al. (2014).

Regardless of their extensive history of successful applications, the details of wind-wave generation, dissipation and energy propagation across the spectrum are still not fully understood to be accurately quantified. In this sense, no wave model result should be used to draw any conclusion prior to a proper validation, ideally made through direct comparison against locally observed data.

3.2 Experiments grids and settings

All experiments were run from the beginning of 1990 to the end of 2012, thus comprehending a total of 23 years of simulations with six-hourly outputs or approximately 33600 different modeled conditions.

The models were forced by surface (10m) wind fields and ice cover data obtained from NCEP/NOAA Reanalysis (Kalnay et al., 1996) and retrieved from website (www.esrl.noaa.gov/psd) as six-hourly data with approximately 1.9° resolution.

The global bathymetric data used to generate all grids were obtained from General Bathymetric Chart of the Oceans (GEBCO, www.bodc.ac.uk). At western South Atlantic innershelves (< 50 m) the bathymetric data were digitalized from Brazilian and Argentinean Nautical Charts.

Three regular grids were one-way nested within the basin-scale model (WW3). The Global grid (not shown) provides boundary conditions for the South Atlantic grid (Figure 3.1, left) which, by its turn, provides boundary conditions to the Western South Atlantic grid, whose open boundaries are depicted as red lines in Figure 3.1 (left).

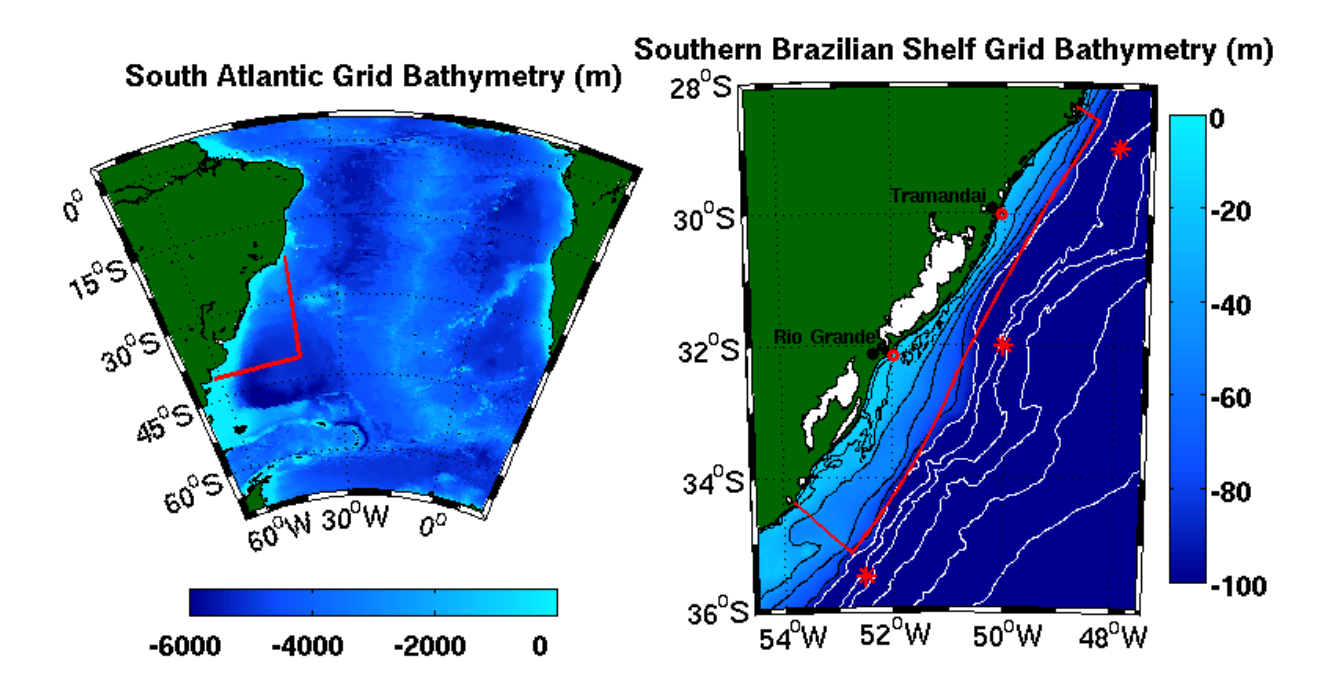


Figure 3.1: Bathymetric grids used in the simulations. Large-scale South Atlantic and Western South Atlantic grids used in WW3 (left) and Shelf and Coastal grids used in SWAN (right). Red lines are the boundary contour of nested grids. In the Shelf grid the black isolines are for 12, 20, 40, 60 and 80 m depth and white isolines are for 100, 200, 1000, 2000, 3000 and 4000 m depth. Red asterisks are the points chosen to validate the WW3 results and red circles are the positions of wave-buoy data used in SWAN validation.

The Global grid has 1° resolution in both directions. It is limited between 75 °S and 65 °N and is circumglobal between 240 °W and 120 °E, in the sense that energy propagating against this boundary appears in the opposite side of the domain. This is especially important as it excludes the need for open boundary conditions in this grid, enabling the utilization of this entire modeling system without any wave data input.

The South Atlantic grid has 0.4° resolution in both directions and is defined between 68.4 °W and 20.4 °E and between 72 °S and 6.4 °N. The spectra used in open boundaries in the Southern Ocean and in the tropics between South America and Africa were obtained from Global grid with 0.4° intervals, matching the positions of the S. Atlantic grid open boundary points.

The Western South Atlantic grid has 0.1° resolution in both directions and is defined between 53.8 °W and 42 °W and between 34.3 °S and 22.9 °S. The spectra of its open boundaries were obtained from S. Atlantic grid also with 0.1° resolution and matching the grid points.

The three grids were discretized in the spectral domain with 36 directions, yielding 10° direction resolution, and with 26 frequencies that grow exponentially from 0.04 with factor 1.1 (default). All other user-adjustable parameters were also set using default values.

In WW3 the action balance equation is solved using a fractional step method. The global time step in which the entire solution is propagated in time, the wavenumber grid is updated and input data are interpolated was chosen to be 3600 s for all three grids.

The time step for spatial propagation, which defines the maximum time step for the lowest

frequency, was chosen with decreasing values of 1200, 900 and 300 s, respectively for Global, S. Atlantic and W.S. Atlantic grids, in pursuit of numerical stability and as a direct consequence of increasing spatial resolution. The time step for intra-spectral propagation was also chosen with decreasing values of 3600, 1800 and 1200 s, which allow for numerical stability in refraction facing this increasing resolution.

Finally, the dynamic time step for source term integration was chosen as 300 s in all three grids for two reasons: it is recommended to be approximately 10 % of global time step and it is the value of the lowest time step of spatial propagation.

Two more grids were then nested within the regional model (SWAN). The Shelf grid is regular with 2 km resolution in both directions and it is defined between 54.5 °W and 47.5 °W and between 36 °S and 28.1 °S (Figure 3.1, right), making use of the boundary conditions provided by the W. S. Atlantic grid (WW3) with 0.1° resolution.

The curvilinear Coastal grid has 200 x 1000 points with variable resolution between 800 m and 1.2 km and it was approximately fitted between the shoreline and the 100 m isobath of the SBS (Figure 3.1, right, red line). Open boundary conditions were provided by the Shelf grid results with resolution of ten Coastal grid points.

Both grids were discretized with 25 frequencies that grow exponentially from 0.05 to 0.5. The Shelf grid was discretized in the full circle directional domain with 72 directions and the Coastal grid with 54 directions in a sector between 0° and 270°, both of them yielding 5° resolution in directions. All remaining user-adjustable parameters were also set using default values, unless clearly stated otherwise.

The final configuration is thus a five levels one-way full downscaling (global to local) long-term wind-wave modeling system centered on the SBS. Worthwhile to notice that such long-term full downscaling has never been accomplished by previous works in the region. Map animations of six-hourly simulations of significant wave height and mean directions for the 23 years can be found in our project website (www.renatocecilio.org).

3.3 Model validation

Numerical models are made to extrapolate the otherwise limited observed data, so much in space as in time. Therefore, realistic modeling like ours should not be utilized to draw any conclusion without the proper assessment of the model skill or, in other words, how much this model reproduces the local reality, which is usually called model validation or verification.

3.3.1 Basin-scale

In this sense and given the lack of wave-buoy data in South Atlantic, we propose the validation of our basin-scale model results through the use of orbital altimetry. To accomplish this task we have made use of the daily mean significant wave height as obtained after a careful compilation of different orbital altimetry missions, provided by the AVISO group (www.aviso.altimetry.fr)

with 1° resolution on a global grid. Map animations of these remotely sensed data can also be found in our project website.

The direct comparison (i.e. same point and time) between the sig. wave height of altimetry data and the daily means of our global WW3 results is presented in the following three figures for the period between 2010 and 2012.

The time series of daily mean sig. wave height for three points representing the north, central and south portions of the shelf break of SBS (Figure 3.1, red asterisks), as obtained with our WW3 simulations on the Global grid and as observed with altimetry data, are shown in Figure 3.2.

Subjective analysis reveals an outstanding reproduction of observations with greatest errors in the underestimation of lower energy waves, which shows northward increase, and also in the overestimation of extreme peaks in the South point. The well-marked annual cycle of summertime lower waves was, however, reproduced precisely.

In Figure 3.3 we show the global maps with the annual means of sig. wave height as obtained with our WW3 simulations on the Global grid (left) and as observed with altimetry data (right). The resemblance is remarkable and differences are only seen under a second inspection.

Highest mean waves occur in mid-to-high latitudes (45-60 °S) of southern hemisphere and secondarily in the North Atlantic and North Pacific, with lowest waves occurring along the tropics and in semi-enclosed shelves or seas. Interannual variations are also followed like, for instance, the intensification in North Atlantic during 2011 and the progressive lowering of mean height in South Pacific.

In Figure 3.4 are presented the global maps with the annual mean differences between modeled (Hm) and observed (Ho) sig. wave heights as calculated by the Mean Absolute Error (MAE) and by the mean of absolute error relative to observed values, called Relative MAE (RMAE), that is here subjectively qualified as very poor, poor, regular and very good agreement for each 25 %:

$$MAE = \frac{1}{n} \sum_{1}^{n} |Hm - Ho|; \qquad RMAE = \frac{1}{n} \sum_{1}^{n} \frac{|Hm - Ho|}{Ho};$$

Lowest differences were found along the tropics and greatest differences were found in the vicinity of Antarctic sea ice border (>1 m) and in mid-to-high latitudes (0.7-0.8 m) where waves were also usually higher. The RMAE calculation adjusts this distortion giving approximately 20-25 % error in mid-to-high latitudes and 10 % error in the tropics, showing that global model results can be considered as in very good agreement with observations.

The same procedure is follow for direct comparisons between S. Atlantic grid results and the altimetry data that were previously interpolated to the 0.4° resolution S. Atlantic grid. No comparison was made with the 0.1° resolution W. S. Atlantic grid as altimetry data would then be composed by too much interpolation.

The daily mean time series comparisons (Figure 3.5) show the same outstanding reproduction of observations found in the global results and, in fact, appear to have the very same mentioned flaws (i.e. underestimation of lower energy waves increasing northward and overestimation of extreme peaks in the South point).

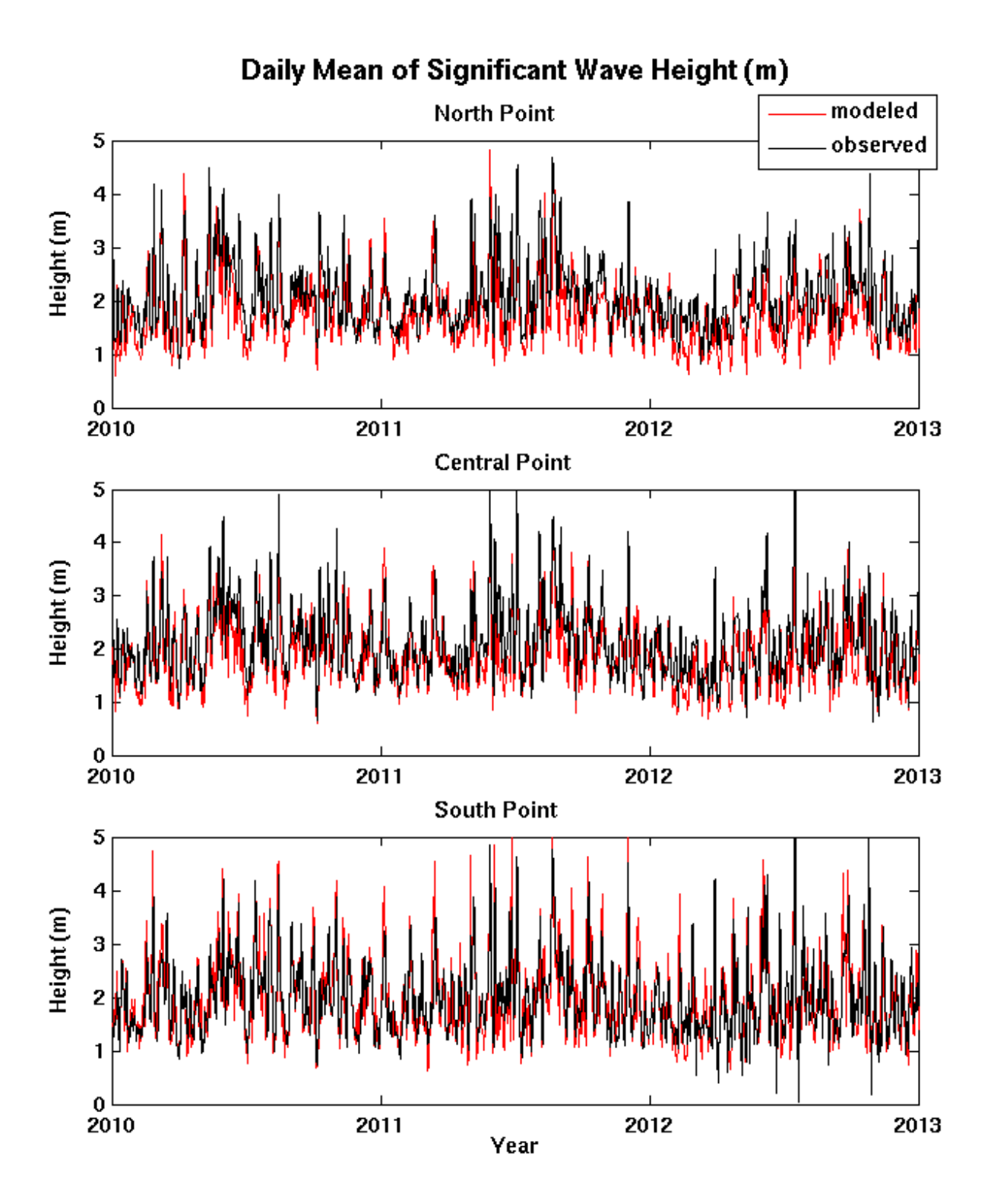


Figure 3.2: Time series of daily mean significant wave height for three points representing the north, central and south portions of the shelf break of SBS (Figure 3.1, red asterisks), as obtained with our WW3 simulations on the Global grid (red lines) and as observed with altimetry data (black lines).

The annual means of sig. wave height (Figure 3.6), as obtained with our WW3 simulations on the S. Atlantic grid (left) and as observed with altimetry data (right), show how the waves in South Atlantic can be divided in two realms by the $40\,^{\circ}$ S latitude, north of which we find mean waves lower than 3 m.

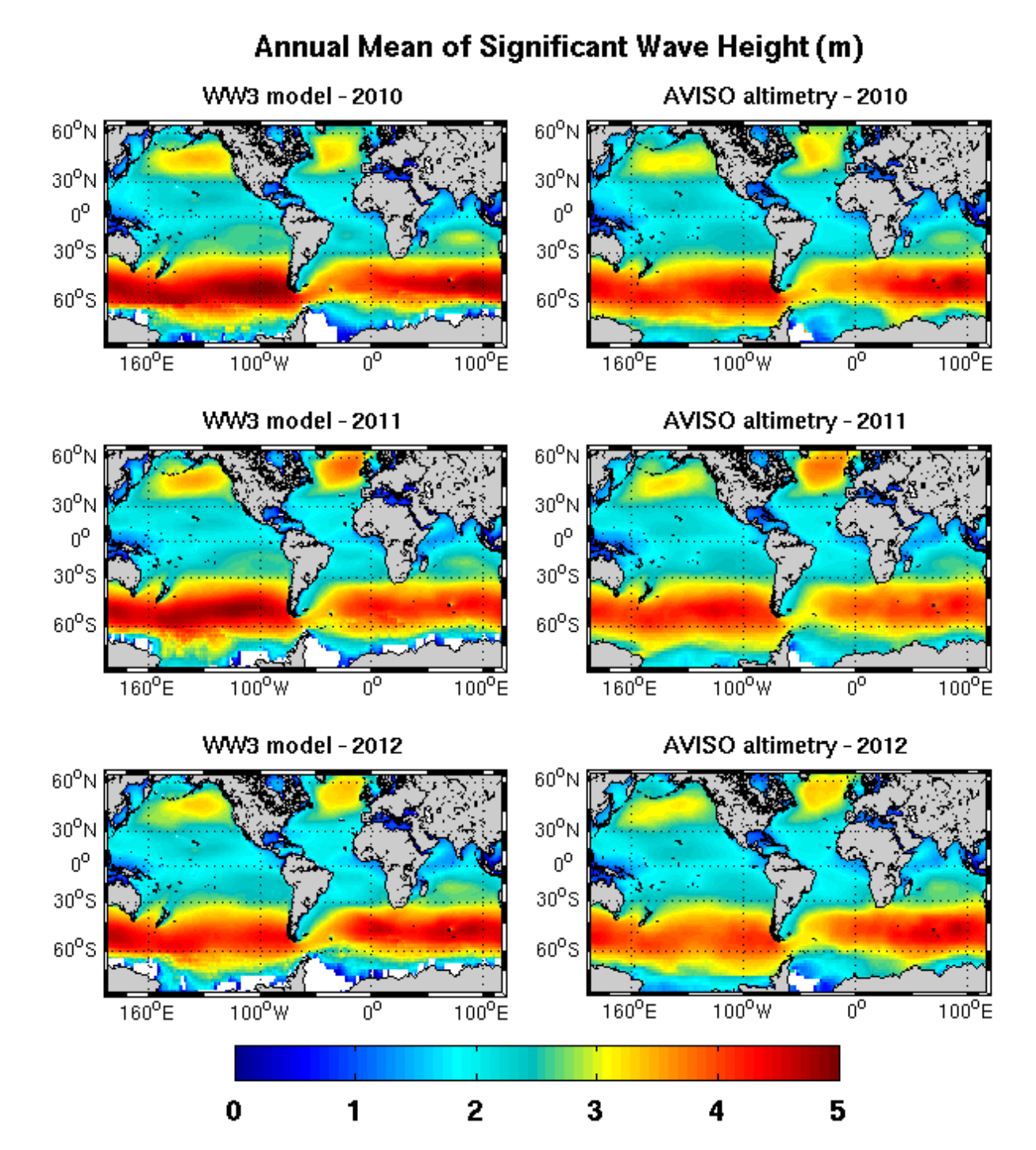


Figure 3.3: Annual mean of significant wave height as obtained with our WW3 simulations on the Global grid (left) and as observed with altimetry data (right).

The zonal differences appear as a direct consequence of limited fetch, with the lower waves in western South Atlantic being caused by the limited fetch of westerlies due to S. America blocking of the South Pacific waves and with the lower waves in the equator near Africa being caused by the limited fetch of the tropical easterlies.

The S. Atlantic grid maps of annual MAE and RMAE are presented in Figure 3.7. Greatest MAE were also found in mid-to-high latitudes, with approximately the same values of global results (0.7-0.8 m), but now the substantial differences found in the tropical South Atlantic during 2010 (0.6 m) are made clearer by the increased resolution.

Mean Absolute Error (m) and Relative Mean Absolute Error (%)

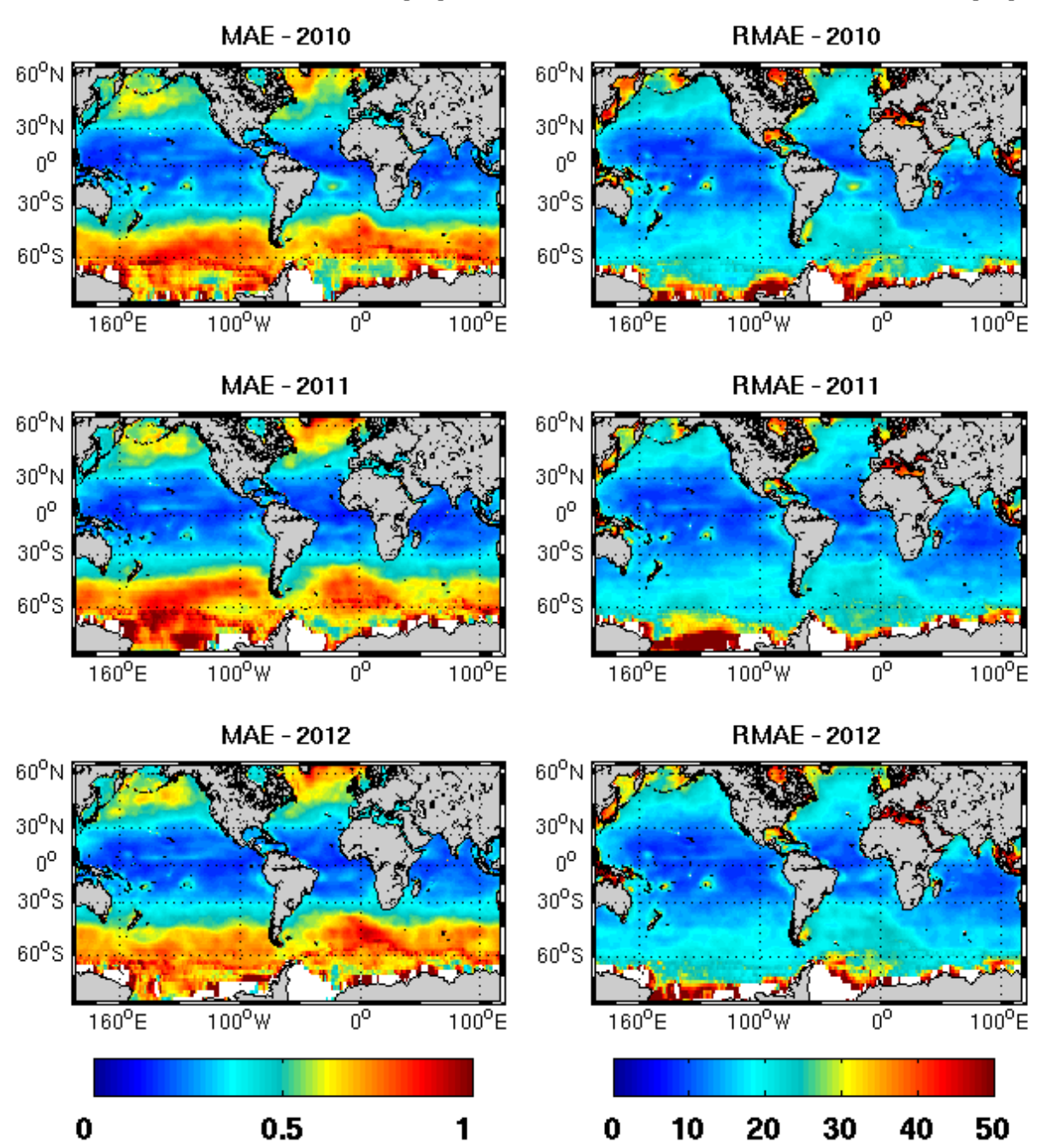


Figure 3.4: Annual mean absolute error (MAE, left) and annual mean of relative absolute error (RMAE, right) between model results and observations of daily mean significant wave height.

The vicinity of Antarctic sea ice border during 2010 and 2012 (> 50 %) and the Patagonian shelf during 2010 and 2011 (35 %) presented elevated RMAE values revealing the major drawback of relative error: it grows exponentially as a consequence of low observed values in the formulae denominator, caused in this case respectively by differences in the sea ice covering between modeled and observed altimetry data and by the Malvinas Island sheltering that was not correctly reproduced in the model due to resolution issues.

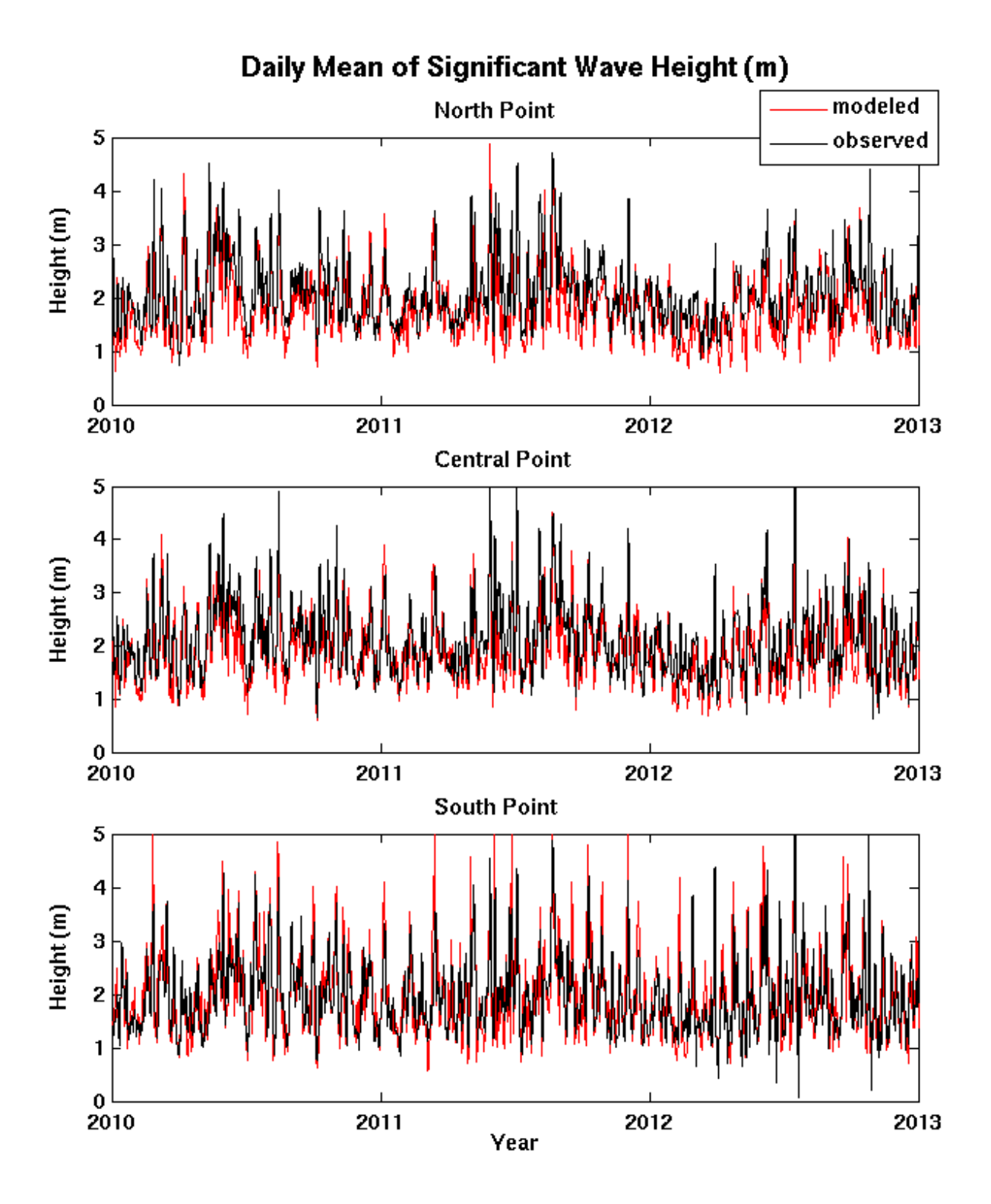


Figure 3.5: Time series of daily mean significant wave height for three points representing the north, central and south portions of the shelf break of SBS (Figure 3.1, red asterisks), as obtained with our WW3 simulations on the S. Atlantic grid (red lines) and as observed with altimetry data (black lines).

Excluding these localized errors, the RMAE show values of approximately 20-25 % error in mid-to-high latitudes and 10 % error in the tropics with exception of the values in the tropic during 2010 (30 %). These values show that model results on the S. Atlantic grid can also be considered as in very good agreement with observations.

Annual Mean of Significant Wave Height (m) WW3 model - 2010 AVISO altimetry - 2010 T.C. W. WW3 model - 2011 AVISO altimetry - 2011 ᡥ W W. atr 4D°VÝ <u>~~</u> 40°₩ WW3 model - 2012 AVISO altimetry - 2012 ď W. W.

Figure 3.6: Annual mean of significant wave height as obtained with our WW3 simulations on the S. Atlantic grid (left) and as observed with altimetry data (right).

2

аŒ

3

4D°VV

5

4

аĆ

 $\widetilde{40}^{0}$ VV

0

1

Finally, we present in Figure 3.8 the statistics for the time series comparison (Figures 3.2 and 3.5) on the Global (left) and S. Atlantic (right) grids expressed in the form of density scatter plot and regression analysis. The results of both grids present remarkable similarities confirming the subjective resemblance previously stated and defining that increasing grid resolution does not necessarily change the model skill.

Mean Absolute Error (m) and Relative Mean Absolute Error (%)

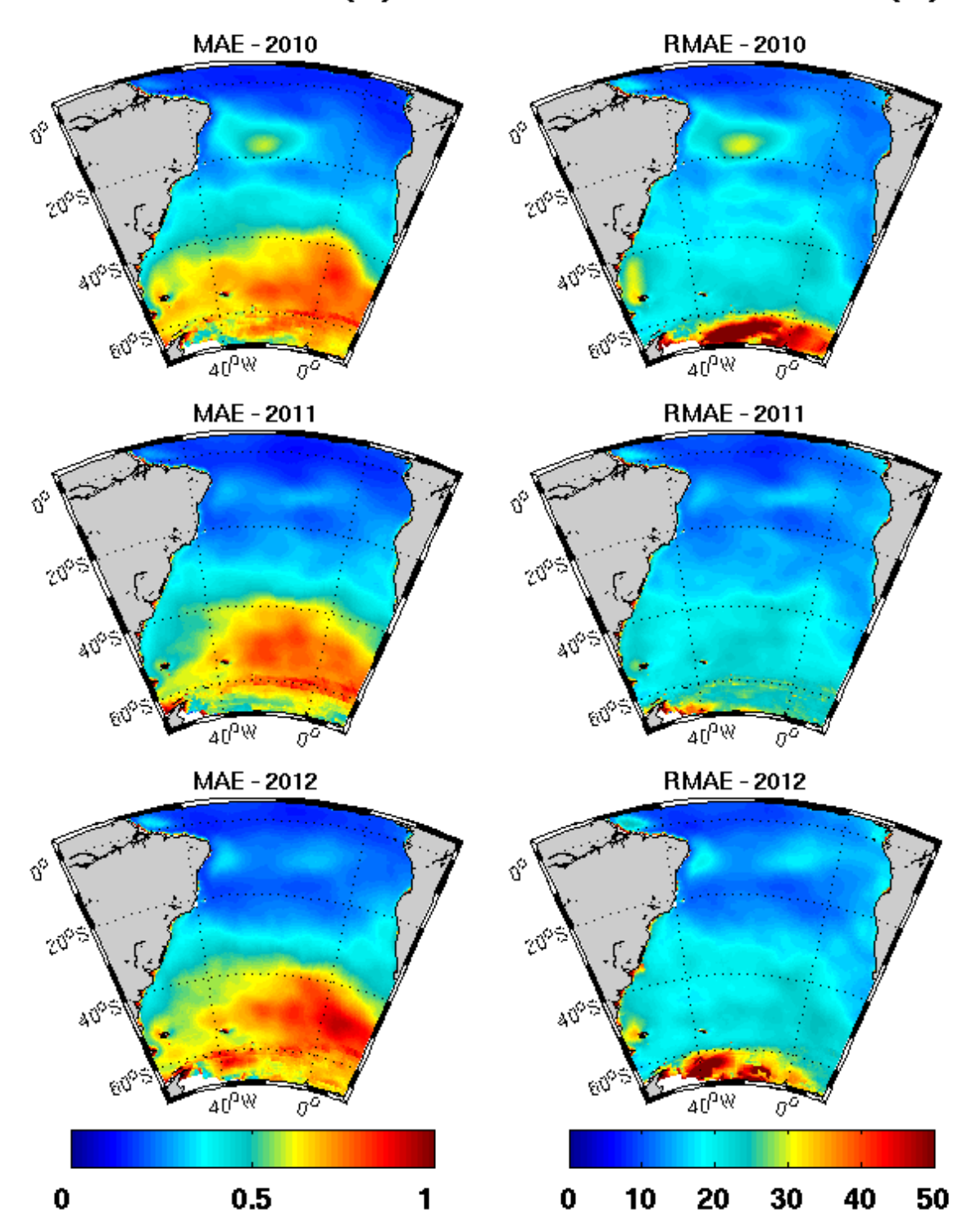


Figure 3.7: Annual mean absolute error (MAE, left) and annual mean of relative absolute error (RMAE, right) between model results and observations of daily mean significant wave height.

The higher densities are found mostly over or near the equality line corroborating with the statement that modeled sig. heights are in very good agreement with observations. The northward increase in the model underestimation of lower waves is seen in the higher density clouds positioning slightly above the equality line.

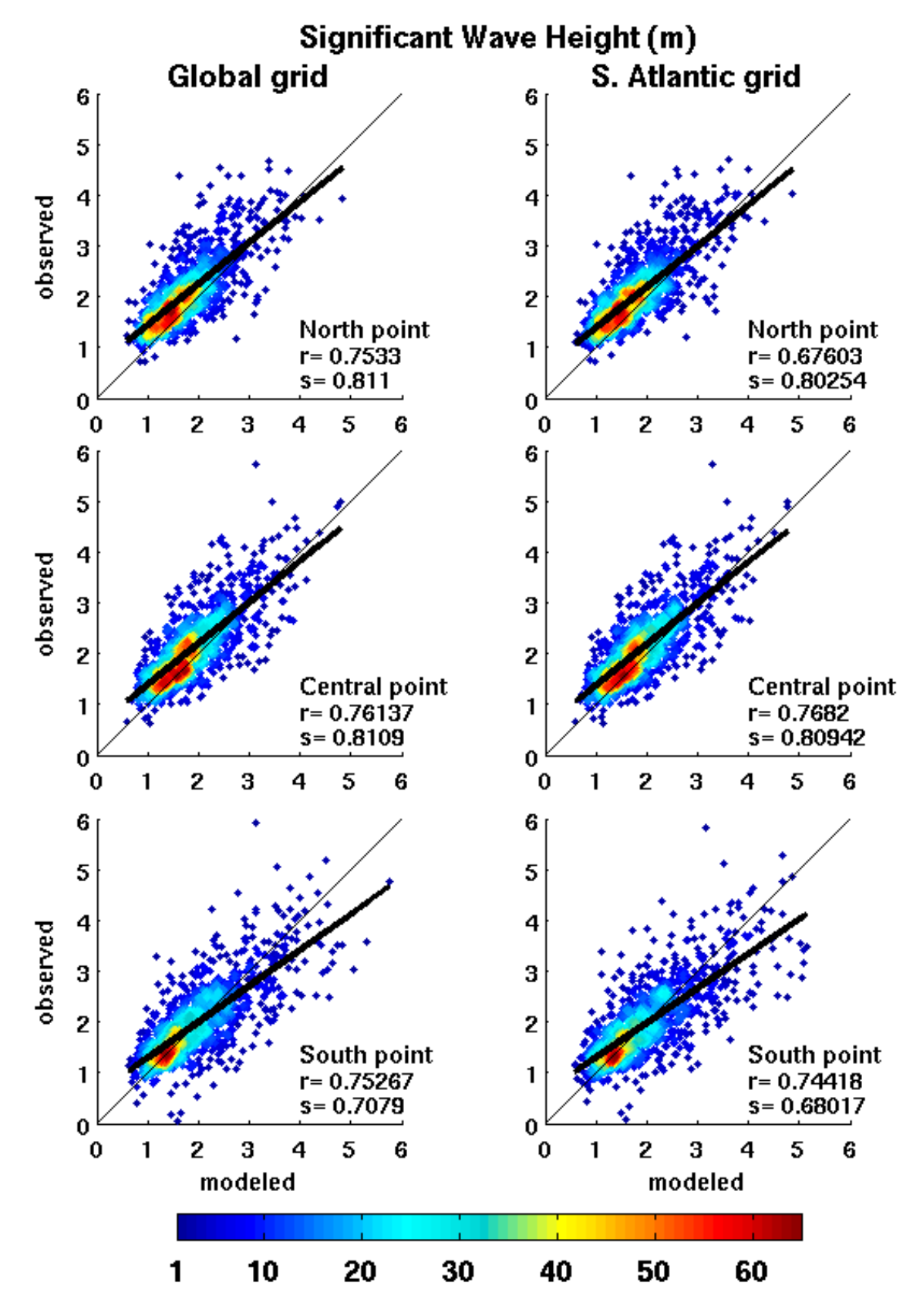


Figure 3.8: Density scatter plot with direct comparisons of daily mean significant wave height for three points representing the north, central and south portions of the shelf break of SBS (Figure 3.1, red asterisks), as obtained with our WW3 simulations on the Global (left) and S. Atlantic grid (right) versus the observed altimetry data. The colors represent the number of occurrences in a square with 0.1 m side. Regression line (thick black), its slope (s) and the correlation between the series (r) are also shown.

Regression lines show slopes lower than unity reflecting this underestimation of lower waves in Central and North points (s=0.8) and also the overestimation of higher waves in the South point, where regression slopes drop to 0.7. Correlations were also high for all points (\sim 0.75) with a minimum of 0.67 in the North point of S. Atlantic grid.

Bearing in mind the high inherent uncertainties associated with both remotely sensed data and model results, the overall low differences found between them in maps and time series statistics are considered at least encouraging, in the sense that wave heights near the shelf break of SBS can effectively be reproduced mainly using default WW3 simulations with NCEP wind reanalysis.

Periods and directions, however, were not validated against observed data and, therefore, we had no means to access the model skill in the reproduction of these wave statistics over the shelf-break of SBS. Future works shall deal with that limitation, thus enhancing our capacity to validate our basin-scale wind-wave model results.

3.3.2 Regional-scale

In order to evaluate the performance of the regional model we made use of the only two wave-buoy dataset available in the region, previously described in Strauch et al. (2009). First dataset was obtained off Rio Grande city, close to the mouth of the Patos lagoon at 17 m depth, for intermittent periods between 1996 and 1999 in a total of 7376 observations. The second dataset was obtained off Tramandaí city at 17.5 m depth for intermittent periods between 2006 and 2007 and totalizes 2250 observations (Figure 3.1, red circles).

The raw data of both datasets were submitted to the same statistical procedure: significant height and peak period were obtained by zero-crossing following Tucker and Pitt (2001) and peak direction was obtained by spectral method following Hashimoto (1997).

In Figure 3.9 we present the direct comparisons of wave statistics between our SWAN simulations on the Shelf grid versus the two observed wave-buoy datasets: Rio Grande (left) and Tramandaí (right). The sig. heights show the higher density areas positioned over or near the equality line, which represent a very good agreement, and the correlations are high (0.81 and 0.7) reflecting this general agreement in most of the data. There is, although, an underestimation of the higher waves by the model, especially in Rio Grande data, with the regression slopes resulting in values greater than unity (1.36 and 1.09).

As with the sig. height, the peak periods show higher density areas positioned over or near the equality line and, therefore, are also considered as in a very good agreement with observations. Regression slopes get values lower than unity (0.77 and 0.55) in response to some overestimation of high-period waves by the model and also due to time-lags or non-representations of some events in the wind data. Correlations are also higher in Rio Grande (0.68 and 0.59) suggesting that those misrepresentations of peak period are higher near Tramandaí.

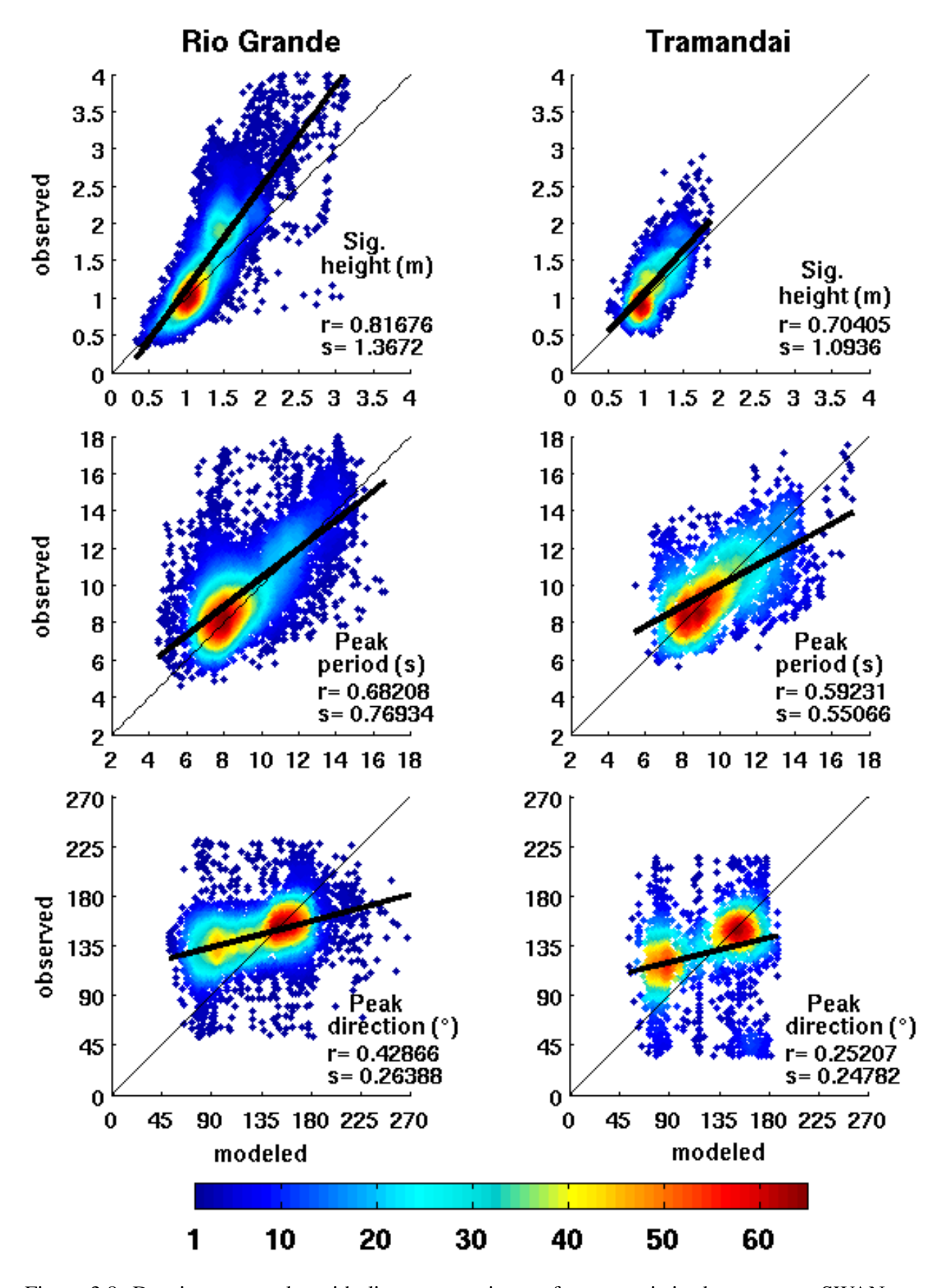


Figure 3.9: Density scatter plot with direct comparisons of wave statistics between our SWAN simulations on the Shelf grid versus the two observed wave-buoy datasets: Rio Grande (left) and Tramandai (right). The colors represent the number of occurrences in a square with 0.1 m, 1 s or 0.1 pi radians side, respectively for heights, periods and directions. Regression line (thick black), its slope (s) and the correlation between the series (r) are also shown.

The peak directions, however, show strong deviations from the equality line, very low correlations (0.42 and 0.25) and regression slopes (0.26 and 0.24), which automatically classify these results as in poor or very poor agreement with observations. However, the higher density region centered in 150-160° (SSE) closely fits the equality line and it is only the second region that is centered between 110° and 150° (ESE and SE) in the observed values of Rio Grande and between 100° and 135° (ESE) in the observed values of Tramandaí that is erroneously represented by the model as approximately 90-100° (E) in Rio Grande data and 70-90° (ENE) in Tramandaí data, in approximately a 20-30° error in the minimum angle.

In Figures 3.10 and 3.11 we show how this non-reproduction of the ESE and SE waves by the model strongly affects the representations on bidimensional wave diagrams. These diagrams instantly make clear that model results have very much less variability than the observations, as the later appear always much more scattered all over the diagrams.

In the Rio Grande dataset (Figure 3.10), we can see how the observed waves distribution in the top diagram present a triagular shape with values contained between 0.5 m and a straight line between 1 m and 5 s and 4 m and 11 s, with the higher density (e.g. light blue contour) located between 6 and 11 s and between 0.5 and 2.3 m, approximately. The distribution of model results remind that triangular shape, but concentrate its values near 7 s period and 1 m height. Extreme events are shown as dark blue scattered points in the upper-right corner of the cloud of points, attaining values between 4 m and 12 s and between 3 m and 18 s, and were absolutely not reproduced by the model. The peak directions in model results show the clear bimodal pattern already pointed out, while the observations are clearly centered near 140° (SE), which is approximately the local coastline normal orientation.

In the Tramandaí dataset (Figure 3.11) the higher density of observed waves in the top diagram is located between 7 and 12 s from 0.7 m to 1.5 m, attaining 2 m between 9 and 11 s. As with Rio Grande dataset, here also the top diagram show a triangular shape "opening" from 1 m and 5 s in direction to higher and longer waves. The distribution of model results, by its turn, barely pass 1.5 m sig. height and the higher density area concentrates in the 7 s peak period, although spreading for the same interval than observations (6 to 15 s) and showing even 17 s peak period waves eventually reproduced. The pattern on modeled peak directions is also similar to the one found in Rio Grande dataset as they are bimodal and with missing higher waves, while the observations are centered near SE, but with greater ESE component.

Rather than stochastic, these large errors found in wave peak directions reveal a clear systematic pattern, once they repeat themselves in time and in both datasets originated from different locations, which strongly suggests the misrepresentation of some physical process or forcing.

Two factors could be in the core of this problem: a coarse grid resolution not enabling the necessary refraction to occur or else a selective over-attenuation of the longer waves, making the energy peaks from SE disappear and leaving only ENE lower and shorter waves in the spectra.

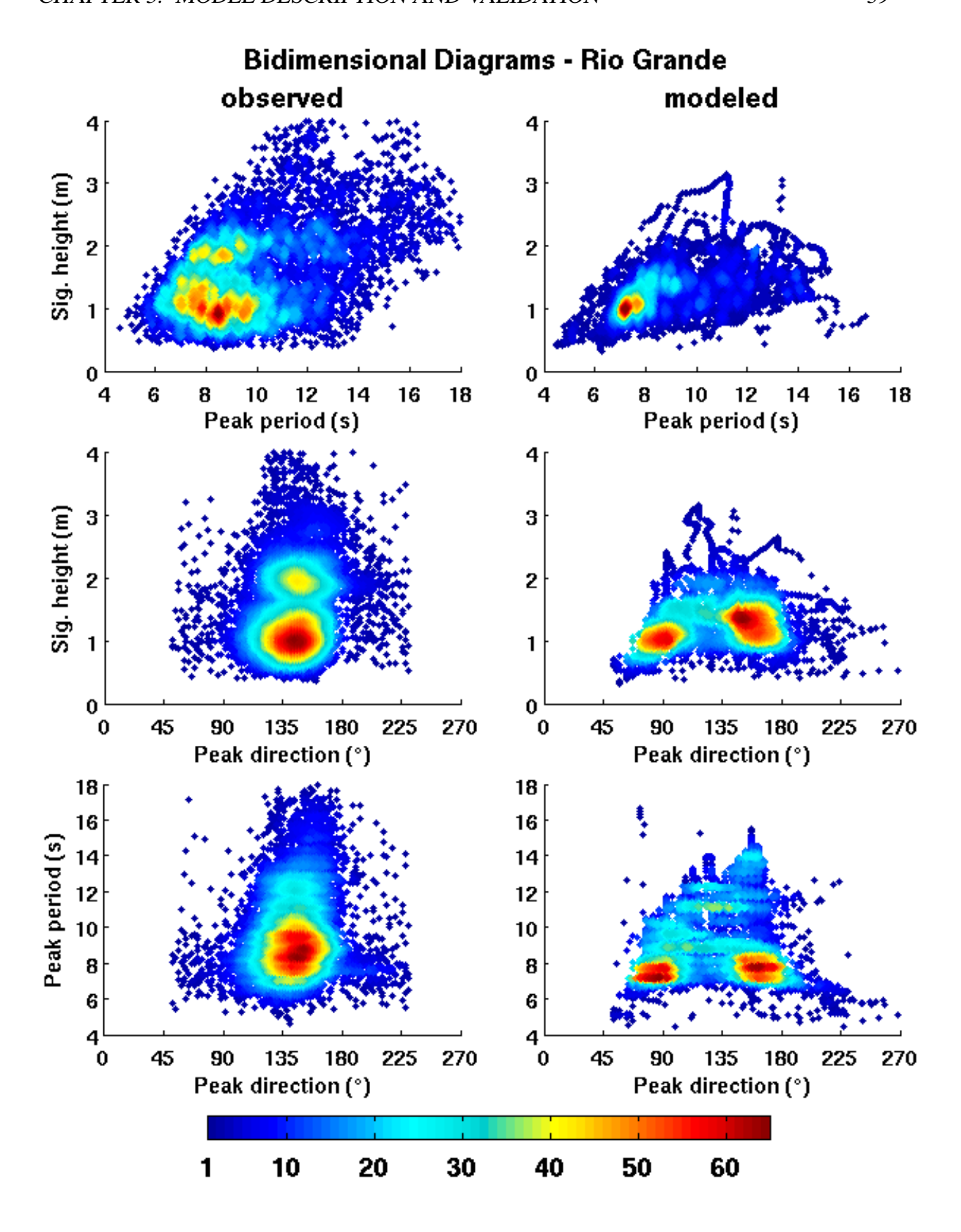


Figure 3.10: Density scatter plot showing bidimensional diagrams of wave statistics, as observed with the wave-buoy dataset of Rio Grande (left) versus our SWAN simulations on the Shelf grid (right). The colors represent the number of occurrences in a square with 0.1 m, s or pi radians side, respectively for heights, periods and directions.

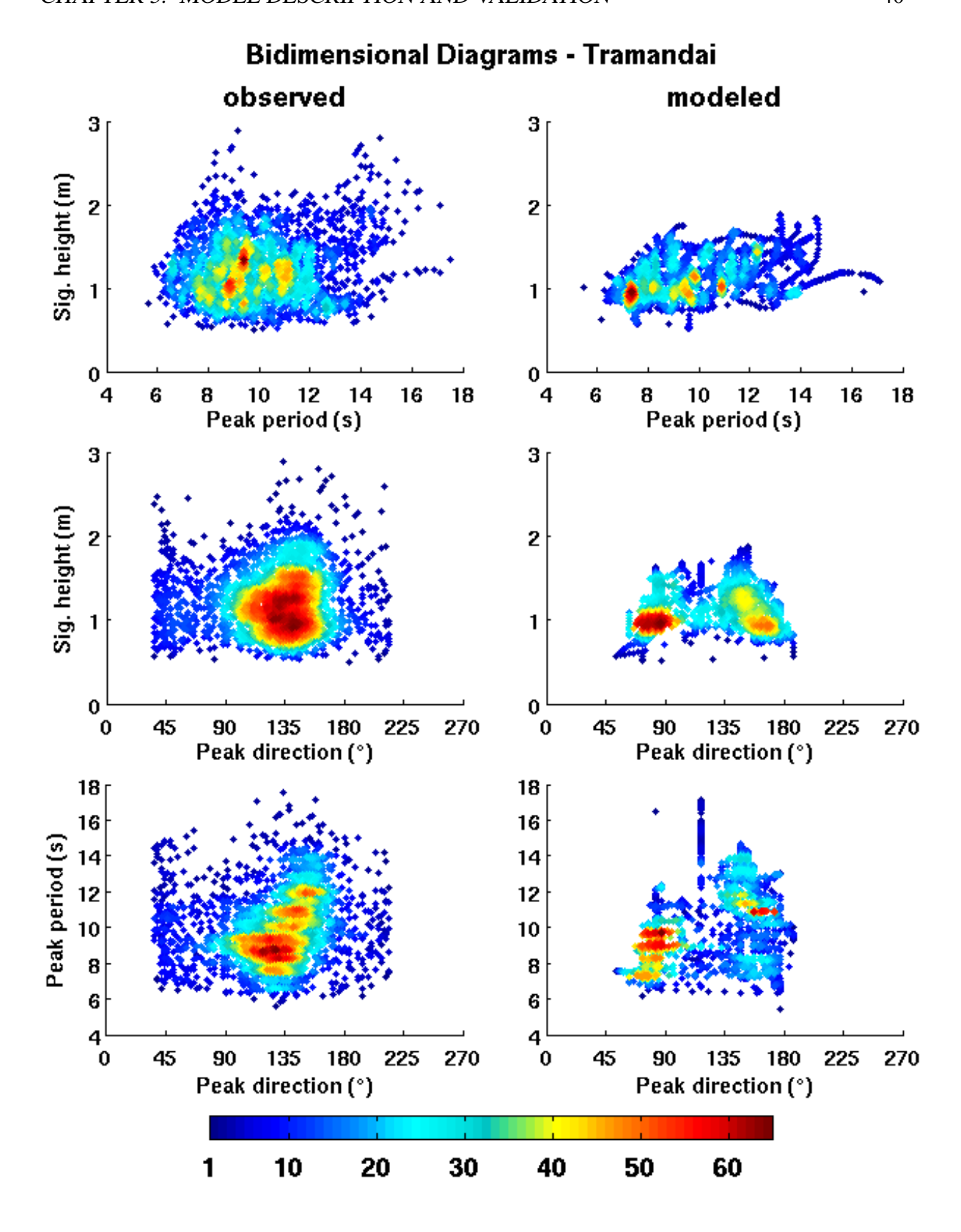


Figure 3.11: Density scatter plot showing bidimensional diagrams of wave statistics, as observed with the wave-buoy dataset of Tramandai (left) versus our SWAN simulations on the Shelf grid (right). The colors represent the number of occurrences in a square with 0.1 m, s or pi radians side, respectively for heights, periods and directions.

In this sense, rather than incorrectly calculating an inexistent ENE wave, the model would be then just underestimating the SE waves, leading therefore to the excessive occurrences of peak directions out of the remaining ENE wave energy. The alternative is that these ENE waves were already incorrectly produced by the basin-scale model WW3, which then transferred this error downwards through the boundaries conditions.

With the purpose of testing the possibility of either spatial resolution or physical parameters influence on the wave model skill, we ran four different experiments on the curvilinear Coastal grid. The first experiment has default configuration, as ran on the Shelf grid, and its results will be used to point out the possible necessity of a finer resolution in order to better represent the exponential shoreface geometry. The second experiment was set with smaller JONSWAP bottom friction parameter (0.038), recommended for swell conditions instead of the default value of 0.067, aiming to decrease the above mentioned over-attenuation of higher waves. Third and fourth experiments were set respectively as the first and second but with wind grow turned off in order to point out the role of local winds on the final shape of wave spectra.

The density scatter plots with direct comparisons of sig. height (Figure 3.12), peak period (Figure 3.13) and peak direction (Figure 3.14) between these four experiments and the two observed wave-buoy datasets show much more similarities than differences. In Tables 3.1 to 3.3 we present the values obtained in the four experiments for correlations and regression slopes, along with their results of MAE and RMAE.

In the sig. heights comparison we can see how the simulations without wind grow (exp. 3 and 4) have usually worse performance when compared with the first two experiments. Even so, they also respond to the pattern of changes found in the first two, which present better agreement than in experiment on the Shelf grid when using default configuration (exp. 1) and even better in the experiment with less bottom friction (exp. 2), whose regression slopes get very near the equality line in the Rio Grande dataset and closely fit it in the case of Tramandai dataset.

In peak periods the very good performance of the previous Shelf grid was maintained, also with worse reproduction of high peak periods in Tramandai. However, although experiments with wind have performed better in the Rio Grande dataset, the opposite is true for Tramandai, which presented better correlations and regression slopes in the no-wind experiments. Of special importance are the waves observed with 13 s and modeled with 7 s that got itself adjusted in the fourth experiment showing that local wind near Tramandai does effectively affect the modeled peak periods while in Rio Grande it does affect less. Besides, its non adjustment in the third experiment reassures the lower bottom friction configuration overall better performance.

Peak directions were also very similar to those found on the Shelf grid, with the experiments without winds presenting a better adjustment of the higher density centered in SSE in the Tramandai dataset. However, the greatest differences are in the Rio Grande dataset where the reduction of density for the ENE waves in the no-wind experiments is large enough to confirm that local winds also effectively affect the modeled peak directions. Moreover, the waves from SE are also more usually seen in these no-wind conditions, attesting that the energy of local waves might have overruled some SE waves energy as previously mentioned.

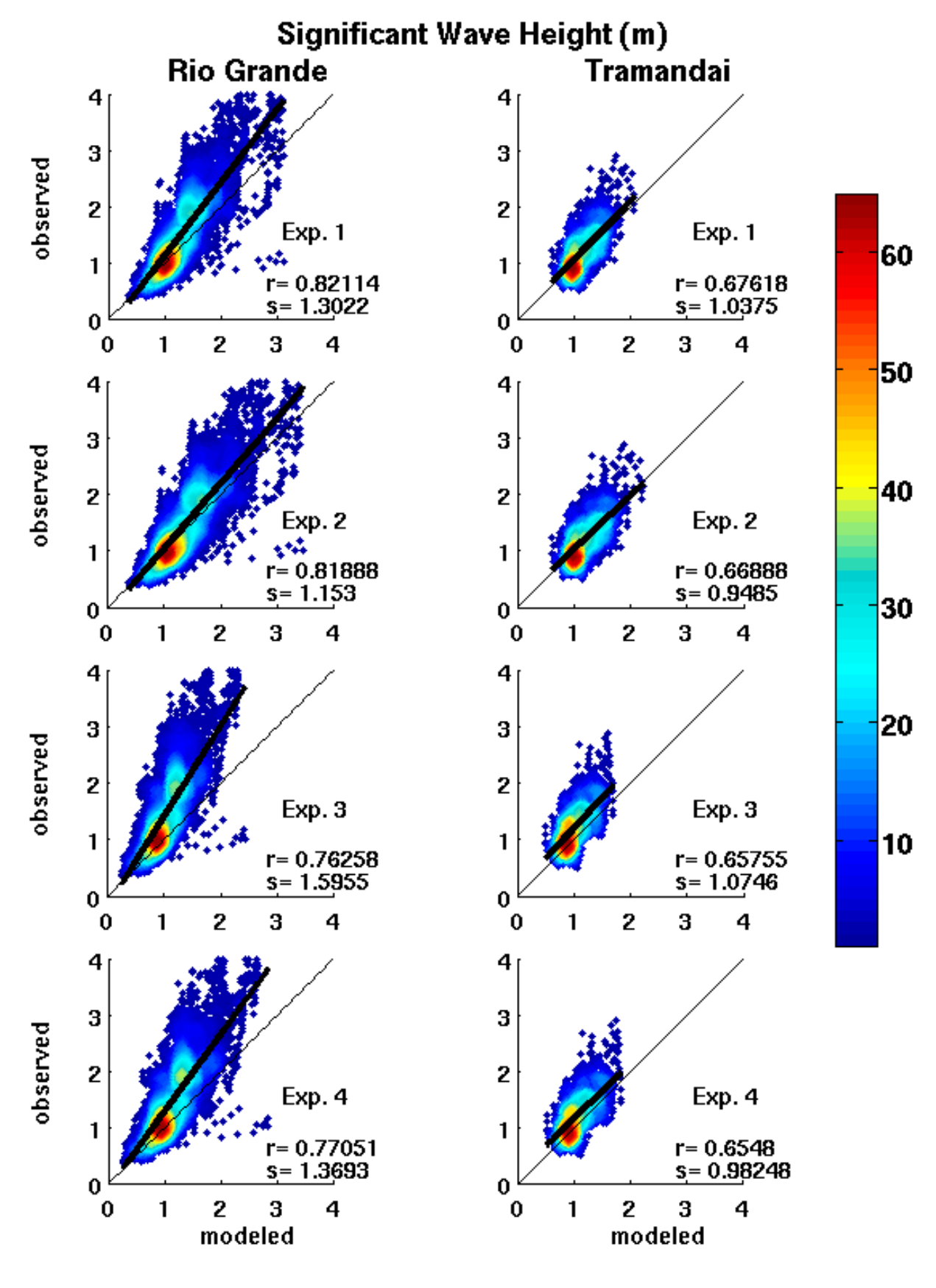


Figure 3.12: Density scatter plot with direct comparisons of significant wave height between the four SWAN experiments ran on the curvilinear Coastal grid versus the two observed wavebuoy datasets: Rio Grande (left) and Tramandai (right). The colors represent the number of occurrences in a square with 0.1 m side. Regression line (thick black), its slope (s) and the correlation between the series (r) are also shown.

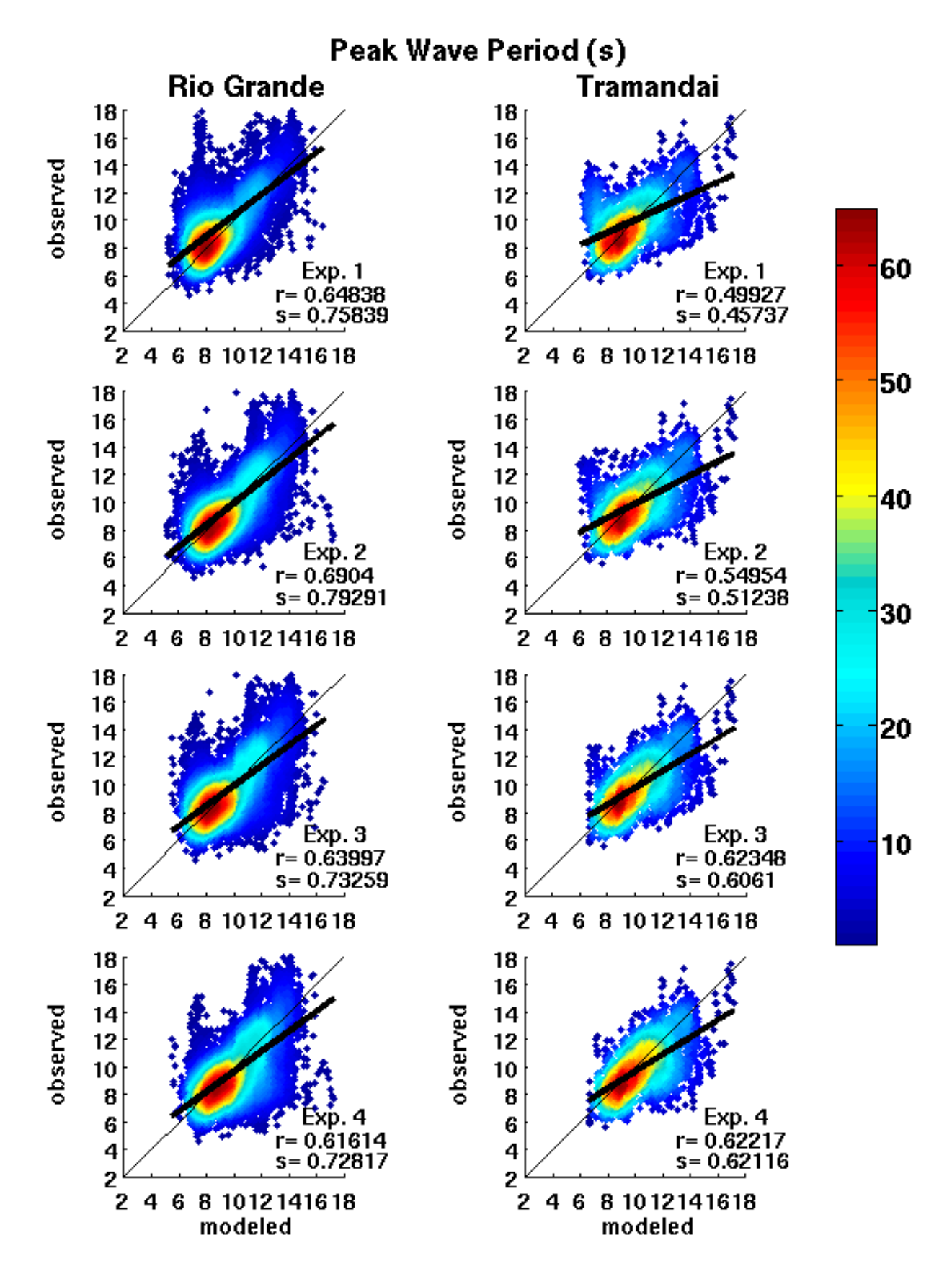


Figure 3.13: Density scatter plot with direct comparisons of peak wave period between the four SWAN experiments ran on the curvilinear Coastal grid versus the two observed wave-buoy datasets: Rio Grande (left) and Tramandai (right). The colors represent the number of occurrences in a square with 1 s side. Regression line (thick black), its slope (s) and the correlation between the series (r) are also shown.

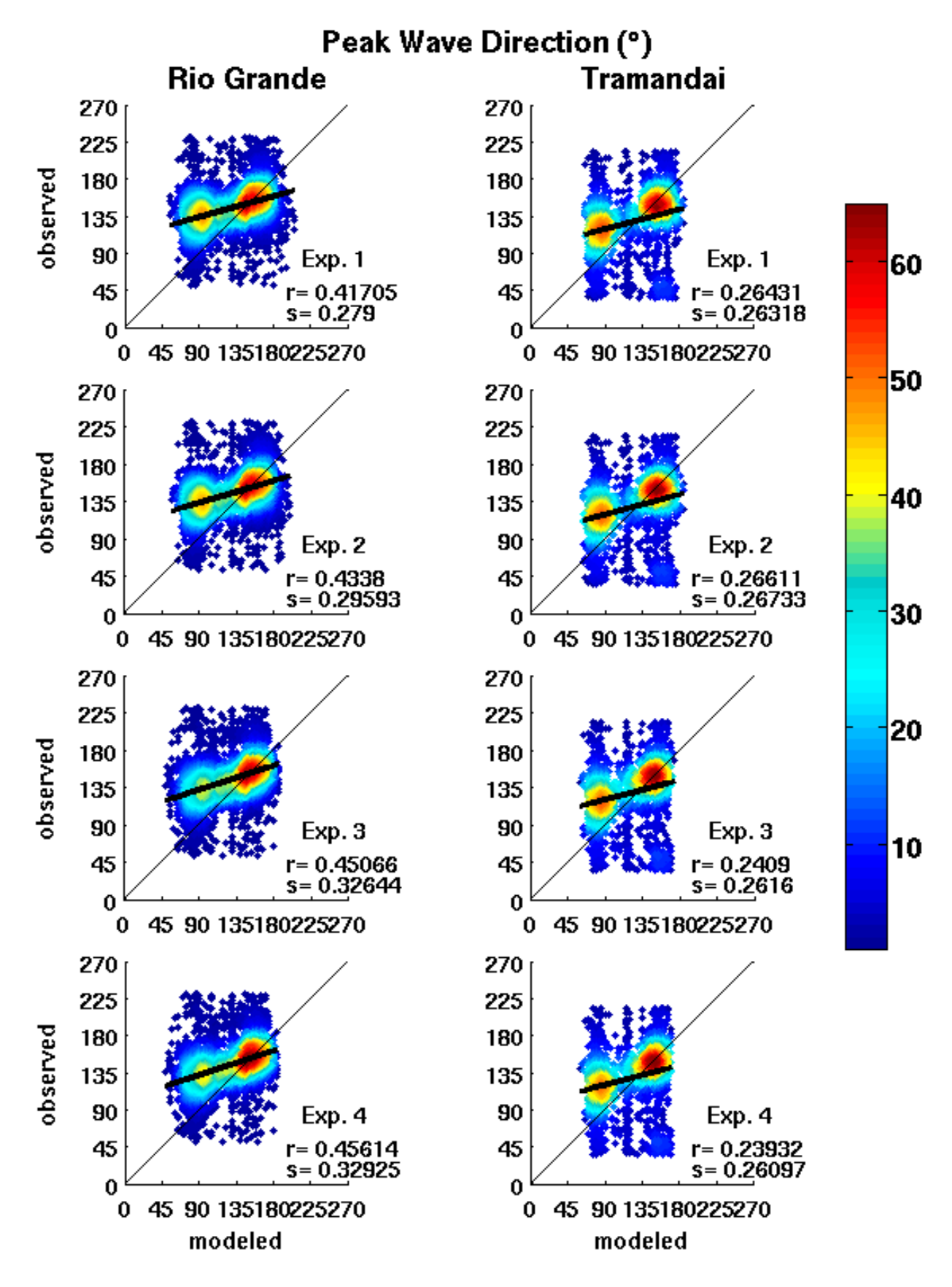


Figure 3.14: Density scatter plot with direct comparisons of peak wave direction between the four SWAN experiments ran on the curvilinear Coastal grid versus the two observed wavebuoy datasets: Rio Grande (left) and Tramandai (right). The colors represent the number of occurrences in a square with 0.1 pi radians side. Regression line (thick black), its slope (s) and the correlation between the series (r) are also shown.

Table 3.1: Statistics of the time series comparison between observed and modeled sig. wave heights.

| Sig. | Rio Grande | | | | Tramandai | | | |
|---------|------------|--------|--------|--------|-----------|--------|--------|--------|
| Heights | r | s | MAE | RMAE | r | s | MAE | RMAE |
| Shelf | 0.8167 | 1.3672 | 0.3464 | 0.2041 | 0.7040 | 1.0936 | 0.2240 | 0.1818 |
| Exp. 1 | 0.8211 | 1.3022 | 0.3409 | 0.2058 | 0.6761 | 1.0375 | 0.2233 | 0.1851 |
| Exp. 2 | 0.8188 | 1.1530 | 0.3076 | 0.2024 | 0.6688 | 0.9485 | 0.2223 | 0.1917 |
| Exp. 3 | 0.7625 | 1.5955 | 0.4999 | 0.2760 | 0.6575 | 1.0746 | 0.2766 | 0.2096 |
| Exp. 4 | 0.7705 | 1.3693 | 0.4226 | 0.2399 | 0.6548 | 0.9824 | 0.2558 | 0.1995 |

Table 3.2: Statistics of the time series comparison between observed and modeled peak wave periods.

| Peak | Rio Grande | | | | Tramandai | | | |
|---------|------------|---------|--------|--------|-----------|--------|--------|--------|
| Periods | r | S | MAE | RMAE | r | S | MAE | RMAE |
| Shelf | 0.6820 | 0.7693 | 1.3631 | 0.1345 | 0.5923 | 0.5506 | 1.4434 | 0.1463 |
| Exp. 1 | 0.6483 | 0.7584 | 1.4088 | 0.1391 | 0.4992 | 0.4573 | 1.5765 | 0.1572 |
| Exp. 2 | 0.6904 | 0.7929 | 1.3325 | 0.1395 | 0.5495 | 0.5123 | 1.5021 | 0.1539 |
| Exp. 3 | 0.6399 | 0.73259 | 1.4319 | 0.1510 | 0.6234 | 0.6061 | 1.3738 | 0.1423 |
| Exp. 4 | 0.6161 | 0.7281 | 1.4974 | 0.1637 | 0.6221 | 0.6211 | 1.4011 | 0.1482 |

Table 3.3: Statistics of the time series comparison between observed and modeled peak wave directions.

| Peak | Rio Grande | | | | Tramandai | | | |
|------------|------------|--------|--------|--------|-----------|--------|--------|--------|
| Directions | r | s | MAE | RMAE | r | s | MAE | RMAE |
| Shelf | 0.4286 | 0.2638 | 27.472 | 0.1977 | 0.2520 | 0.2478 | 33.041 | 0.3503 |
| Exp. 1 | 0.4170 | 0.2790 | 27.706 | 0.1981 | 0.2643 | 0.2631 | 32.541 | 0.3458 |
| Exp. 2 | 0.4338 | 0.2959 | 26.720 | 0.1913 | 0.2661 | 0.2673 | 32.279 | 0.3440 |
| Exp. 3 | 0.4506 | 0.3264 | 25.092 | 0.1784 | 0.2409 | 0.2616 | 32.114 | 0.3375 |
| Exp. 4 | 0.4561 | 0.3292 | 25.083 | 0.1786 | 0.2393 | 0.2609 | 31.961 | 0.3372 |

Thus, the model results on the curvilinear grid are considered as in very good agreement with observations for sig. height and peak periods but presented conflicting results regarding peak directions, once the model satisfactorily reproduces SSE and secondarily the SE directions but do not correctly reproduce the ESE waves.

Finally, we show in Figures 3.15 and 3.16 the bidimensional diagrams of wave statistics, respectively for Rio Grande and Tramandai (compare with Figures 3.10 and 3.11), which were made using the model results obtained with the experiment two with wind grow (left, +w) and with the experiment four without wind grow (right, -w). Those diagrams always accentuate the possible differences by scattering the occurrences into a plane and therefore represent an invaluable help in the establishment of the experiment with the better performance.

The diagrams show how the experiments with wind grow have a better reproduction of the higher waves but worse reproduction of the lower waves, especially in Rio Grande. They also show how the density of ENE wave occurrences diminishes without wind, together with some low-period SSE waves, therefore corroborating with the possibility that these waves concealed some SE wave occurrences, which are greater in the no-wind experiments at both locations.

3.4 Concluding remarks

After briefly describe the two models utilized and present the model grids and settings, the present study evaluated the proposed validation of the basin-scale model results against orbital altimetry and the validation of the regional-scale model results against the two available wave-buoy data over the SBS, discussing the extent to which the model reproduced local reality.

Excluding localized errors, the WW3 model results of sig wave height on the Global and on the S. Atlantic grid could be considered as in very good agreement with observations, presenting remarkable similarities with observed altimetry data. The errors over the shelf break of the SBS were found to be mainly in the model underestimation of the lower waves, which shows a northward increase.

Bearing in mind the high inherent uncertainties associated with both remotely sensed data and model results, the overall low differences found are considered at least encouraging, in the sense that wave heights near the shelf break of SBS can effectively be reproduced mainly by using default WW3 simulations with NCEP wind reanalysis.

Our basin-scale results of wave periods and directions, however, were not validated against observed data and, therefore, we had no means to access the WW3 model skill in the reproduction of these wave statistics over the shelf-break of SBS. Future works shall deal with that limitation, thus enhancing our capability to validate our basin-scale wind-wave model results.

Regarding the regional-scale modeling, both sig. height and peak periods as obtained on the Shelf grid were considered as in a very good agreement with observations. Regression slopes and correlations of peak periods suggest that their misrepresentations are higher near Tramandai.

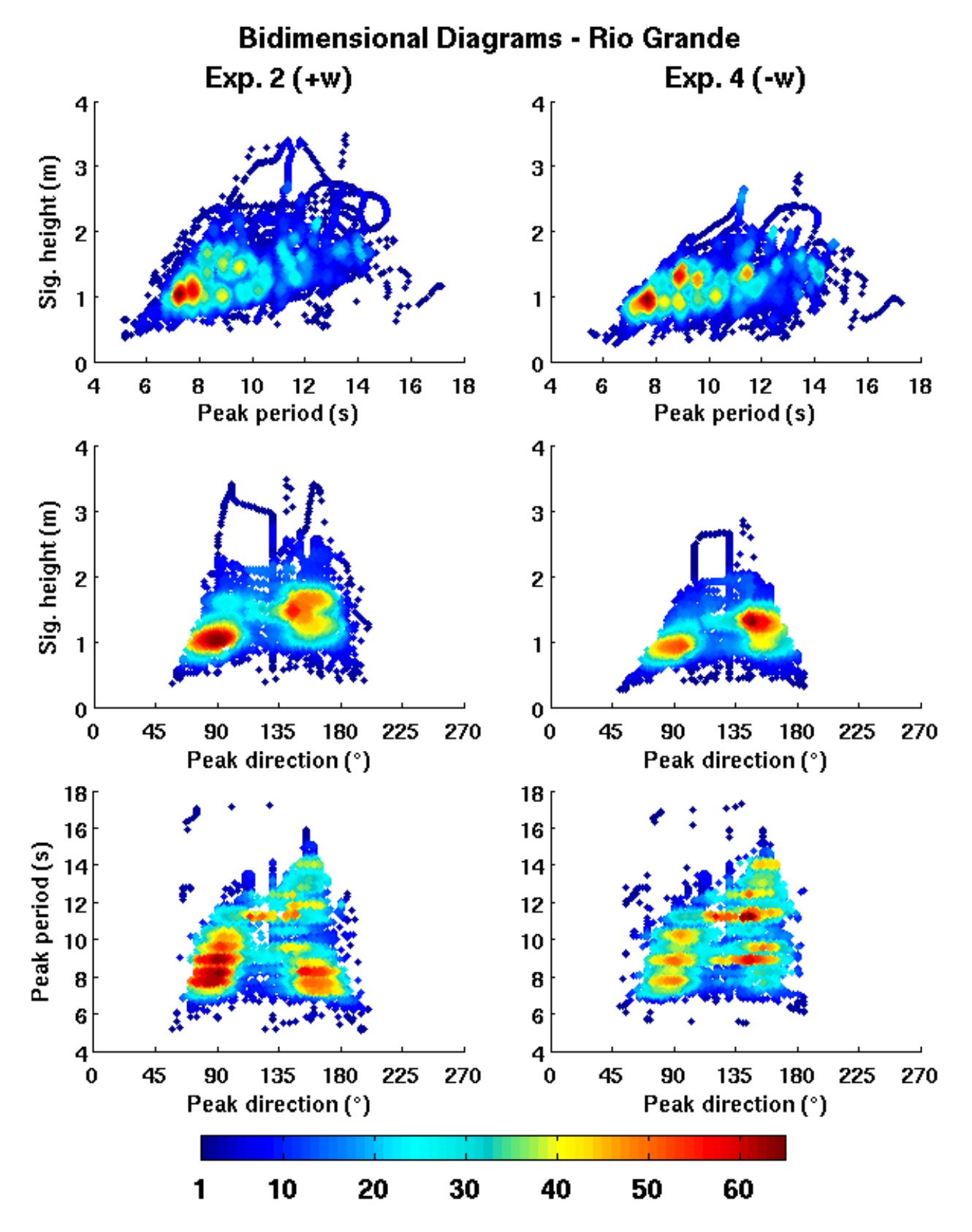


Figure 3.15: Density scatter plot showing bidimensional diagrams of wave statistics for model results at Rio Grande, as obtained in experiment two with wind grow (left, +w) and in experiment 4 without wind grow (right, -w). The colors represent the number of occurrences in a square with 0.1 m, s or pi radians side, respectively for heights, periods and directions.

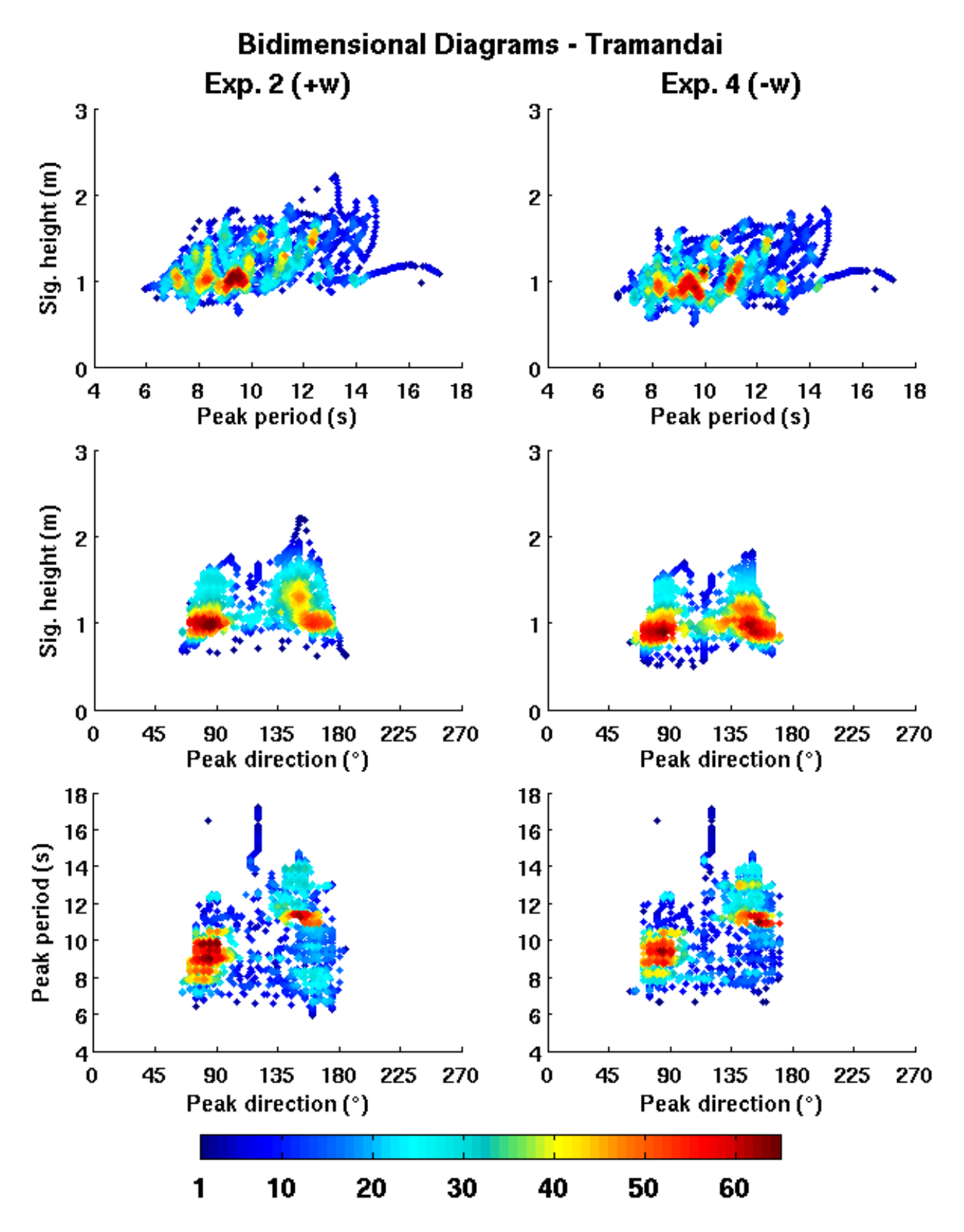


Figure 3.16: Density scatter plot showing bidimensional diagrams of wave statistics for model results at Tramandai, as obtained in experiment two with wind grow (left, +w) and in experiment 4 without wind grow (right, -w). The colors represent the number of occurrences in a square with 0.1 m, s or pi radians side, respectively for heights, periods and directions.

The peak directions, however, showed very low correlations and regression slopes in both locations, which automatically classify these results as in poor agreement with observations. Nevertheless, the S or SSE waves were closely reproduced and it was only the ESE waves that were erroneously represented as approximately E or ENE by the model.

The model results on the curvilinear Coastal grid were also considered as in very good agreement with observations for sig. height and peak periods but presented the same conflicting results regarding peak directions, once this high-resolution grid satisfactorily reproduces SSE and even secondarily the SE directions but also do not correctly reproduce the ESE wave.

We believe that these E or ENE waves were already incorrectly produced by the basin-scale model WW3, which then transferred this error downwards through the boundaries conditions. Future experiments shall make sensibility tests to verify the origin of this error in the northern part of SBS and possibly propose a solution.

The wave statistics of model results on the curvilinear grid were proven to be effectively influenced by local wind, which improved higher waves performance but impaired the model performance in terms of lower waves, peak periods and peak directions. The fact that the inclusion of wind grow almost doubles the computational effort without consistently improve performance give support to the possible use of the no-wind option in future experiments with this grid, in which case much care shall be taken with the validation of sig. wave heights.

Increased spatial resolution certainly played a role and cannot be discarded, once it shows overall better statistics and greater variability of results, but it was the lowering of bottom friction that represented the major improvement in the curvilinear grid simulations. Most probably because of the very low declivity of the SBS and the complete smoothness of its very fine sandy bottom, the model configuration with a smaller friction coefficient yielded by far the best performances within the curvilinear grid experiments, attesting that smaller bottom friction might indeed be a very good calibration parameter in future experiments with SWAN wave model in the region.

Chapter 4

Wave variability in time and space

4.1 Large-scale wave patterns

The first step into a better definition of the wave conditions over the SBS is to present the maps of the long-term mean (1990-2012) sig. wave height and peak wave period as obtained in our WW3 model results (Figure 4.1). It is possible to see both the sheltering effect of South America on the waves generated by the westerlies and the northward decrease of wave heights as previously discussed in chapter 3.

The same continental sheltering is responsible for the large area of lower mean peak period found at the southwestern South Atlantic, which defines this region as a generation area dominated by local waves with minor incoming remote waves (or swell). Further north and centered at about 30 °S it is also possible to see in light orange (8 s) a lower mean peak period area made by the ENE/E waves generated by the winds of the South Atlantic High pressure cell (SAH).

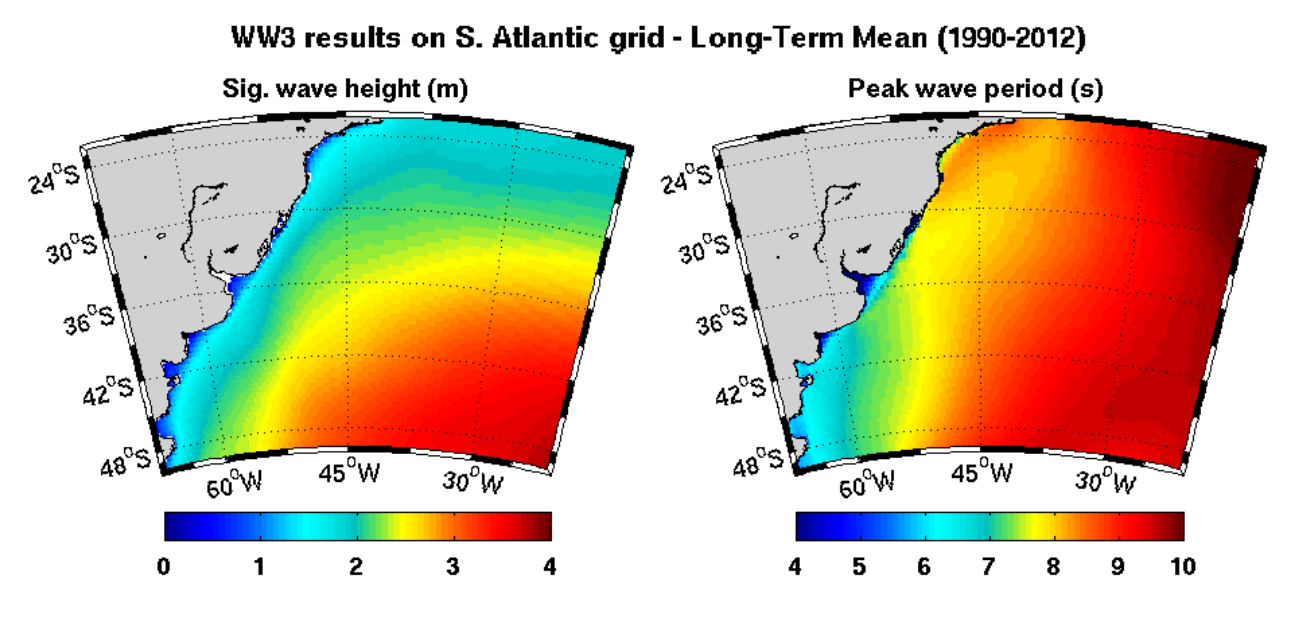


Figure 4.1: Long-term mean (1990-2012) of sig. wave height (left) and peak wave period (right) as obtained with our WW3 model results on the S. Atlantic grid.

These results allow us to define the SBS positioning exactly in the encounter between the influence of the westerlies and cyclones and the influence of the SAH, at least regarding windwaves generation and in present day atmospheric conditions. Altogether, it also corroborates with the early statement that the SBS is essentially bimodal in directions.

It is worth to mention that over the SBS and excluding shallow water, the long-term mean sig. wave height attains approximately between 1.5 m and 2 m, which can be considered, at most, a moderate energy condition. However, as it was previously discussed in chapter 2, typical high-energy wave occurrences are not due to the mean atmospheric circulation but instead due to the succession of synoptic-scale oscillations of high and low sea-level pressure cells moving eastward across South America that ultimately results in alternate surface winds over the ocean.

As a rule, instant maps of wave statistics are extremely messy, being most of the time a superposition of diverse wave patterns which makes it difficult to carry further subjective interpretation. Nevertheless, out of 23 years of six-hourly simulations we were able to identify and pinch out some isolated examples that might help the general characterization of the SBS wave climate.

We start in Figures 4.2 to 4.4 showing examples of wave patterns induced by the presence of extratropical cyclones around the three clearly distinguishable regions of cyclogenesis maxima over the western South Atlantic. From north to south, the first is located near the northern extreme of the SBS (27 °S), the second is off Uruguay and over the SBS (35 °S) and the third is off Argentina (48 °S).

In Figure 4.2 we present the high waves generated by the cyclogenesis near 27 °S, which were certainly found mostly during summer and therefore most probably share the cyclone's relation with the atmospheric subtropical convergence zone. These chosen events occurred on 17/12/2008 (top) and 04/01/2009 (bottom) causing E/ESE waves up to 5.5 m height as in Figure 4.2 (bottom-left) and can be strong enough to even cause opposite wave directions as in Figure 4.2 (bottom-right). After genesis these cyclones usually move southeastward, then possibly generating high waves from SE over the SBS.

The cyclones on 27 °S have by far the lower vorticity of the three. In Figure 4.3 we present two examples of high waves generated by the cyclogenesis near 35 °S, which are centered in wintertime but also exhibit enhanced vorticities during autumn and spring due to intensification of atmospheric thermal gradients.

The events of 18/04/1999 (top) and 03/09/2006 (bottom) are isolated examples when waves reached up to 8 m sig. height and even formed a perfect ring of high waves, leaving no doubt on the importance of such phenomena for the SBS. The occurrence of high SE waves is also made clear at the southern portion of the cyclones, at a longer distance from the coast than the S/SW waves.

In Figure 4.4 we show then examples of wave patterns generated by the cyclogenesis centered at 48 °S, which occur all over the year but more frequently during summer. The events of 19/02/1995 (top) and 24/06/2007 (bottom) also show areas with more than 8 m of sig. height that were originated at 48 °S but later did spread out for the entire western South Atlantic.

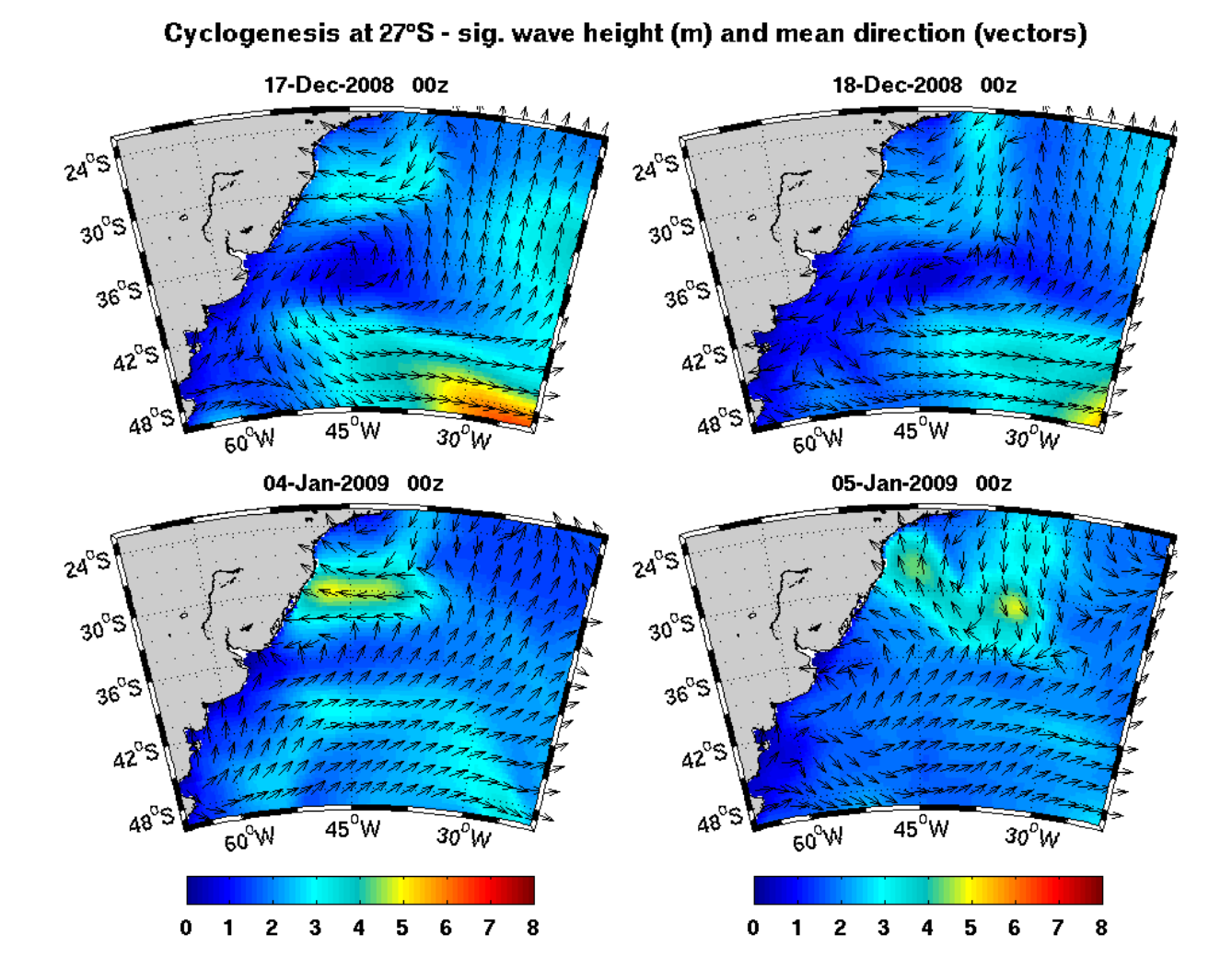


Figure 4.2: Examples of wave patterns generated by the cyclogenesis centered at 27 °S. Sig. wave height (m) and mean wave direction (adimensional vectors) for the events of 17/12/2008 (top) and 04/01/2009 (bottom) as obtained with our WW3 model results on the S. Atlantic grid.

Either generated by the cyclones of 35 °S (Figure 4.3, bottom-right) or by the cyclones of 48 °S (Figure 4.4, bottom-right), these northeastward spreadings of the waves are, in fact, a very recurrent situation over the western South Atlantic and do occur even in the absence of an identifiable cyclone, driven then by ordinary low pressure systems.

By the time when the anticyclonic high pressure cell reaches the ocean, the wind blows back to the continent and possibly generates E/SE waves. Later, if there is enough time between two frontal systems, the ENE waves generated by the SAH cell establish and reinforce until the next event, usually marked by the N/NW pre-frontal waves spreading out from near SBS away into the Southern Ocean.

In Figure 4.5 (top) we show two isolated examples of post-frontal SE waves reaching the SBS on 31/12/2010 (top-left) and reaching the crescent moon shaped Southeastern Brazilian Shelf (SEBS) northward from SBS on 26/12/2001 (top-right). It becomes clear that there is a relationship between the latitude subject to post-frontal SE waves and the high pressure cell positioning, once it can only blow SE waves over the SBS when is located south from 40 °S. Worthwhile to emphasize that the arrival of such SE waves to the coast after the S/SW condition

shall not be mistaken with the frontal SE waves which are generated by the cyclones and also arrive after the S/SW condition.

In Figure 4.5 (bottom) it is presented the event started on 14/10/1999 to show the change from ENE waves of the post-frontal condition (bottom-left) to the pre-frontal N/NW waves (bottom-right) that can reach values up to 5 m, but is directed away from the SBS.

Finally, we present the evolution of high waves from ENE and from E/ESE that sometimes last for several days reaching 3 to 4 m height. The event between 02 and 05/10/2006 (Figure 4.6) shows the high waves from ENE that turns into NE waves near Uruguay. At least at the surroundings of the SBS, the orientation of these waves resembles very much the mean atmospheric near surface circulation (Figure 2.6).

In Figure 4.7, the event between 07 and 10/03/2010 shows extreme waves from E attaining up to 6 m sig. height just in front of the SBS in a post-frontal configuration. Although they are not usually that high, yet these E waves are used as an example that under certain circumstances the meridional atmospheric pressure gradients might indeed become important, even in the absence of a cyclone.

Cyclogenesis at 35°S - sig. wave height (m) and mean direction (vectors)

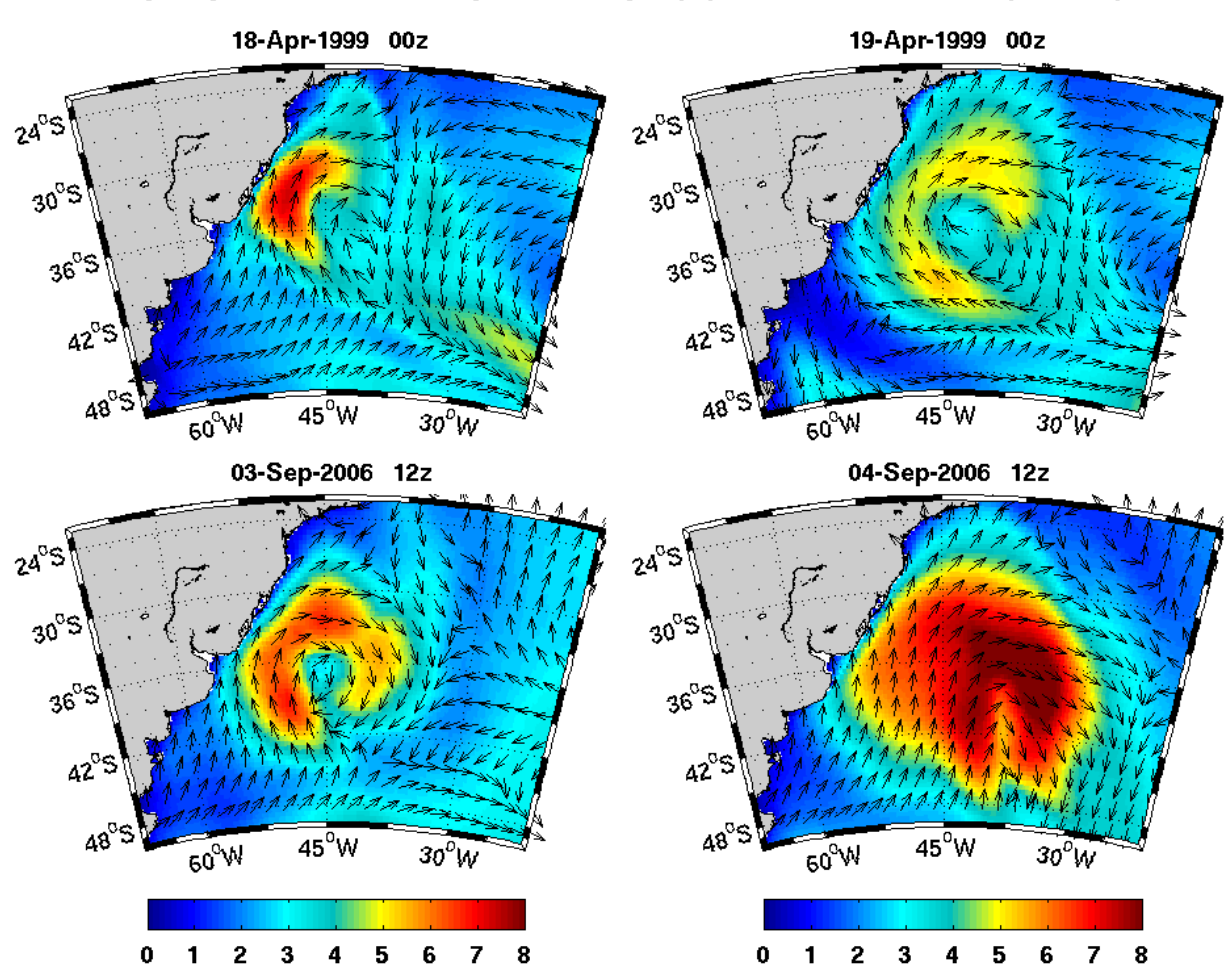


Figure 4.3: Examples of wave patterns generated by the cyclogenesis centered at 35 °S. Sig. wave height (m) and mean wave direction (adimensional vectors) for the events of 18/04/1999 (top) and 03/09/2006 (bottom) as obtained with our WW3 model results on the S. Atlantic grid.

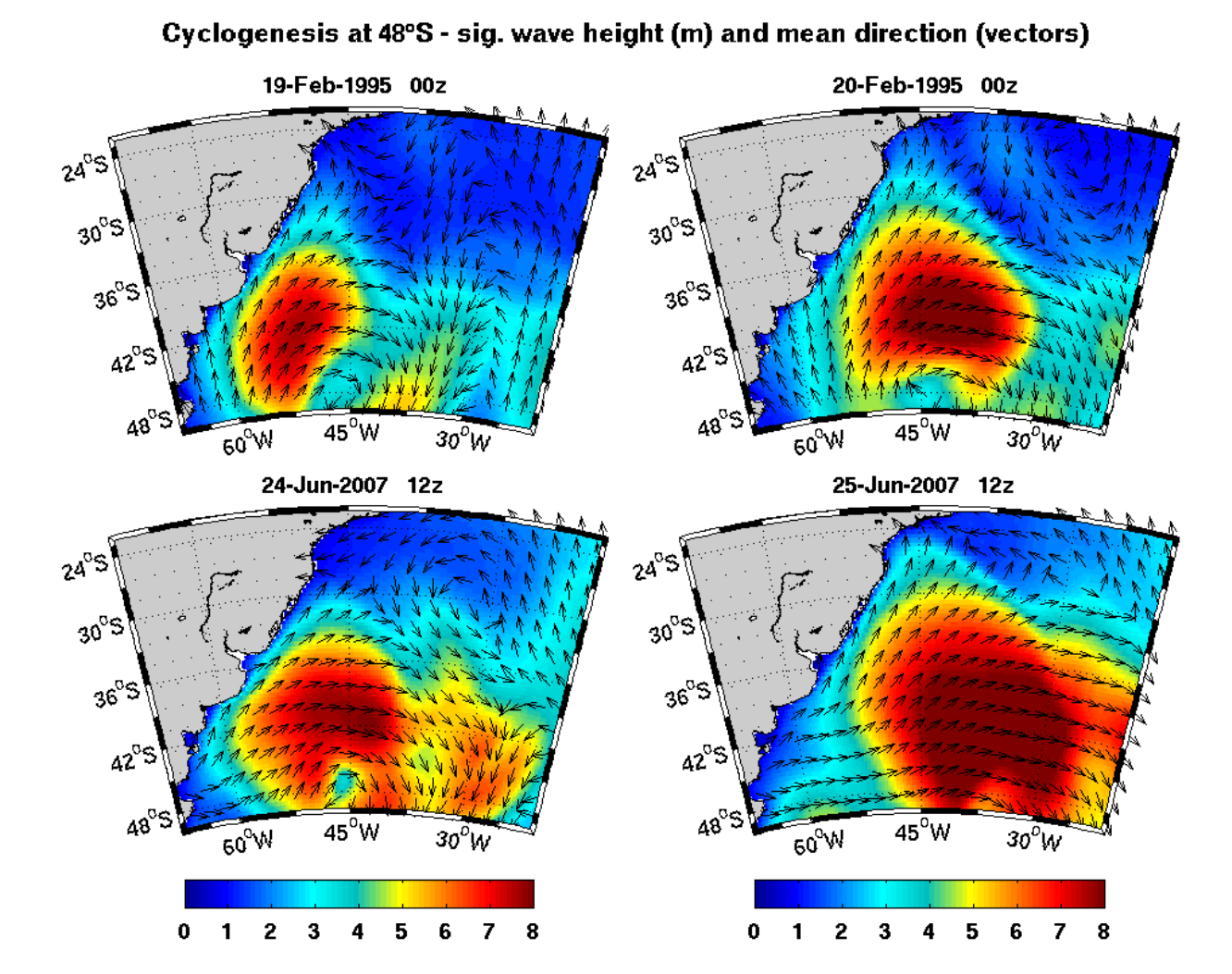


Figure 4.4: Examples of wave patterns generated by the cyclogenesis centered at 48 °S. Sig. wave height (m) and mean wave direction (adimensional vectors) for the events of 19/02/1995 (top) and 24/06/2007 (bottom) as obtained with our WW3 model results on the S. Atlantic grid.

As presented in chapter 3, our results do overestimate the occurrences of these ENE waves in impairment of the E/ESE waves. In Figures 4.6 and 4.7 we can see that the difference between both wave patterns lies in the general configuration of the waves associated to the mobile high pressure cell, whose northern portion may or may not present a stronger E wave component.

It is imperative to call for special attention to the existence of a vorticity around 25 °S in Figure 4.7 (bottom), turning waves clockwise. The low sea level pressure responsible for this is most probably the very same responsible for induce summer cyclogenesis at 27 °S and the similarities between the E wave patterns of Figures 4.2 and 4.7 are far from being just a coincidence. When this coastal low do occur, the otherwise ENE waves come from E or ESE in closer agreement with the observed wave-buoy data. When it does not, the ENE waves persist longer and in clear disagreement with observations.

The location of this low early suggests the influence of the atmospheric subtropical convergence zone, but it is important to remind that it is also influenced by the 1000 m relief of eastern South America that near the coast accompany the entire crescent moon shaped SEBS, thus creating a sheltering effect from the low-level N/NW mean winds.

Post-Frontal SE and Pre-Frontal N/NW - sig. wave height (m) and mean direction (vectors)

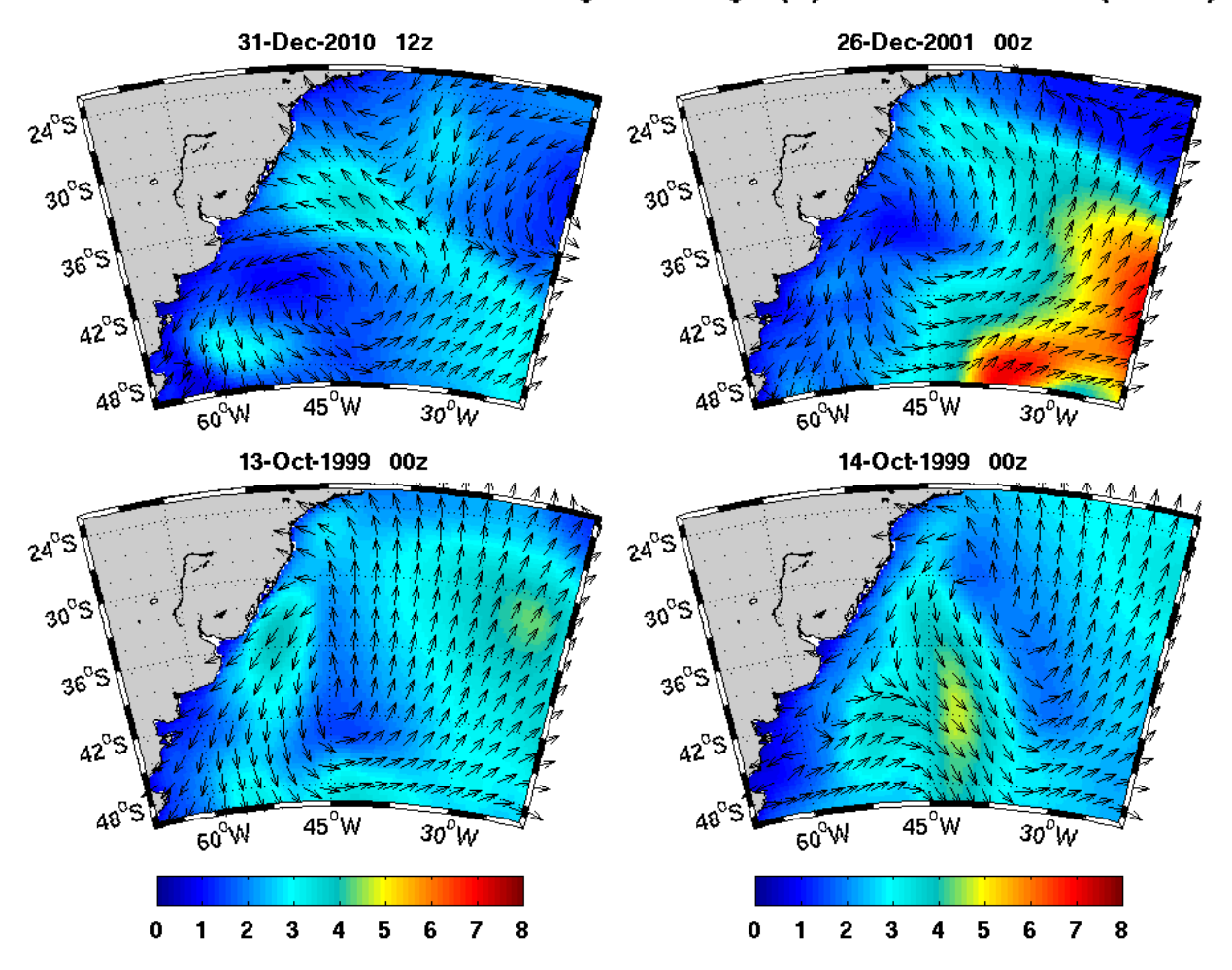


Figure 4.5: Two examples of post-frontal SE waves (top) and one example of pre-frontal change from ENE to N/NW waves (bottom). Sig. wave height (m) and mean wave direction (adimensional vectors) for the events of 31/12/2010 and 26/12/2001 (top) and 14/10/1999 (bottom) as obtained with our WW3 model results on the S. Atlantic grid.

Due to this large and abrupt topographic change, when reaching the ocean the lower atmosphere mean circulation is then subject to a significant pressure drop. In addition, it is also bottom heated by the warm Brazil Current flowing near shelf-break, thus enhancing this coastal low sea level pressure. Furthermore, the N/NE surface winds coming aloft the ocean from tropical Brazil are also guided offshore by the abrupt change of coastline orientation at Cape Frio, Rio de Janeiro (22 °S), only turning clockwise southward of this coastal low (e.g. Figure 2.3 (DJF) and Figure 2.6).

The continental relief and this coastal low pressure at SEBS thus act together by blocking the northeastward advance of the mobile high pressure cell along the coast and deviating it to the east into the ocean (Figure 4.7, top-right). The coastal low itself, which is a somewhat persistent feature enhanced during summer, then finally acts separating the mobile high from the mean SAH and also helping in the establishment of the meridional pressure gradients that are strong enough to generate these E waves that reach the SBS (Figure 4.7, bottom-left).

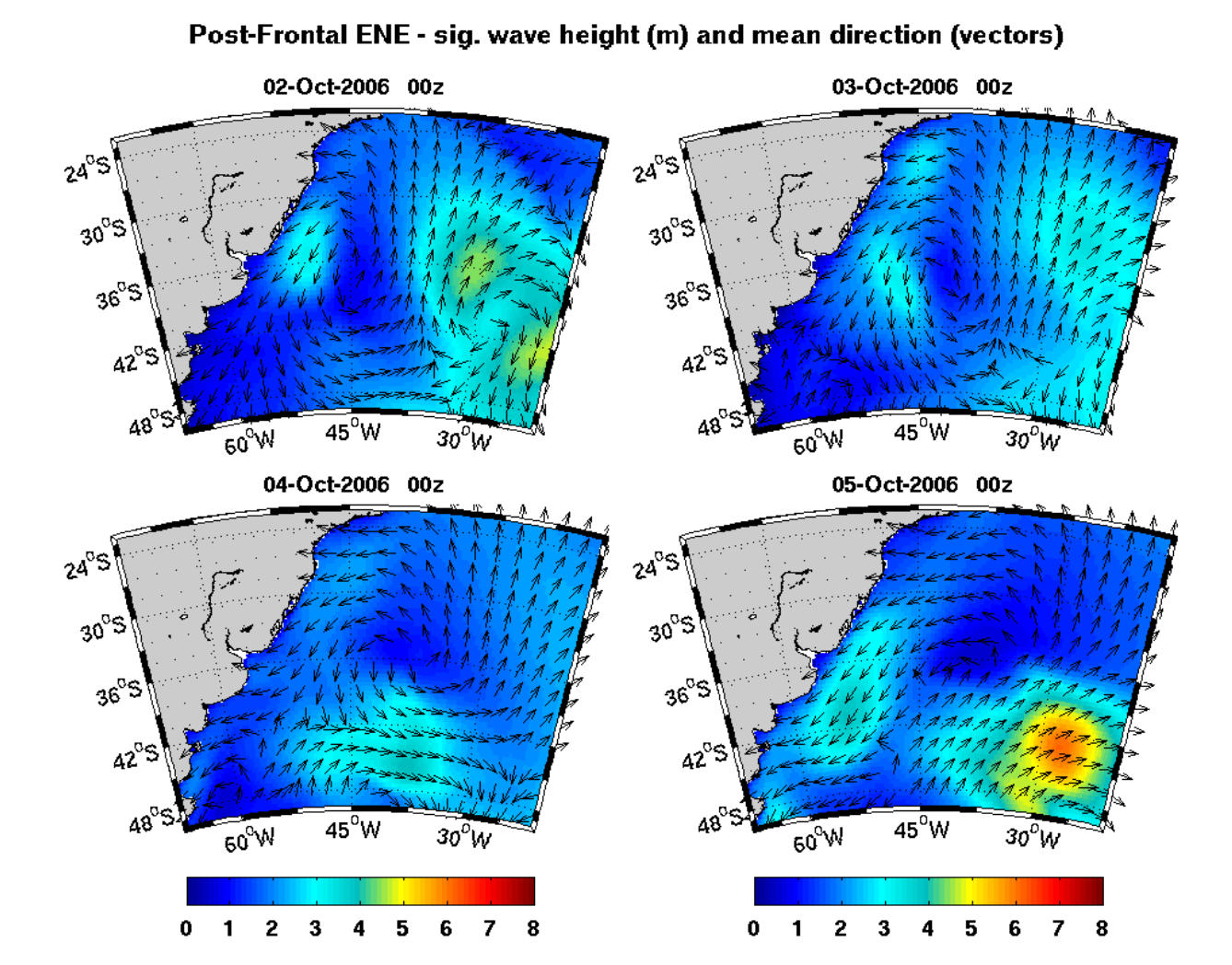


Figure 4.6: Example of ENE wave patterns generated by the eastward moving high pressure cell. Sig. wave height (m) and mean wave direction (adimensional vectors) for the event between 02 and 05/10/2006 as obtained with our WW3 model results on the S. Atlantic grid.

The fact is that, if observations are correct and the SBS is not under extensive ENE wave action, then this coastal low pressure acting between 25 and 27 °S over the SEBS is certainly more common and possibly also stronger than it is represented in the NCEP Reanalysis dataset. Besides, it proves to be an important factor in the merging between the moving high cell and the mean SAH and, as long as we are discussing about a relatively regional scale feature, its underrepresentation on 1.9° grid resolution reanalysis is not entirely unexpected.

By all means, the bottom line is that the wave patterns over the SBS present themselves as very sensitive to the relative positioning of the eastward moving high and low pressure systems as well as to the presence of the SEBS coastal low pressure. Hence, any possible change on this delicate system, either at present or at geological timescale, might drive a huge consequence on the SBS wave climate.

In order to objectively quantify the variability found in our wave model results we made an attempt to estimate the coupled covariance of sig. wave height and peak wave period by means of the use of the singular value decomposition (SVD), following Bjornsson and Venegas (1997).

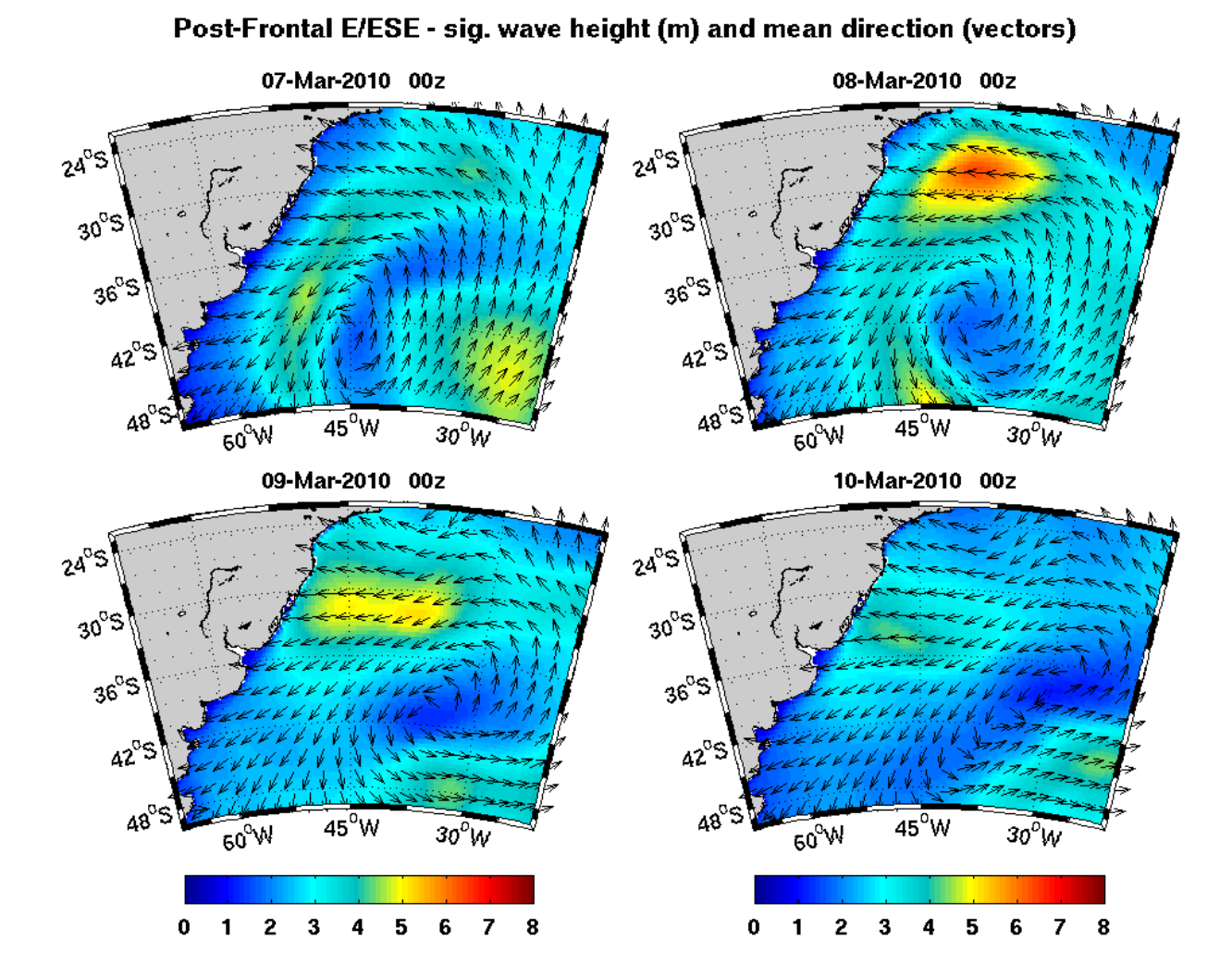


Figure 4.7: Example of E/ESE waves patterns generated by the eastward moving high pressure cell. Sig. wave height (m) and mean wave direction (adimensional vectors) for the event between 07 and 10/03/2010 as obtained with our WW3 model results on the S. Atlantic grid.

This method is used to calculate the temporal cross-covariance matrix yielding two spatially orthogonal sets of singular vectors that form a spatial pattern for each variable and also a set of singular values associated with each pattern. Each pair of these spatial patterns describes a fraction of the square covariance between the two variables and the expansion coefficients obtained from the singular values describe how each one of these modes of variability oscillates in time.

In Figure 4.8 we present the long-term SVD of daily mean sig. height and peak period as obtained with our WW3 model results on the S. Atlantic grid between 1990 and 2012. First three modes are shown with the respective fraction of explanation (%) and the correlation between expansion coefficients (r).

First mode attained as high as 76.77 % but with low correlation between the coefficients (r=0.164) and with a covariance pattern that totally fits the mean fields previously presented in Figure 4.1. Rather than explaining such a large fraction of the data, this mode is actually showing us that most of the data is poorly explained. Second mode attained more 15.27 % of explanation but showed even worse correlation of coefficients (r=0.083). Up to there, we were

not optimistic with the use of the method.

Aware of the close relation between sig. wave heights and peak wave periods and that this relation should somehow appear with the use of the SVD method of cross-covariance, we tried then to filter all the data of both variables in time. Cut-frequencies corresponding to 20 days, 90 days and 2 years were used in low-pass filters without success, once correlations hardly exceeded 0.2.

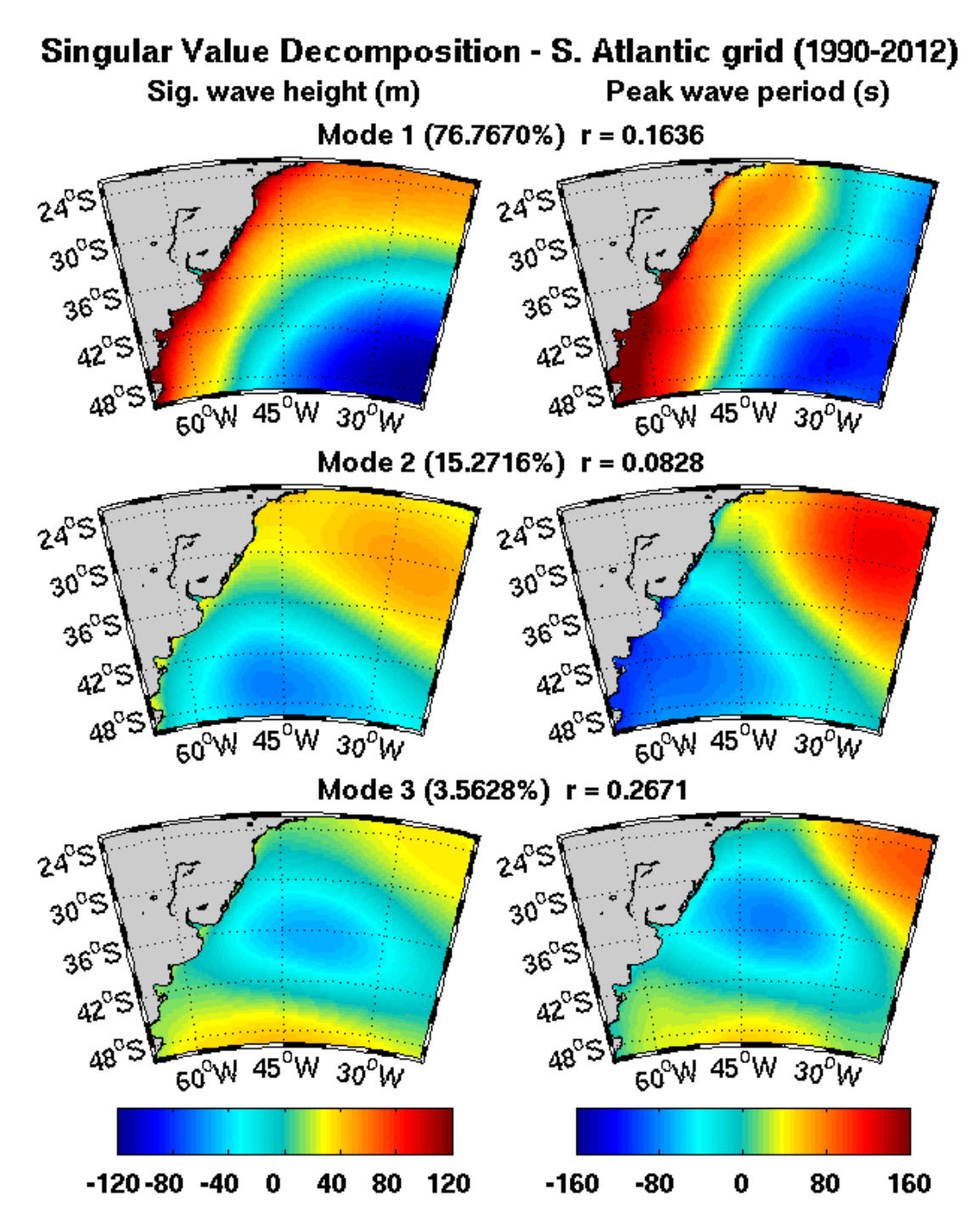


Figure 4.8: Long-term SVD of daily mean sig. height and peak period as obtained with our WW3 model results on the S. Atlantic grid between 1990 and 2012. Modes 1 to 3 are shown with the respective fraction of explanation (%) and the correlation between expansion coefficients (r).

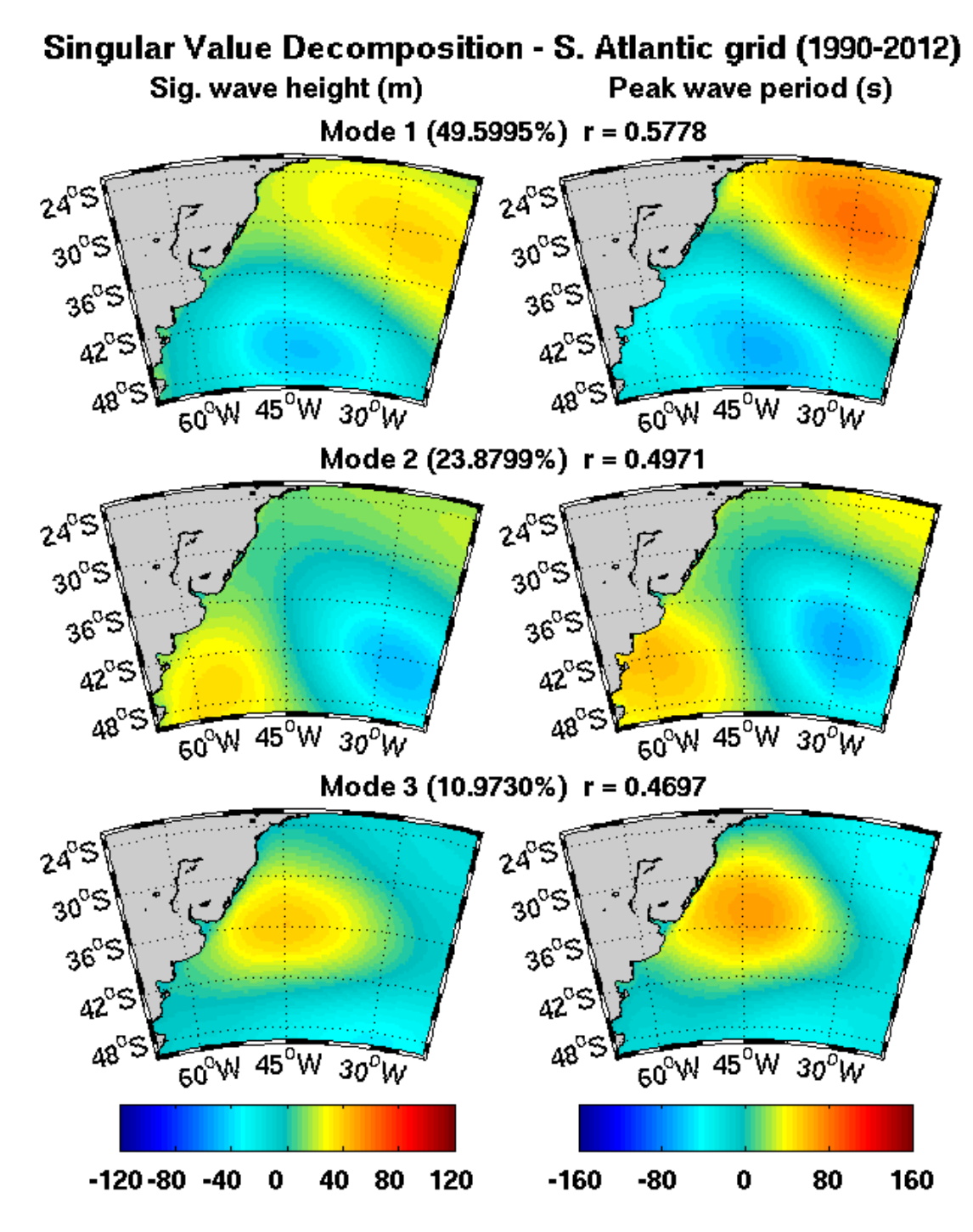


Figure 4.9: Long-term SVD of daily mean sig. height and peak period as obtained with our WW3 model results on the S. Atlantic grid between 1990 and 2012, after high-pass filtering with 20 days cutting frequency. Modes 1 to 3 are shown with the respective fraction of explanation (%) and the correlation between expansion coefficients (r).

The same frequencies were then used in high-pass filters, but this time the highest frequency showed up with meaningful results. The resultant patterns were then interpreted as having positive coupled covariance where higher period waves are formed and negative coupled covariance where lower period waves are formed.

In Figures 4.9 and 4.10 we show the modes 1 to 3 and 4 to 6, respectively, from the long-term SVD of daily mean sig. height and peak period obtained after high-pass filtering the data with 20 days cutting frequency.

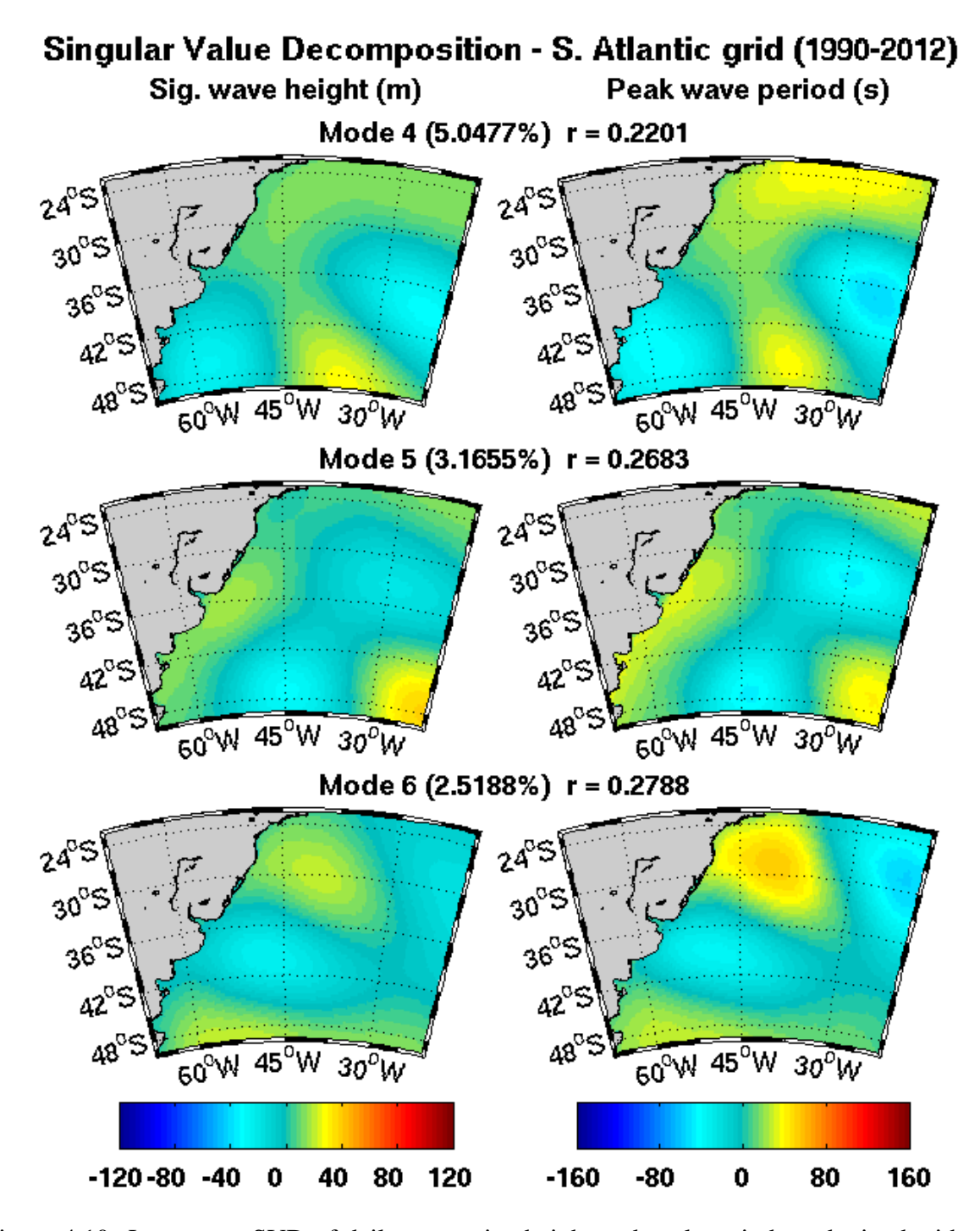


Figure 4.10: Long-term SVD of daily mean sig. height and peak period as obtained with our WW3 model results on the S. Atlantic grid between 1990 and 2012, after high-pass filtering with 20 days cutting frequency. Modes 4 to 6 are shown with the respective fraction of explanation (%) and the correlation between expansion coefficients (r).

Now, the first mode explains nearly half the covariance (49.6 %) with very better correlation (r=0.578) and shows a bimodal spatial pattern that resembles the general northeastward spreading of the waves with growing wave periods that occurs during almost every synoptic-scale event. Therefore, this ordinary condition must be in fact considered as the principal mode of variability of the western South Atlantic wave climate and shall not be neglected in future experiments.

Second mode now explains 23.88 % of the covariance with some correlation (r=0.497) and

presents a bimodal spatial pattern that shows positive values to the cyclogenesis region at 48 °S and negative values to the generation under the westerlies more to the east. Unimodal third mode with 10.97 % of explanation and also some correlation (r=0.47) shows the spatial pattern of the cyclogenesis region at 35 °S. The next three modes presented lower correlations but the spatial patterns seem to represent the pre-frontal, possibly added to the cyclogenesis at 27 °S (mode 4), and the post-frontals ENE (mode 5) and SE (mode 6) waves.

Although this SVD method was able to provide us an objective way of quantifying the coupled covariance of sig. wave height and peak wave period and thereby helped to define the above mentioned spatial wave patterns, it does so only in the timescale of wind-wave generation in which the relation between wave height and period still holds and, therefore, was not of much help to evaluate the interannual variability of the SBS wave climate.

4.2 SBS Offshore wave conditions

It is way beyond the aim of the present study to describe the SBS geological evolution or even to classify any particular shelf feature, but the first order differences of declivity in the cross-shelf and along-shelf directions are indeed expected to influence the general pattern of wave energy distribution over the shelf.

In this sense, it is utterly necessary to distinguish between the larger mid-shelf in the southern part of SBS and the narrower mid-shelf found northward from 32 °S, as can be inferred in Figure 4.11 by the distance between the 60 m isobath and the shoreline. For instance, please notice the much larger distance in front of Polonio Cape than in front of Santa Marta Cape, at the southern and northern extremities of SBS, respectively.

The outer-shelf declivities, made clear by the distance between the 100 m and 200 m isobaths in Figure 4.11, are very much greater at south in such a way that shelf-break (200 m) remains at a rather constant distance from the shoreline for the entire SBS. Consequently, the SBS physiography present opposite patterns with a low declivity mid-shelf and a high declivity outer-shelf on its southern part and with the contrary being found northward from 32 °S.

For the spectra analysis of the SBS offshore wave climate, as obtained with our SWAN experiments on the shelf grid, we then chose eight points from north to south over the 60 m and 200 m isobaths (Figure 4.11, red asterisks and squares). In Figures 4.12 and 4.13 we then show the long-term mean (1990-2012) power spectra for these eight points at shelf-break (200 m) and mid-shelf (60 m), respectively.

Both figures present similar bimodal spectra shapes, which therefore defines the offshore climatological wave power spectra of the SBS. There is a predominance of the SSE/SW waves generated by the frontal systems and cyclones with power peak between S/SSW. The lower power peak composed of ENE/E waves are generated by the post-frontal winds.

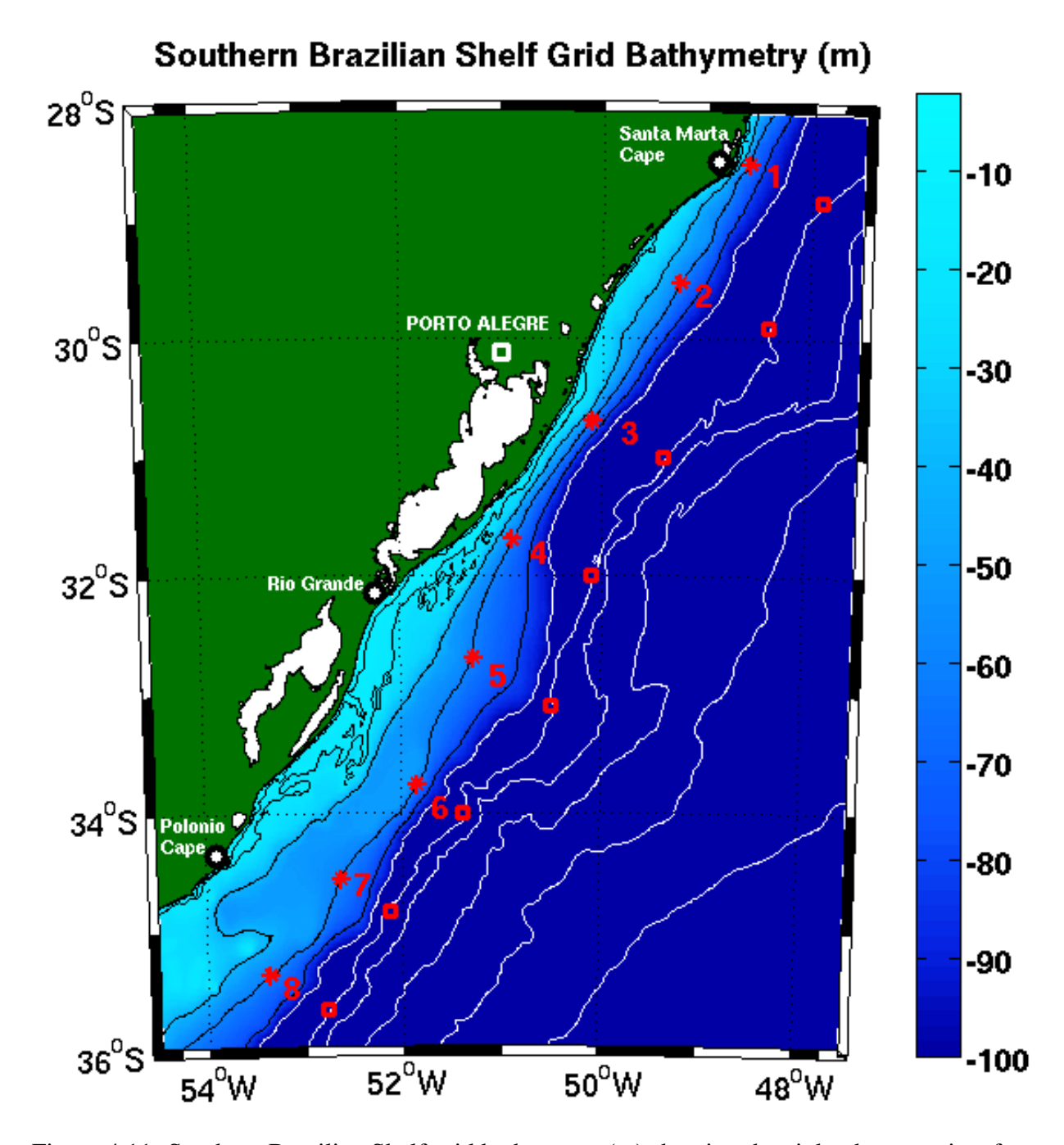


Figure 4.11: Southern Brazilian Shelf grid bathymetry (m) showing the eight chosen points for offshore wave power spectra analysis along the 60 m isobath (red asterisks) and 200 m isobath (red squares). Black isolines are for 12, 20, 40, 60 and 80 m depth and white isolines are for 100, 200, 1000, 2000, 3000 and 4000 m depth.

The intensities are reduced and the overall shapes are smoothed in the mid-shelf power spectra, but S/SSW waves still diminishes northward and ENE/E waves secondarily diminish southward. It is also noticeable a W component remaining at mid-shelf on the southern points 6 to 8.

These results in fact corroborate with the previous statement that SBS is located in the encounter between the influence of the westerlies and cyclones and the influence of the SAH, at least regarding wind-wave generation and in present day atmospheric conditions.

Long-Term Mean Power Spectrum at 200m (m²/Hz)

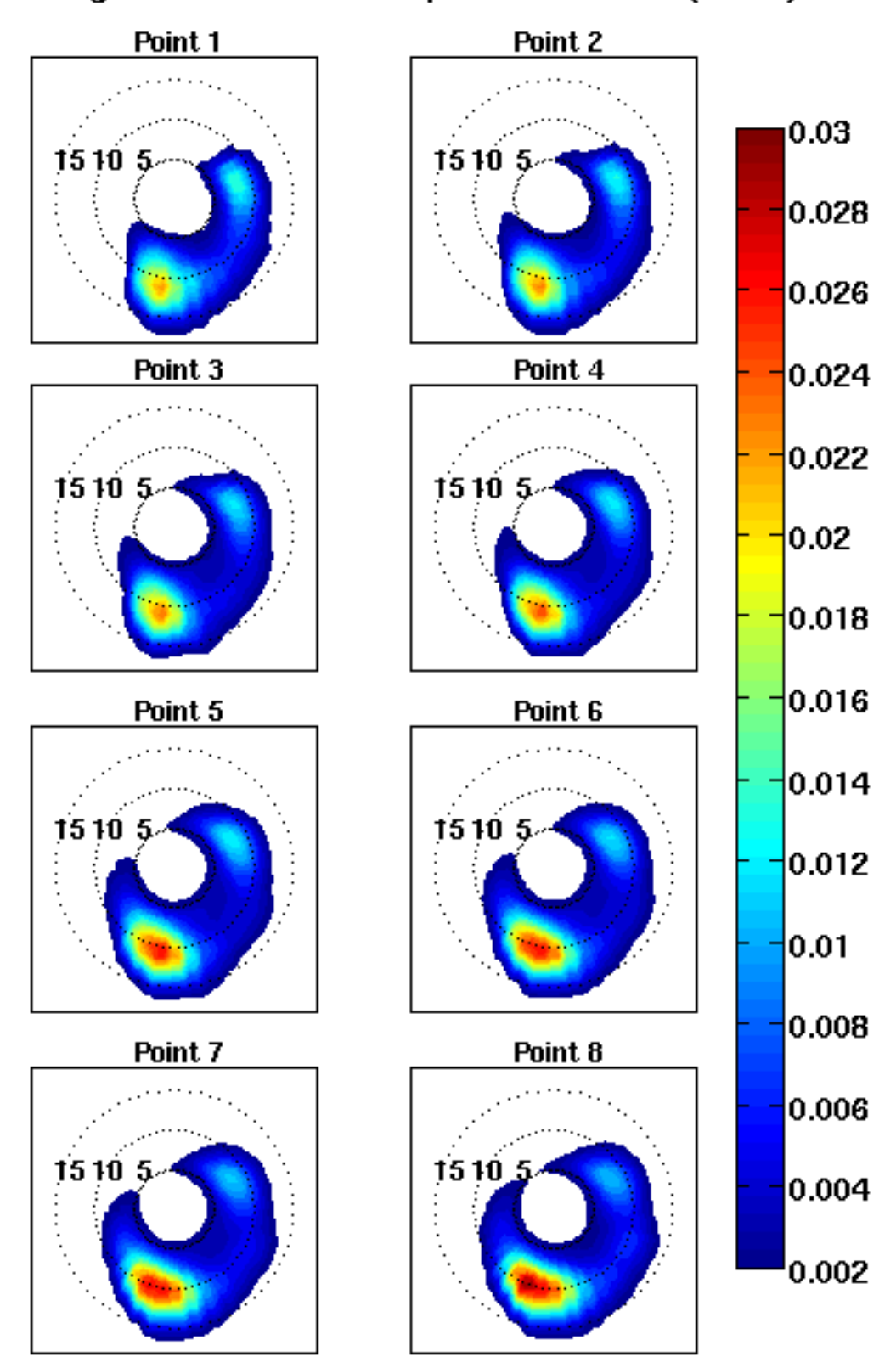


Figure 4.12: Long-term (1990-2012) mean wave power spectrum (m²/Hz) as obtained with our SWAN experiments on the shelf grid, for the eight points selected at shelf-break (200 m).

Long-Term Mean Power Spectrum at 60m (m²/Hz)

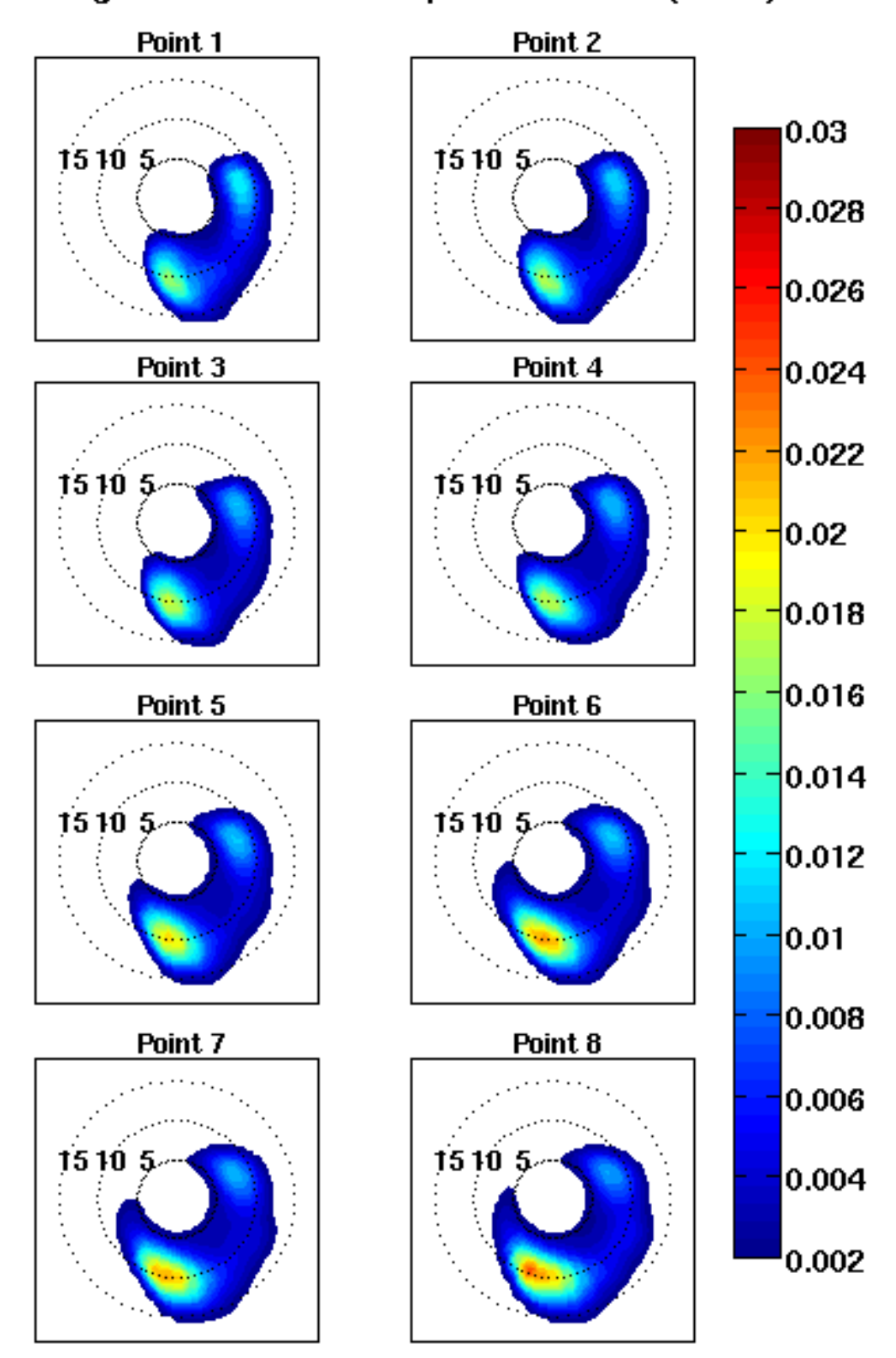


Figure 4.13: Long-term (1990-2012) mean wave power spectrum (m²/Hz) as obtained with our SWAN experiments on the shelf grid, for the eight points selected at mid-shelf (60 m).



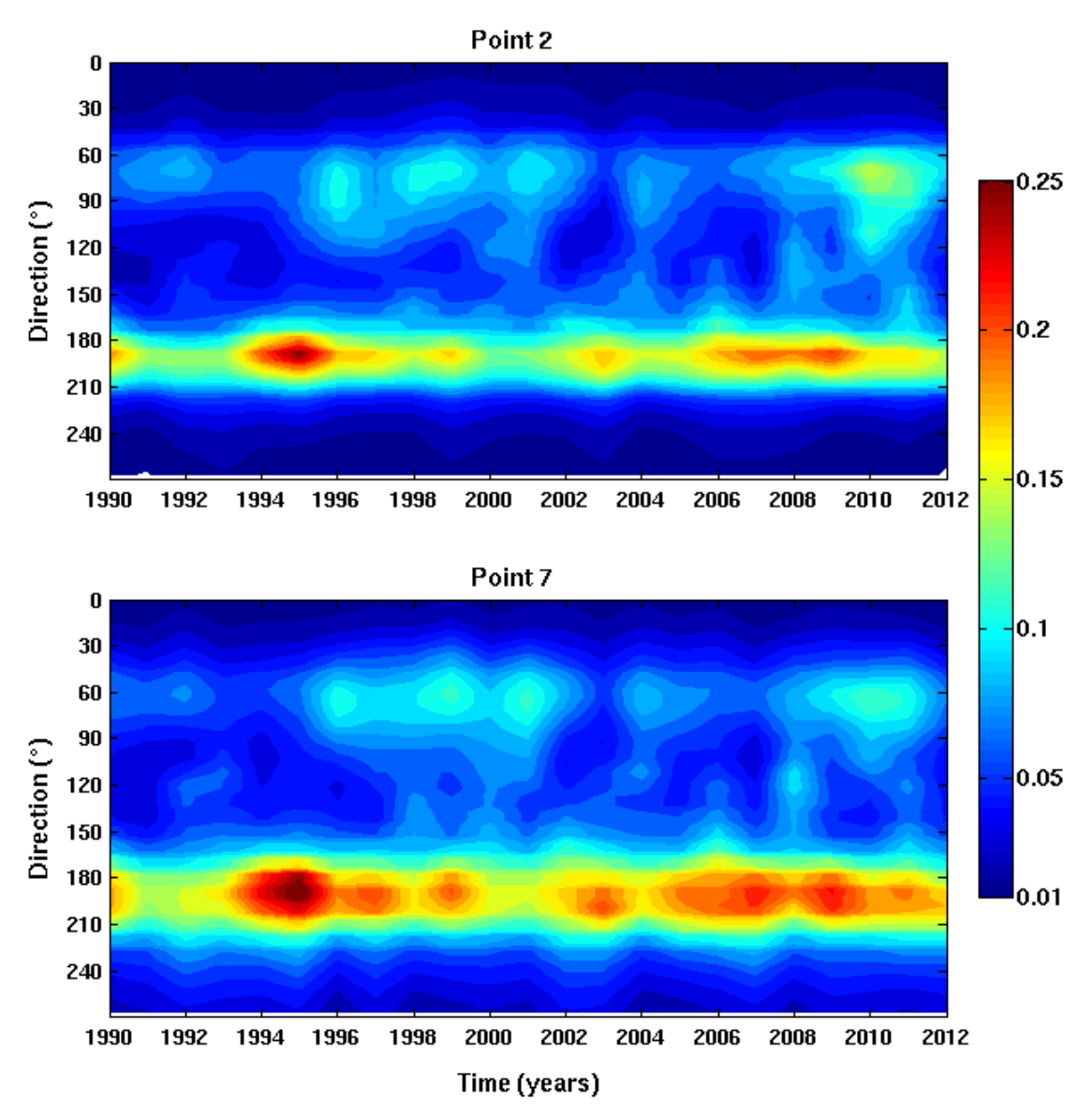


Figure 4.14: Long-term distribution (1990-2012) of the annual mean power spectrum (m²/Hz) as obtained with our SWAN experiments on the shelf grid, integrated over frequencies, for the points 2 (top) and 7 (bottom) at shelf-break (200 m).

In Figure 4.14 we present the long-term distribution of the annual mean power spectrum at the shelf-break, integrated over frequencies, for points 2 and 7 as representatives for the northern and southern parts of the SBS. Similarly, we present in Figure 4.15 the spectra at mid-shelf points, which despite the general lower intensities when compared with shelf-break spectra also show the same large interannual changes.

Both figures show a distinctive pattern between 1996 and 2001 and again between 2008 and 2011, when there is a clear rise in ENE/E wave power and secondarily in the ESE wave power. The S/SSW waves by its turn, present power maxima just before those risings, between 1994 and 1995 and between 2006 and 2009, with power minima between 1991 and 1992 and between 2000 and 2001.



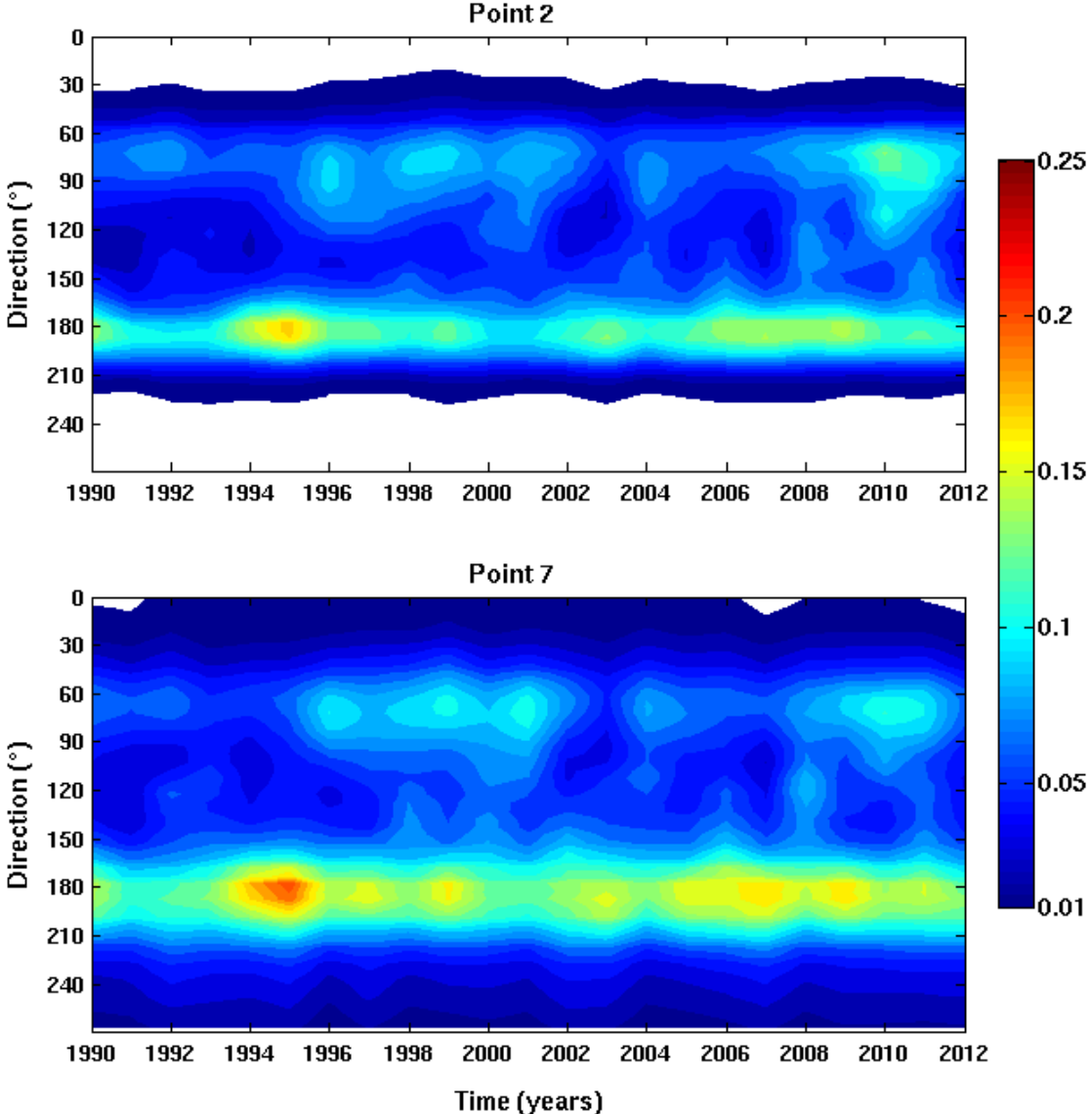


Figure 4.15: Long-term distribution (1990-2012) of the annual mean power spectrum (m²/Hz) as obtained with our SWAN experiments on the shelf grid, integrated over frequencies, for the points 2 (top) and 7 (bottom) at mid-shelf (60 m).

The coincidence between the ENE/E wave power rising periods and the known peaks of La Ninã lead us to the comparison presented in Figure 4.16. We took the shelf-break and mid-shelf wave power spectra integrated over frequencies only between 30° and 120° and plotted against the Southern Oscillation (SO) index for the entire period of the experiments. The wave power series obtained this way were also demeaned and the 13 months running mean SO index was rescaled to fit the standard deviation of the wave power.

These results show how the differences in wave power between the shelf-break and midshelf vanish after the removal of the respective means, which therefore suggests that the mean field holds the information of almost the entire outer-shelf wave power transformations.

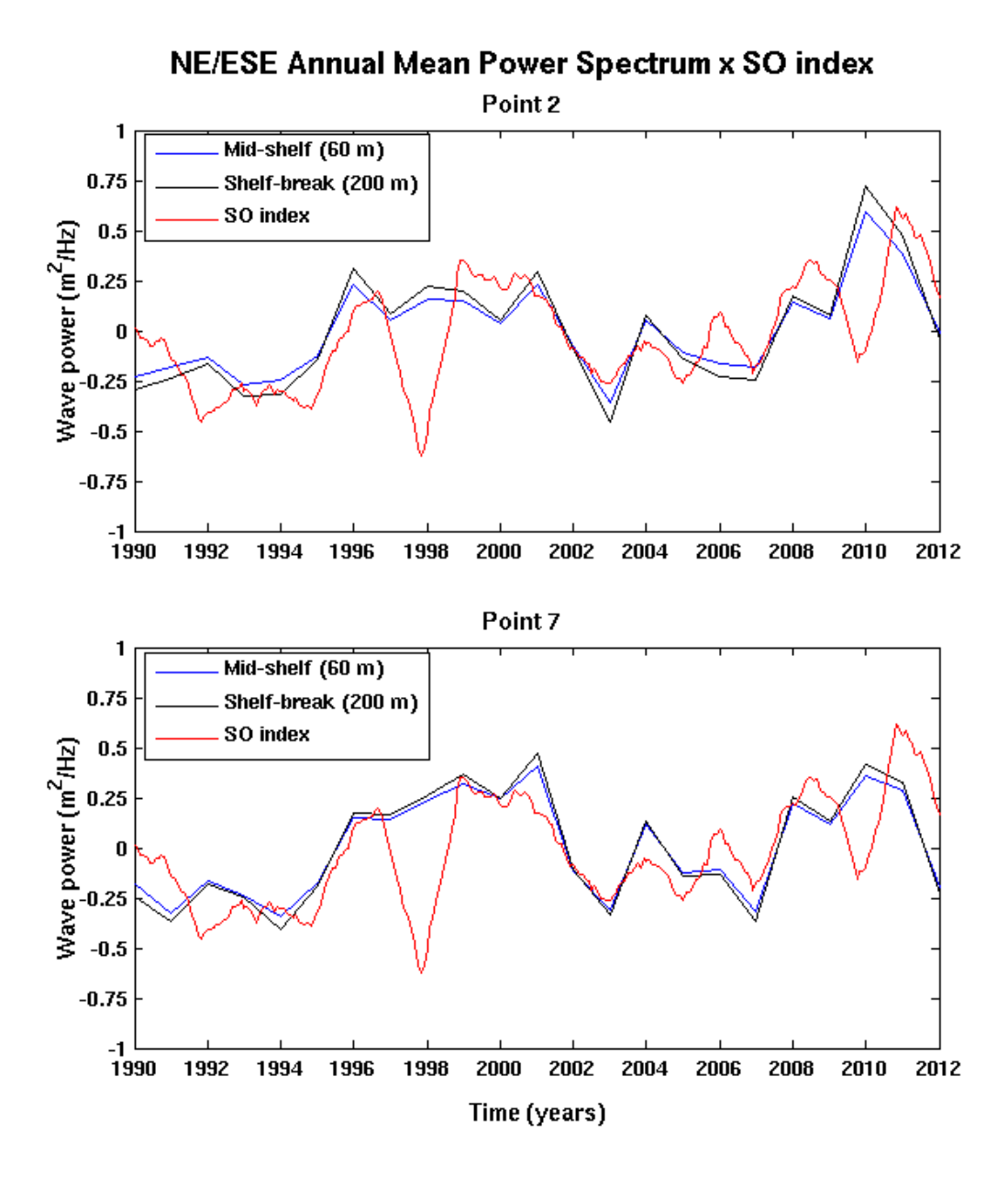


Figure 4.16: Long-term distribution (1990-2012) of the annual mean power spectrum (m²/Hz), integrated over frequencies only between 30° and 120°, for the points 2 (top) and 7 (bottom) at shelf-break (blue line) and mid-shelf (black line). Red line shows the 13 months running mean of the SO index rescaled to the wave power standard deviation.

Additionally, the most significant finding is the correlation of 0.667 obtained between our curves (black and blue lines) and the SO index (red lines) allowing us to state that the modeled wave power from ENE/E is actually modulated by the El Niño Southern Oscillation. As we have seen in chapter 2, the sea level pressure over SBS is also modulated in the same way and, for that reason, we believe that these wave power oscillations are most probably caused by the interannual oscillations of the sea level pressure rather than by synoptic-scale forcing.

Moreover, this is also pointing to the possibility that the overestimation of ENE waves found in the model results could somehow reside in some sort of relaxation of the atmospheric pressure field to the mean condition during the reanalysis processes, especially given the scarcity of in situ observations over the South Atlantic.

Monthly Mean Power Spectrum at 200m (m²/Hz)

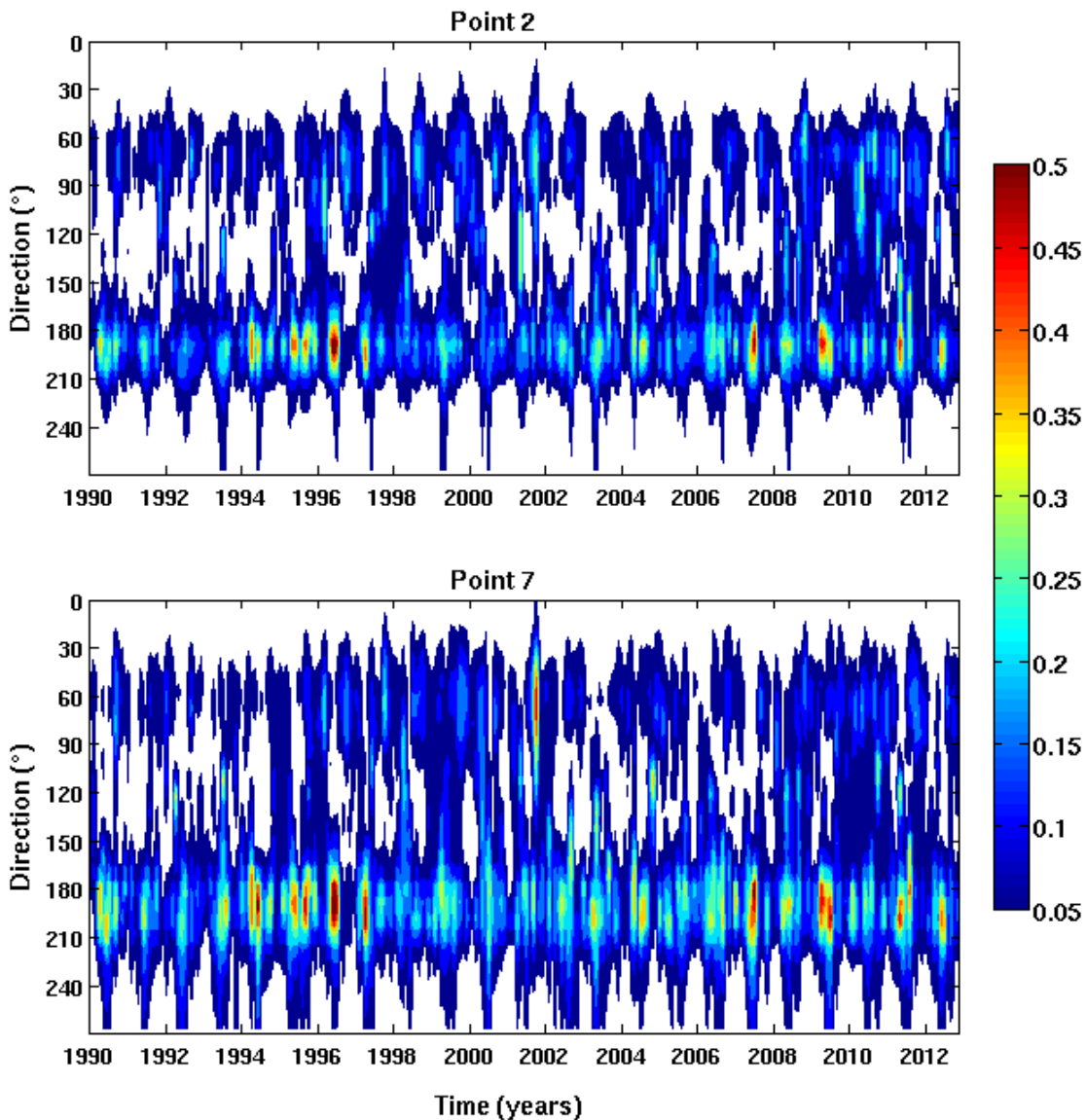


Figure 4.17: Long-term distribution (1990-2012) of the monthly mean power spectrum (m²/Hz) as obtained with our SWAN experiments on the shelf grid, integrated over frequencies, for the points 2 (top) and 7 (bottom) at shelf-break (200 m).

The analysis of the long-term wave power distribution in higher temporal resolution is then made with the use of monthly means of the power spectrum integrated over frequencies, as presented in Figure 4.17 and 4.18 for points 2 and 7 of shelf-break and mid-shelf, respectively.

During the winters, it is possible to see over the shelf-break the occurrence of SW waves in point 2 and even W waves in point 7, due to the greater influence of the westerlies at the southern points, and how they are absent at mid-shelf point 2.

The annual maxima found in the previous figures are now distributed in oscillating values, as for instance the S/SSW maxima of 1994 and 1995, with most of the winters showing in fact a pattern of two maxima with a minimum in the center, which is related to the atmosphere reaching equilibrium near the solstice.

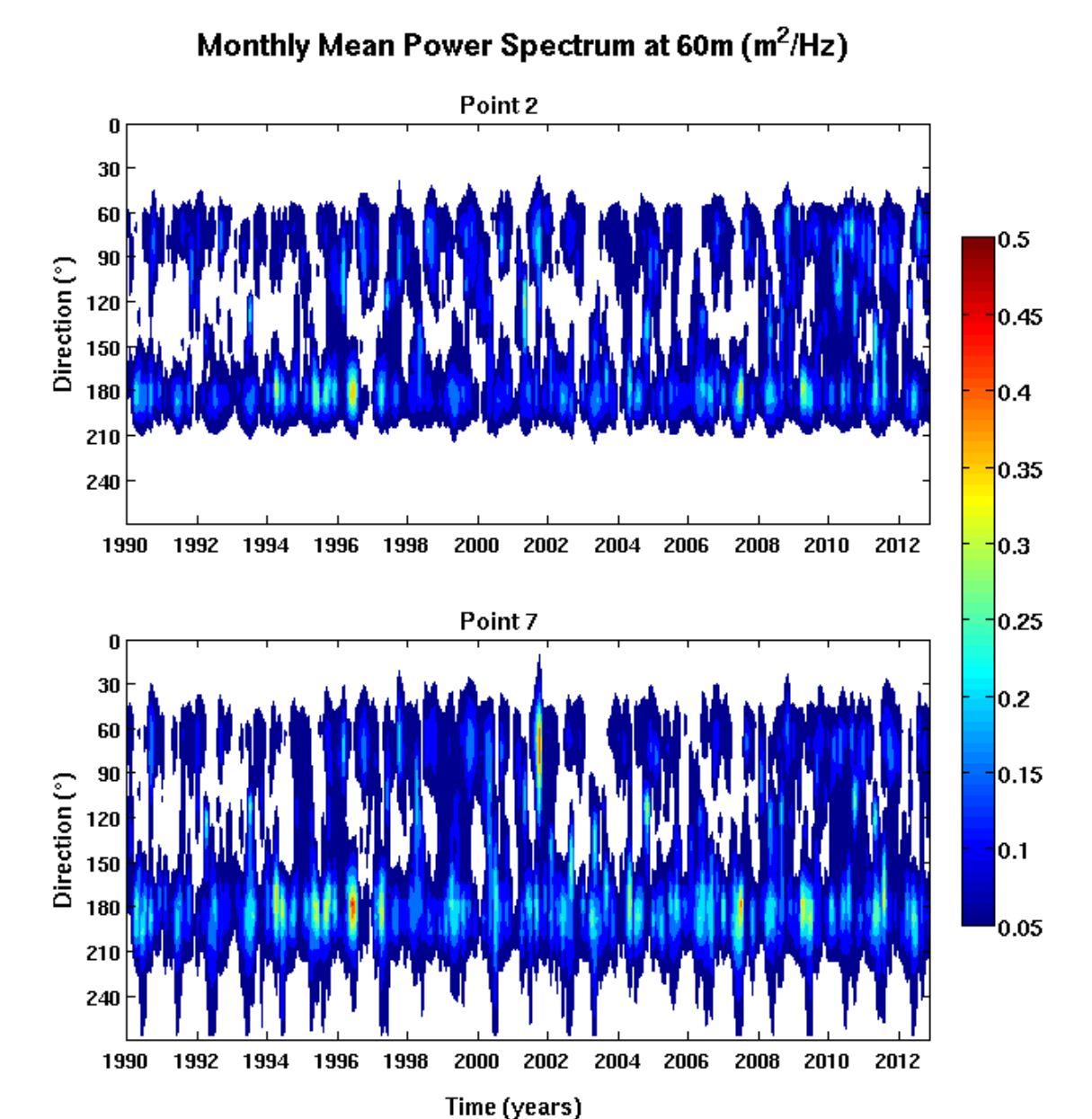


Figure 4.18: Long-term distribution (1990-2012) of the monthly mean power spectrum (m²/Hz) as obtained with our SWAN experiments on the shelf grid, integrated over frequencies, for the points 2 (top) and 7 (bottom) at mid-shelf (60 m).

As expected, strong month-to-month variations are also seen, especially of the S/SSW waves, and we believe they must be in some way direct related to the strong intraseasonal atmospheric oscillations found over SBS, as explained in chapter 2.

Furthermore, it is worth to notice how the natural aliasing of information on any mean can influence the interpretation as in the case of the isolated NE/E maximum of point 7 in 2001 or in situations with none ENE/E waves like in 2003, which are not satisfactorily represented in the annual means.

In Figures 4.19 and 4.20 we present the intra-annual distribution of the six-hourly long-term (1990-2012) mean power spectrum, integrated over frequencies, for the points 2 (top) and 7 (bottom), respectively at shelf-break and mid-shelf.

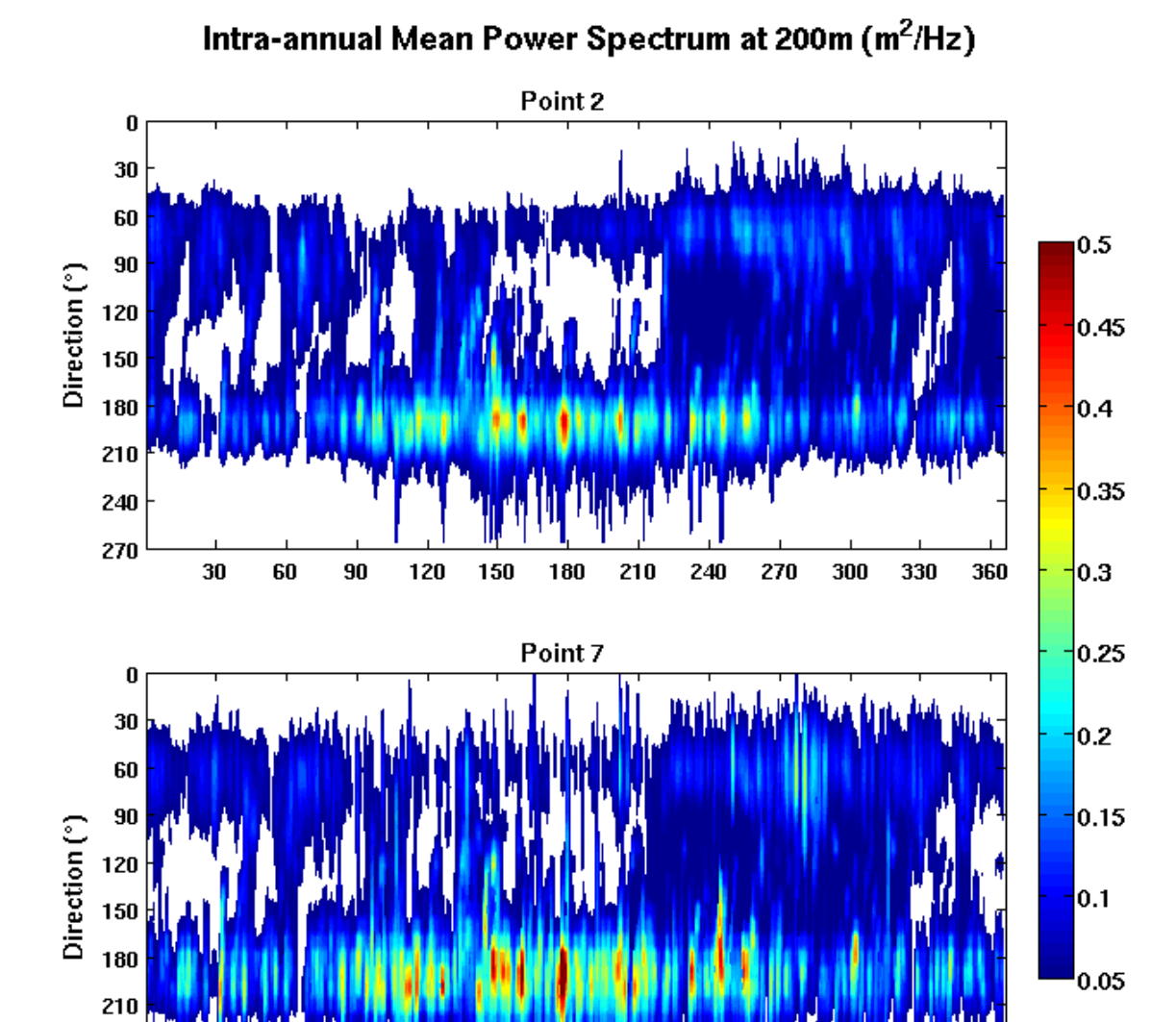


Figure 4.19: Intra-annual distribution of the six-hourly long-term (1990-2012) mean power spectrum (m²/Hz) as obtained with our SWAN experiments on the shelf grid, integrated over frequencies, for the points 2 (top) and 7 (bottom) at shelf-break (200 m).

Time (days)

In both figures, the core of S/SSW waves occurs centered in wintertime between April and September, but especially in point 7 there are secondary high waves occurrences in the rest of the year too.

There is also an ENE/E core that occurs mainly during the springs in opposition to the lower powers found during wintertime. During October in point 7 the peaks of ENE/E waves attain elevated values while the S/SSW waves show a power decrease. Secondary isolated peaks are also seen during March in point 2 and during May and July in point 7.

Worthwhile to notice that during the springs there is a SE low power area in dark blue connecting both previous mentioned patterns. Highest SE waves occur mainly during April and May and secondarily during the spring and are associated with the cyclones.

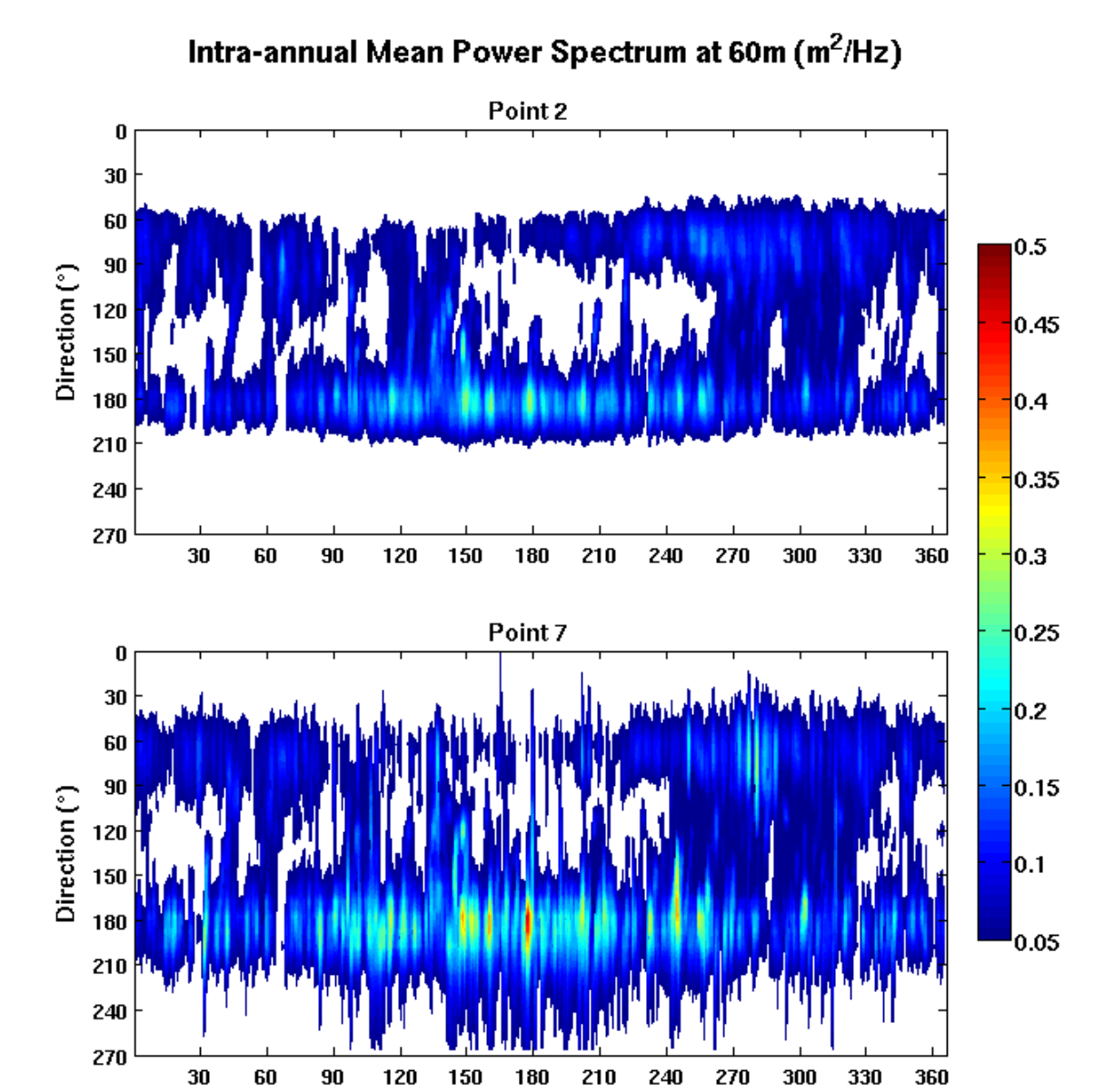


Figure 4.20: Intra-annual distribution of the six-hourly long-term (1990-2012) mean power spectrum (m²/Hz) as obtained with our SWAN experiments on the shelf grid, integrated over frequencies, for the points 2 (top) and 7 (bottom) at mid-shelf (60 m).

Time (days)

In this six-hourly resolution it is clearly possible to see how some waves do occur at shelf-break coming from the continent (270°), especially in point 7 but also in point 2 during the winter. At mid-shelf point 2, however, such phenomenon is very much reduced due to the tiny distance to the shore.

The long-term (1990-2012) monthly mean maps of sig. wave height over the SBS are then presented in Figure 4.21 to show the spatial relations on the intra-annual distribution. As previously seen, the higher monthly mean waves occur during half of the year, centered in wintertime between April and September. No particular pattern emerges from this intra-annual distribution of monthly mean maps with exception for September, when higher energy is seen near the coast off the northern coastal projection and offshore values get higher than the previous month.

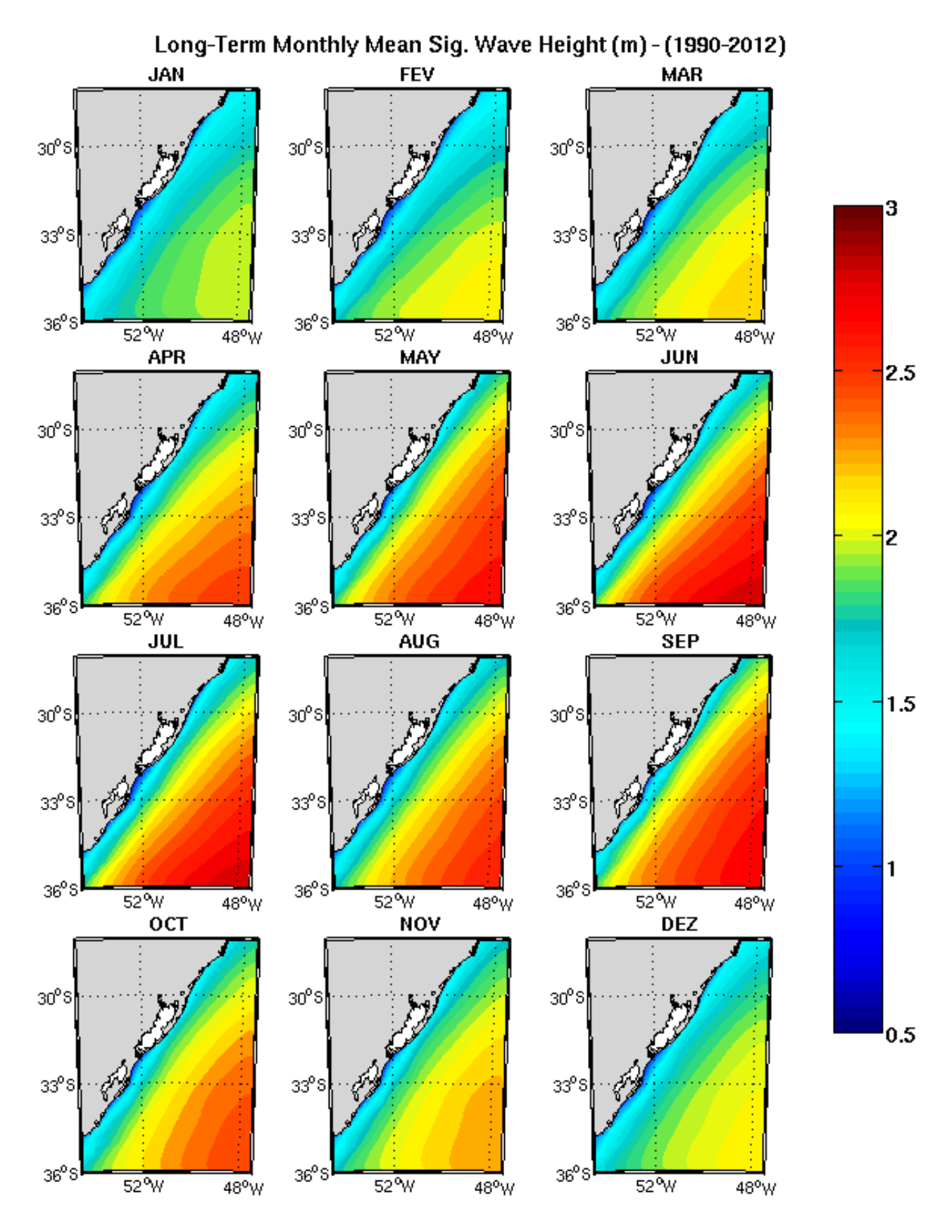


Figure 4.21: Long-term (1990-2012) monthly mean maps of sig. wave height over the SBS as obtained with our SWAN experiments on the shelf grid.

Long-Term Mean Sig. Wave Height (m) - (1990-2012)

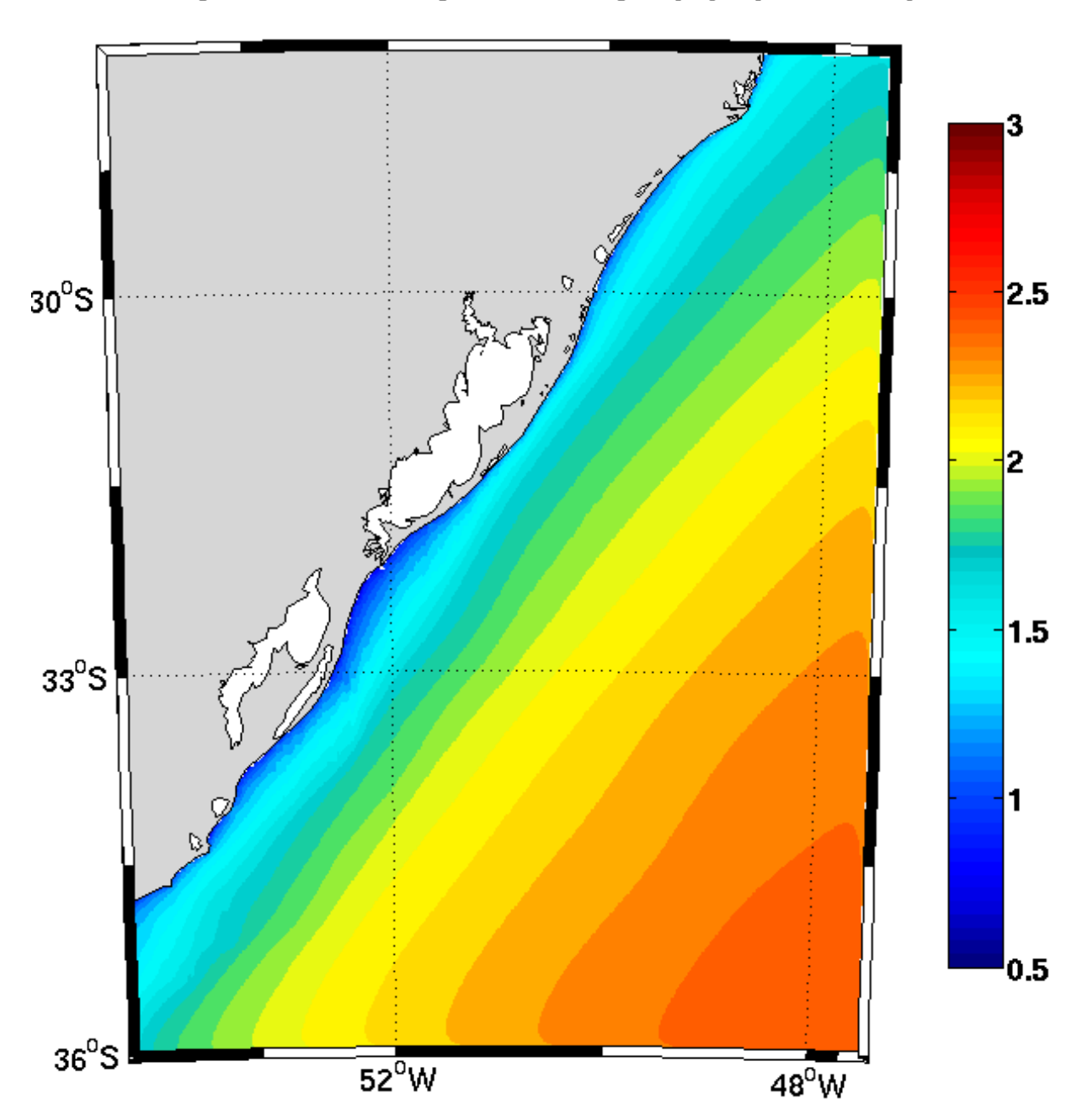


Figure 4.22: Long-term (1990-2012) mean map of sig. wave height over the SBS as obtained with our SWAN experiments on the shelf grid.

Finally we present in Figure 4.22 the long-term (1990-2012) mean map of sig. wave height over the SBS, which defines the mean wave energy distribution. Maximum energy is found way offshore in the southeastern corner of the grid, where it attains up to 2.4 m of sig. height, and minima are found near the coast.

Along-shelf wave energy gradients near the coast are already seen on this resolution, with higher energy located off both capes and off the northern coastal projection and only secondarily off the southern coastal projection. On the other hand, energy minimum is found between coastal projections off Rio Grande (32.5 °S) and secondarily between capes and coastal projections.

The offshore outer and mid-shelf declivities are not reflected on this energy pattern as no differences are found between the mean energies over the northern and southern parts of SBS, other than the slight northward decrease of the higher waves. Nearer to the coast, however, over depths shallower than 40 m the energy pattern does follow the bathymetric contours after a considerable drop of wave energy caused by bottom friction.

The mean wave base or the isobath after which the waves are expected to have strong influence over the transport of bottom sediments is a major feature of coastal dynamics as it can be used to define the lower limit of a wave-dominated shoreface.

This depth can be indirectly inferred from the mean wave energy distribution previously described as much as bottom sediment transport can be considered proportional to the friction exerted by the fluid. Therefore, based on our results, we suggest the 40 m depth as the present day mean wave base and consequently the lower limit of the present SBS shoreface.

This conclusion is actually in close agreement with the findings of Almeida et al. (1999) who defined as 36 m the depth of the external or oceanic limit of the so called profile of equilibrium at the northern part of the SBS. They took the few available wave data at that time and used on the empirical function described in Hallermeier (1981 a,b) and Birkemeier (1985), which takes into account the sig. wave height and period along with the mean diameter of the sediment.

Moreover, this 40 m depth limit is in fact coincident with the approximate lower limit of the nearshore belt of sandy sediments covering the SBS, as described by the maps of surface sediment composition (e.g. Martins and Urien, 1977; Corrêa et al., 1996; Figueiredo Jr and Tessler, 2004).

In this sense, we can also state that this general absence of the finer sediments near the coast acts then like a proxy of the elevated wave shear stress exerted by the fluid on the bottom in this shallower region and thus corroborates with the definition of the 40 m isobath as the present lower limit of the SBS shoreface.

4.3 SBS Shoreface wave conditions

For simplicity and practicality purposes we can subdivide the SBS shoreface (Figure 4.23) in only three distinctive regions. Two sand ridge fields with different characteristics are located near each of the coastal projections, thus defining the first two shoreface regions which are separated from each other at around 32.5 °S off Rio Grande. As a consequence, in between the center of the northern coastal projection and the Santa Marta Cape a third region without any sand ridge can be defined.

The southern shoreface sand ridges are large morphological features marked by their great curvatures and by their opening to the south. They are present at the lower shoreface between 12 and 30 m depth with heights between 4 and 10 m, widths between 2 and 8 km and lengths up to 40 km.

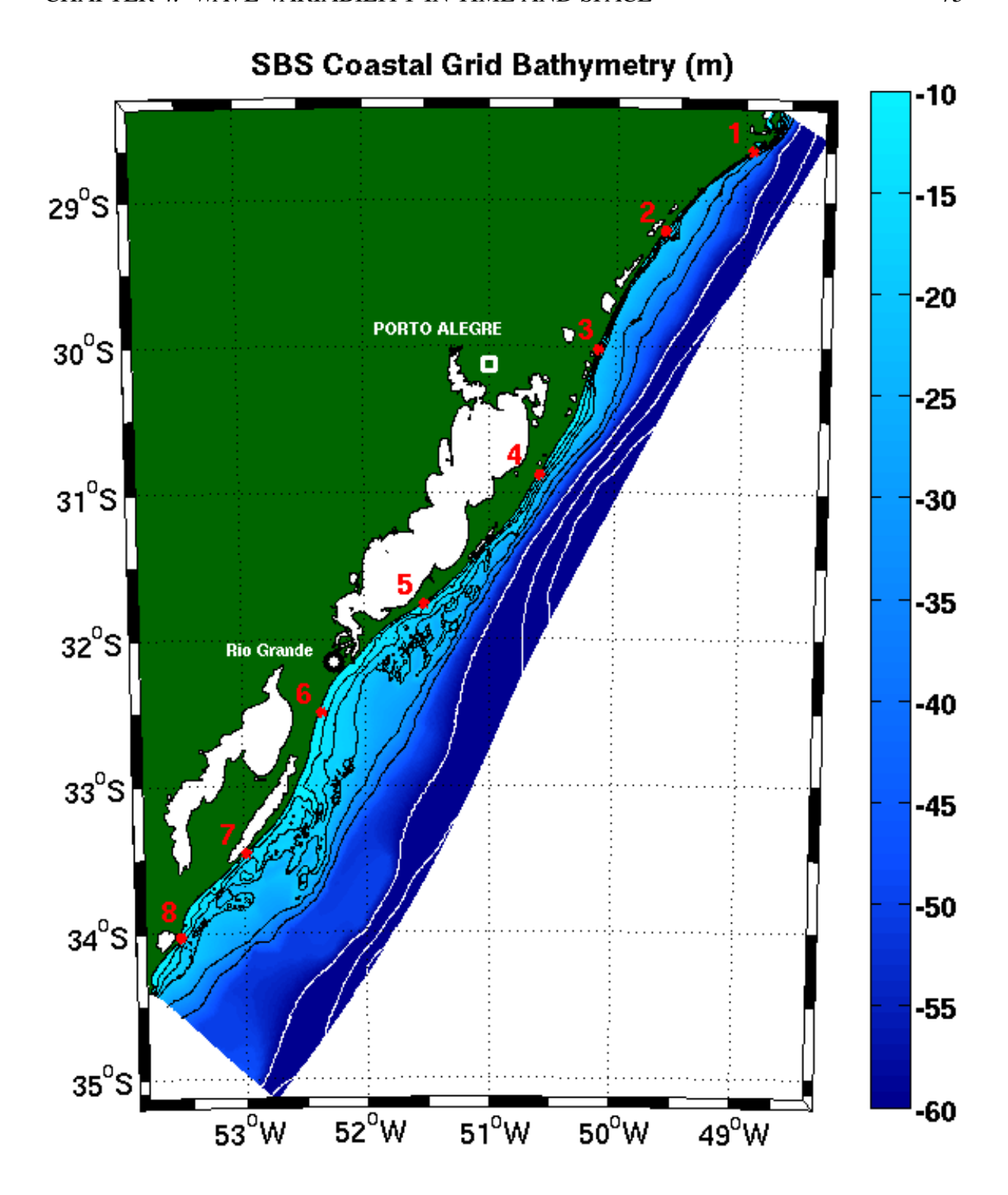


Figure 4.23: Curvilinear Coastal grid bathymetry (m) showing the eight chosen points for upper shoreface wave power spectra analysis along the 6 m isobath (red asterisks). Black isolines are for 12, 16, 20, 30 and 40 m depth and white isolines are for 60, 80 and 100 m depth.

Some of these ridges are connected to the upper shoreface and some are not. The most prominent ridge, called Albardão (33 °S), is not merely connected but also shows an orthogonal orientation to the coast with its top reaching only 7 m depth as far as 20 km off the shoreline.

The central shoreface sand ridges present similar dimensions when compared to the southern ridge field but with much more discontinuities. On the other hand, they are mostly linear and aligned to the general NE/SW orientation of the shelf and coast. They are also sometimes

obliquely connected to the upper shoreface but with far shorter dimensions than the Albardão ridge.

Anyhow, both ridge fields are well within shoreface depths and therefore are currently subject to wave action, which means that they represent a remarkable obstruction to wave energy propagation until the shore.

In order to define the general wave energy distribution over the shoreface we show in Figure 4.24 the four maps of long-term (1990-2012) mean sig. wave height over the SBS as obtained with our SWAN model results from the four experiments on the higher-resolution curvilinear coastal grid, detailed in chapter 3. In all four experiments it is possible to see the considerable drop of wave energy over depths shallower than 40 m with the energy pattern approximately following the bathymetric contours.

Although the absolute values of the along-shelf wave energy gradients do vary, the general maxima and minima positioning in the four coastal grid experiments are virtually identical to those found on the shelf grid, i.e. higher values are seen near capes and coastal projections while lower values are seen between them. The increased resolution, however, allow us to fine-tuning this statement by recognizing that the Polonio cape and especially the southern coastal projection are under lower mean wave energy than respectively the Santa Marta cape and the northern coastal projection, in a more direct relation with the local shoreface width.

In the experiments three and four (without wind), whose quantitative validation already did point out a reduction of wave energy, the mean maps show how this energy reduction occurs over the entire grid rather than only over the shoreface. In experiments two and four (with smaller friction), on the other hand, it is possible to quantify the enhancement of the mean wave heights over the shoreface in relation to the experiments one and three (with default friction).

Willing to address the proper significance of these values of wave heights we show in Figure 4.25 the four maps of long-term (1990-2012) mean relative sig. wave height over the SBS (i.e. the sig. height divided by the local depth). In this figure it is made clear the geomorphological separation between the huge lower shoreface (in two light blue shades) and the greater declivities of the tiny upper shoreface and the Albardão ridge (in red, orange and green shades). Moreover, it is also worth to notice that such classification holds for all four experiments, in spite of the energy reduction in the experiments without wind or the energy enhancement in the experiments with smaller friction.

Henceforth, for the spectra analysis in space and time of the SBS shoreface wave climate we used the results of our SWAN experiment number two on the coastal grid, once it scored the best validation skills in chapter 3.

In Figure 4.26 we show then the long-term mean (1990-2012) power spectra for eight upper shoreface points chosed from north to south over the 6 m isobath (Figure 4.23, red asterisks). The more remarkable finding is the almost full refraction observed between the previous found bimodal offshore spectra and these upper shoreface spectra that are mostly found as ESE/SSE waves with increased SE wave importance and in an almost unimodal spectra, which is in absolute accordance with the local wave measurements.

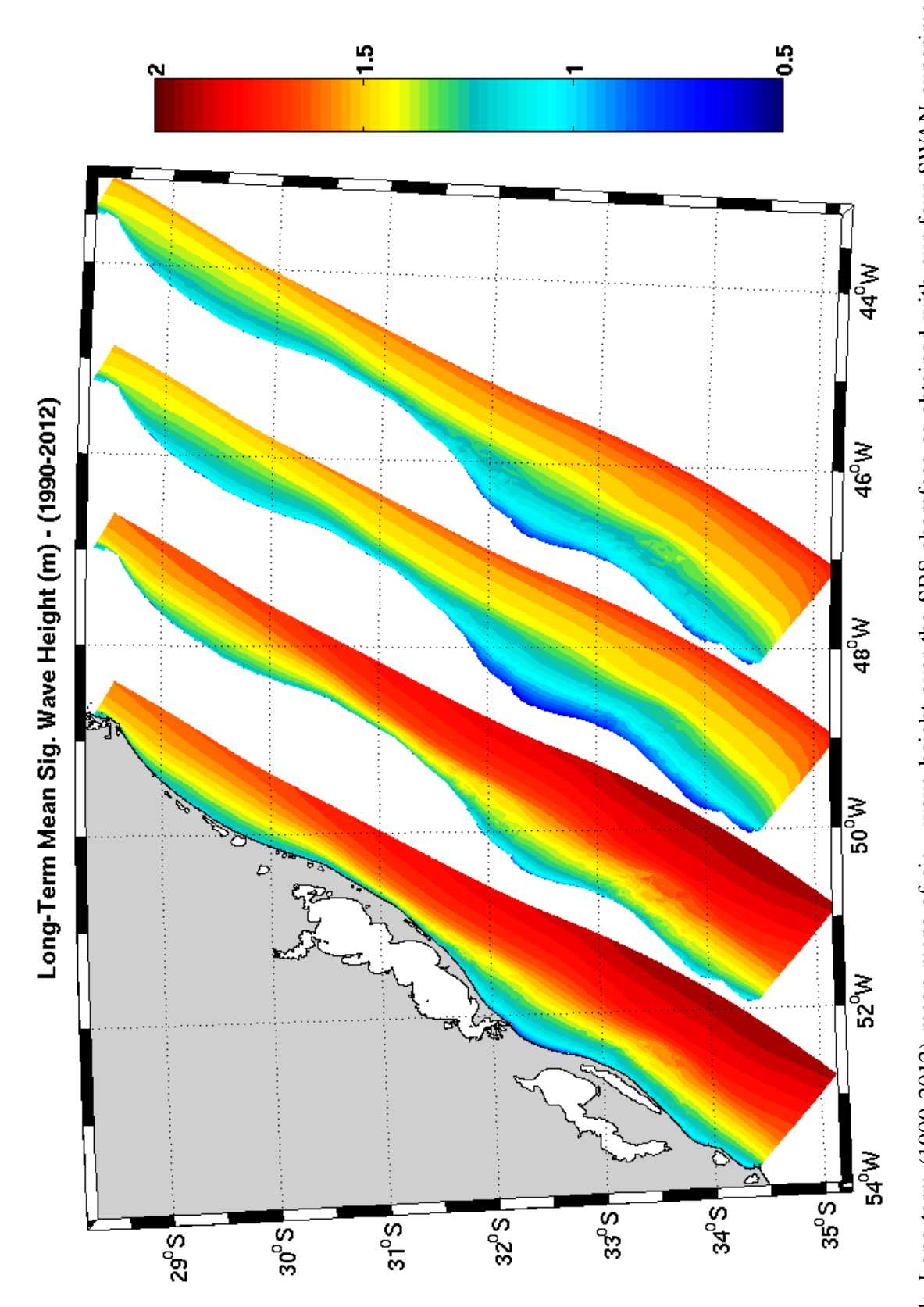


Figure 4.24: Long-term (1990-2012) mean maps of sig. wave height over the SBS shoreface as obtained with our four SWAN experiments on the curvilinear coastal grid. Experiments one to four are shown respectively from left to right.

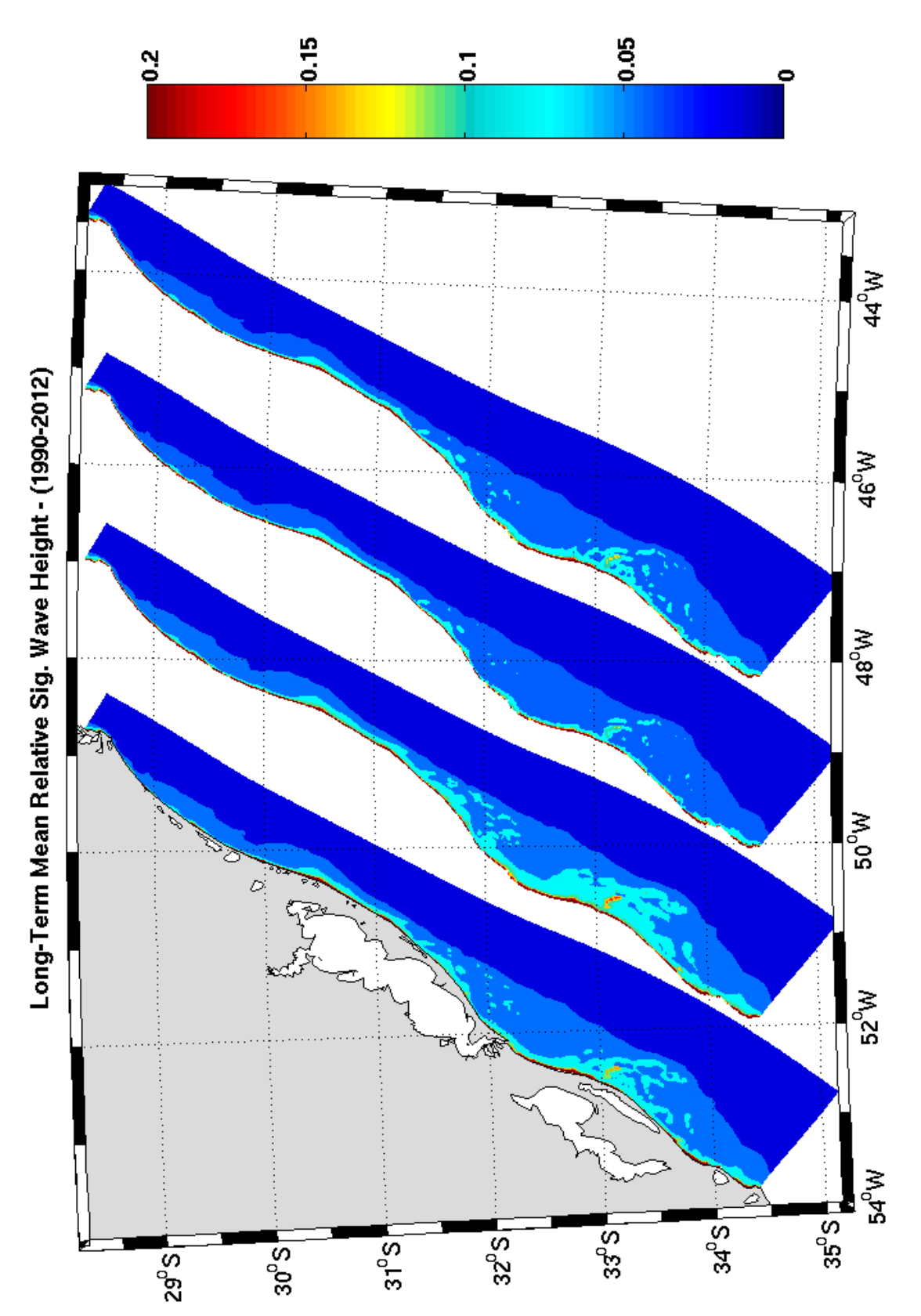


Figure 4.25: Long-term (1990-2012) mean maps of relative sig. wave height over the SBS shoreface as obtained with our four SWAN experiments on the curvilinear coastal grid. Experiments one to four are shown respectively from left to right.

These results show how the large and shallow SBS shoreface is responsible for an intense refraction of the waves (over 45°), thus forcing them to approach the beach system with very small angles of attack (< 10°) in relation to the shore normal. The important consequence for sediment dynamics is straightforward, once the so called littoral drift is considered proportional to this angle (e.g. Komar, 1998), and shall be dealt with in future experiments using sediment transport calculations.

The eight spectra can be separated in northern points with higher wave powers (one to four) and southern points with lower wave powers (five to eight). Therefore, while offshore mean wave power showed a small and smooth northward decrease with spatial patterns that do not follow bathymetric contours, the upper shoreface mean wave power, on the contrary, varies abruptly decreasing from the half north to the half south points, in a clear response to offshore mid-shelf declivities.

This is because during higher-energy events considerable bottom friction may occur way offshore making the energy of those waves to decrease differentially between the northern and southern portions of the mid-shelf, thus affecting the shoreface widths and also the mean wave power at upper shoreface. It means that, even though mid-shelf declivities are not reflected on the mean offshore wave energy or power patterns, still they represent an important factor on the along-shelf variability by allowing a north/south differentiation of the higher waves attenuation.

This finding corroborates the previous statement that the mean energy of the waves reaching the upper shoreface of the SBS appears to be inversely proportional to shoreface width, which is influenced by the mid-shelf declivities. This lead us to the important conclusion that the geological inheritance, expressed through the shoreface width and the offshore mid-shelf declivities, might indeed most times be more important to generate wave variability than the offshore wave power along-shelf variations itself.

Additionally, another feature drawing attention in Figure 4.26 is the similarity between the power spectra of points 1, 5 and 7, which present a clear focus of SSE waves. This finding is direct related to shoreline orientation as these three points face SSE and are positioned to the south of the northern cape and both the coastal projections, respectively.

We strongly believe that this phenomenon is caused by a windowing on the wave propagation until the shore. Once the greater is the refraction the greater is also the travelled distance of the wave, one can expect the maximization of bottom friction over refracted waves and, on the other hand, a minimization of bottom friction over poorly refracted ones, which travel shorter distances. The immediate consequence is that shore normal waves reach the coast with higher energy than angled incoming waves.

These three points, therefore, must be compared against points 6 and 8 (which face ESE) and secondarily against point 2 (which faces SE), once they are positioned immediately to the north of the southern cape and both the coastal projections. In much the same way as in points 1, 5 and 7, the shore normal waves also show power enhancements, although with a lower intensity. The SSE waves, in this case, are very much reduced or inexistent, indicating the sheltering effect caused by the capes and coastal projections through the induction of downwave refraction.

Long-Term Mean Power Spectrum at 6m (m²/Hz)

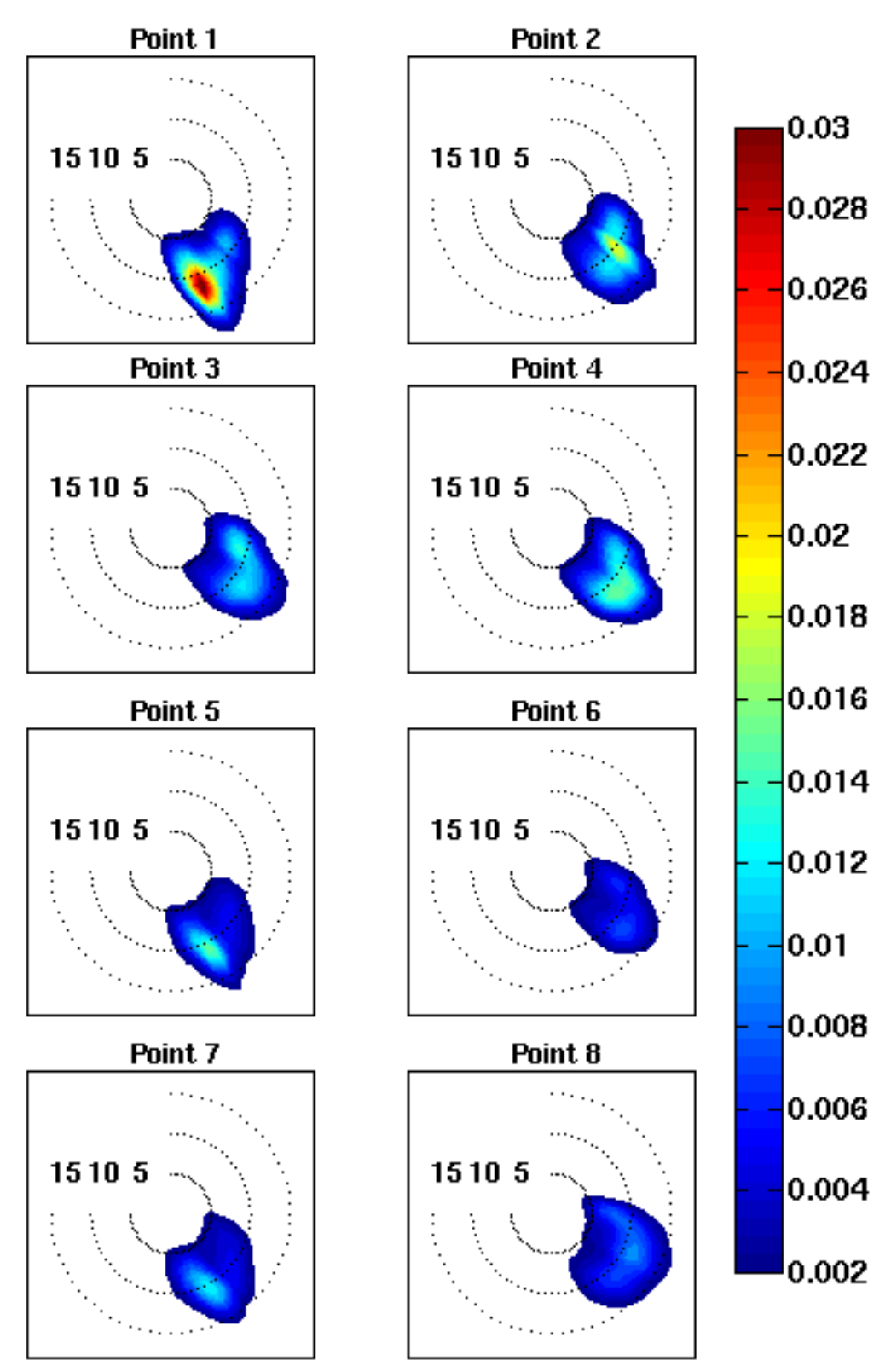


Figure 4.26: Long-term (1990-2012) mean wave power spectrum (m2/Hz) as obtained with our SWAN experiment number two on the curvilinear coastal grid, for the eight points selected at upper shoreface (6 m).

The consequence is that at the spaces between capes and coastal projections, where lower wave energies were found (Figures 4.22 and 4.24), there is a remarkable north/south asymmetry with higher energies to the north because of this refraction windowing.

Implications for coastal evolution will be dealt with in a future experiment, but this north/south asymmetry pattern closely fits the relative positioning of the different types of Holocene coastal barriers, as described in Dillenburg et al. (2009).

Altogether, it is possible to state that bottom friction plays a major role on wave differentiation along the SBS shoreface either by acting over different amounts of refraction or by acting over the different shoreface widths. In this sense, these results allow us to define the shoreline orientation, the shoreface width and the offshore mid-shelf declivities as the key factors determining the wave power spectra that ultimately reach the shore of the SBS.

For the temporal analysis of these results we present in Figures 4.27 and 4.28 the long-term distribution of the annual mean power spectrum, integrated over frequencies, for the eight points chosen at the upper shoreface. The sharp north/south power difference along the shelf is again made clear with the northern points in Figure 4.27 showing red and orange shades that do not appear in the southern points (Figure 4.28). The high interannual wave power changes closely follow the variations previously found in the mid-shelf spectra with the clear enhancement of ESE waves during La-Niña years.

These figures show the concentration of wave power sometimes occurring in a straight line over the full experiment, with different directions for adjacent points like in points 1 and 2, that does not occur in points 3 and 4 (Figure 4.27). In point 1, we have the maximum power clearly centered in 160° with occurrences of 130° waves, while in point 2 we have the maximum in the shore normal (130°) , but in great similarity with points 3 and 4, we also have waves from 120° and 140° .

The points 5 and 7 also show these straight line wave power concentrations in the shore normal direction, while the absence of SSE wave energy is clear in points 6 and 8 with the extreme attenuation of the ESE and SE waves in point 6 (Figure 4.28). The two cores of directions are now approximately in 130° and 155° for points 5 and 7, while in point 6 they are in 100° and 130°. In point 8 the SSE waves seem totally blocked and the cores are in 90° and 120°.

These results reinforce the role of shoreline orientation showing that the previous found offshore waves that come from ENE (70°) and SSW (190°) are now found refracted up to 60° as in points 1 and 5 (for ENE waves) and in points 3 and 6 (for SSW waves). For the same reason, it is worth to notice how the southernmost point receives the minimum of offshore SSW wave power while the northernmost point receives the maximum of this power, in total opposition to what one could intuitively expect, once the SSW offshore wave power smoothly decreases to the north.

As we have mentioned earlier, the annual mean wave power might present considerable aliasing of information on a synoptic-scale dominated system and for that reason we present in Figures 4.29 and 4.30 the long-term distribution (1990-2012) of the monthly mean power spectrum, integrated over frequencies, for the eight points chosen at the upper shoreface.

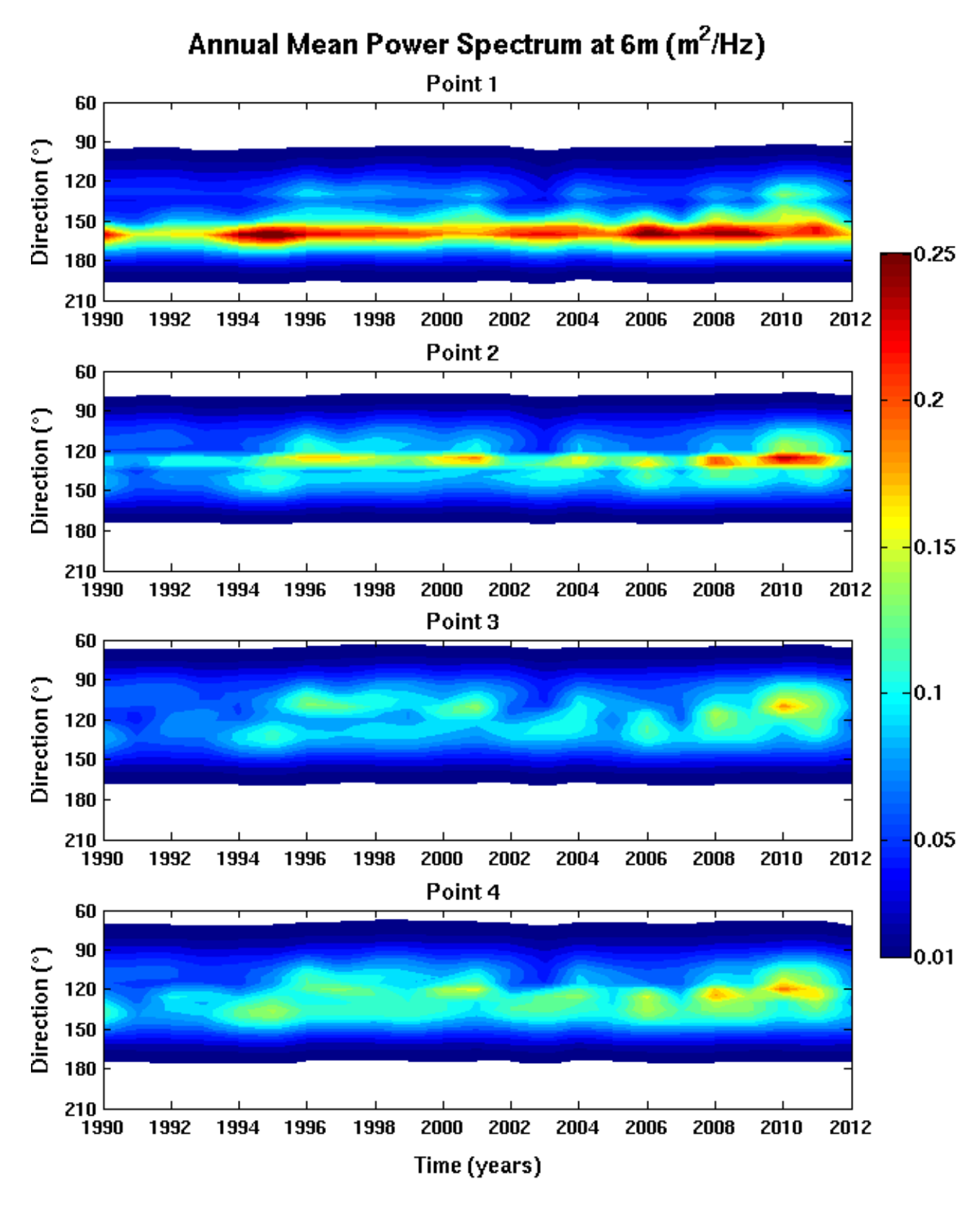


Figure 4.27: Long-term distribution (1990-2012) of the annual mean power spectrum (m2/Hz) as obtained with our SWAN experiment number two on the curvilinear coastal grid, integrated over frequencies, for the points 1 (top) to 4 (bottom) at upper shoreface (6 m).

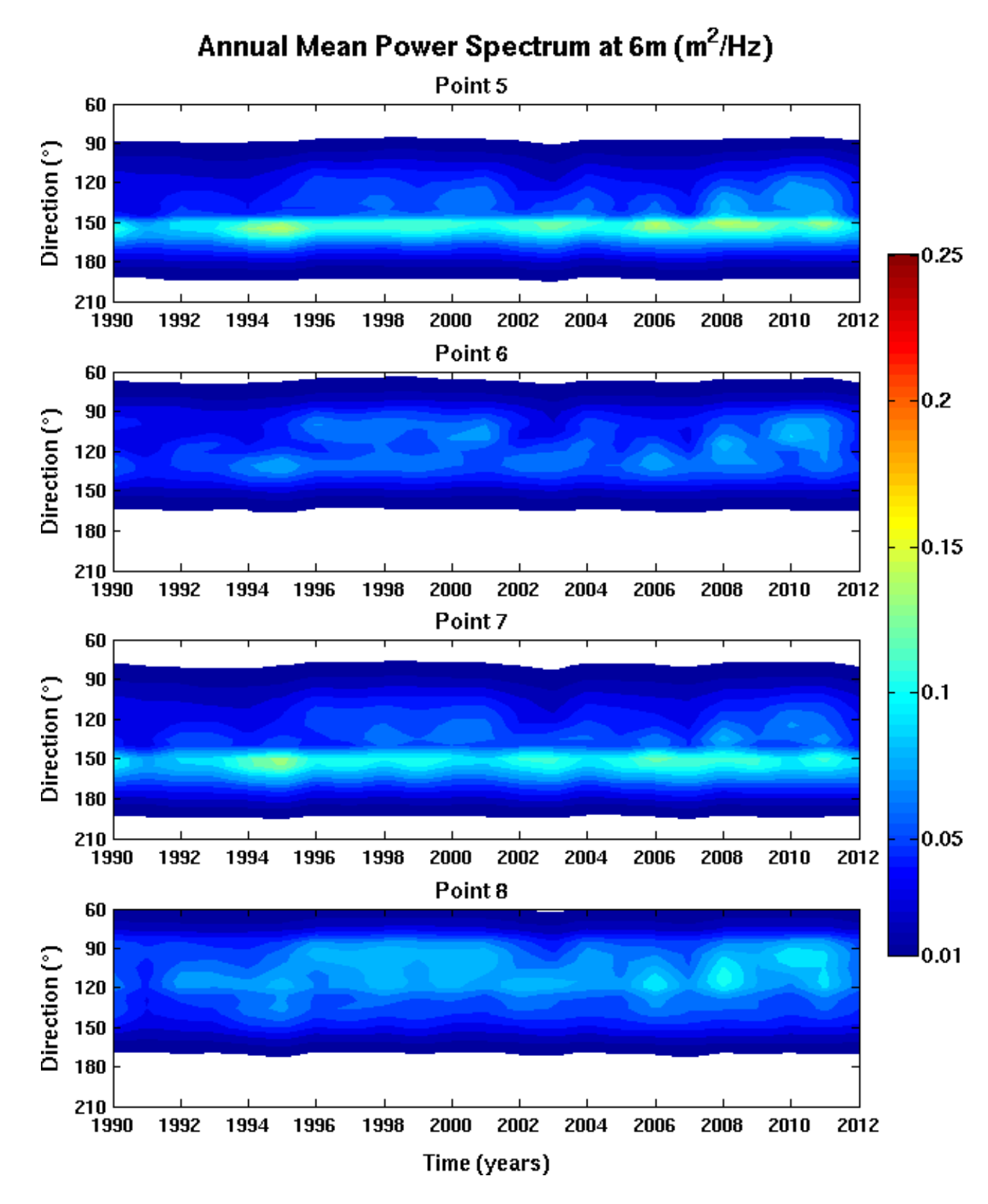


Figure 4.28: Long-term distribution (1990-2012) of the annual mean power spectrum (m2/Hz) as obtained with our SWAN experiment number two on the curvilinear coastal grid, integrated over frequencies, for the points 5 (top) to 8 (bottom) at upper shoreface (6 m).

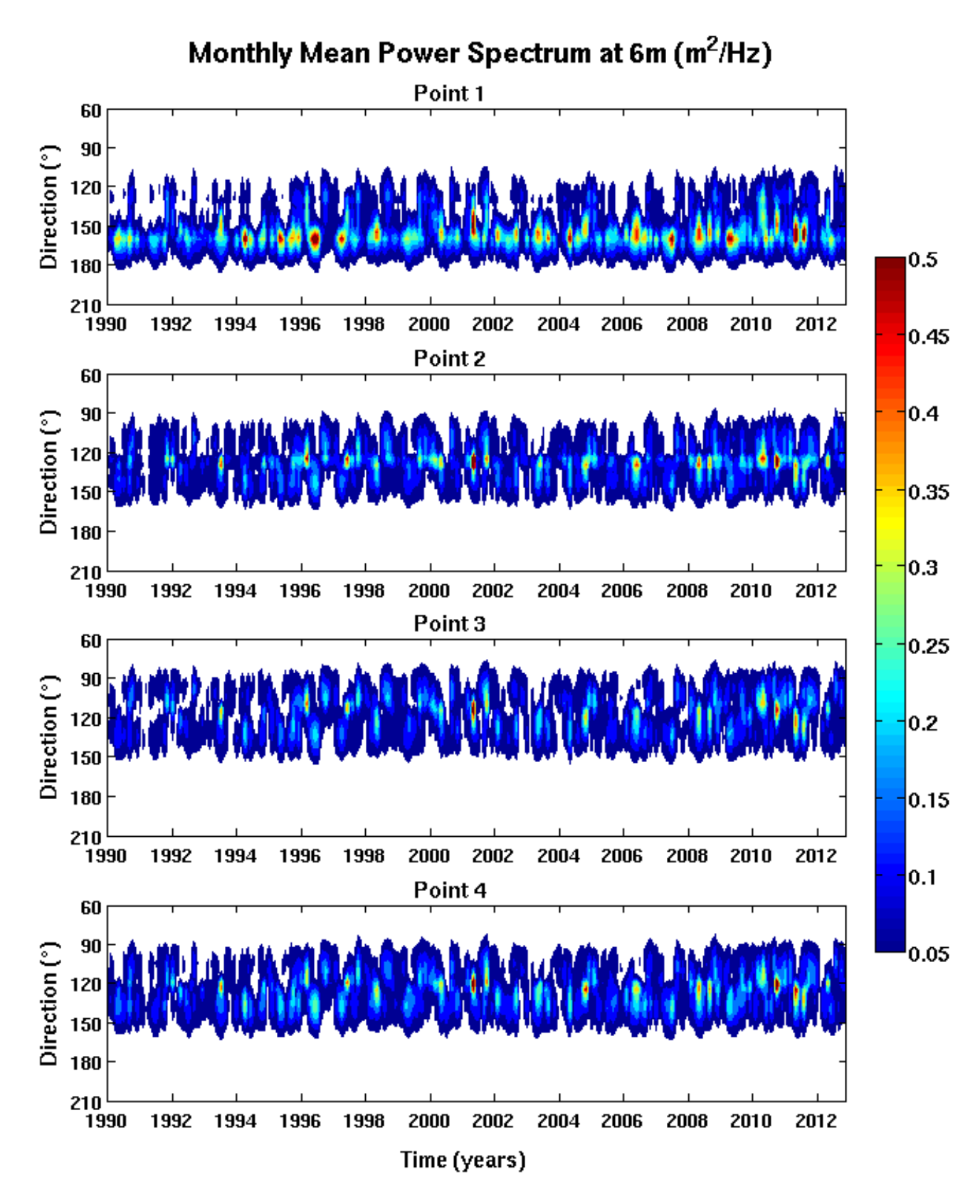


Figure 4.29: Long-term distribution (1990-2012) of the monthly mean power spectrum (m2/Hz) as obtained with our SWAN experiment number two on the curvilinear coastal grid, integrated over frequencies, for the points 1 (top) to 4 (bottom) at upper shoreface (6 m).

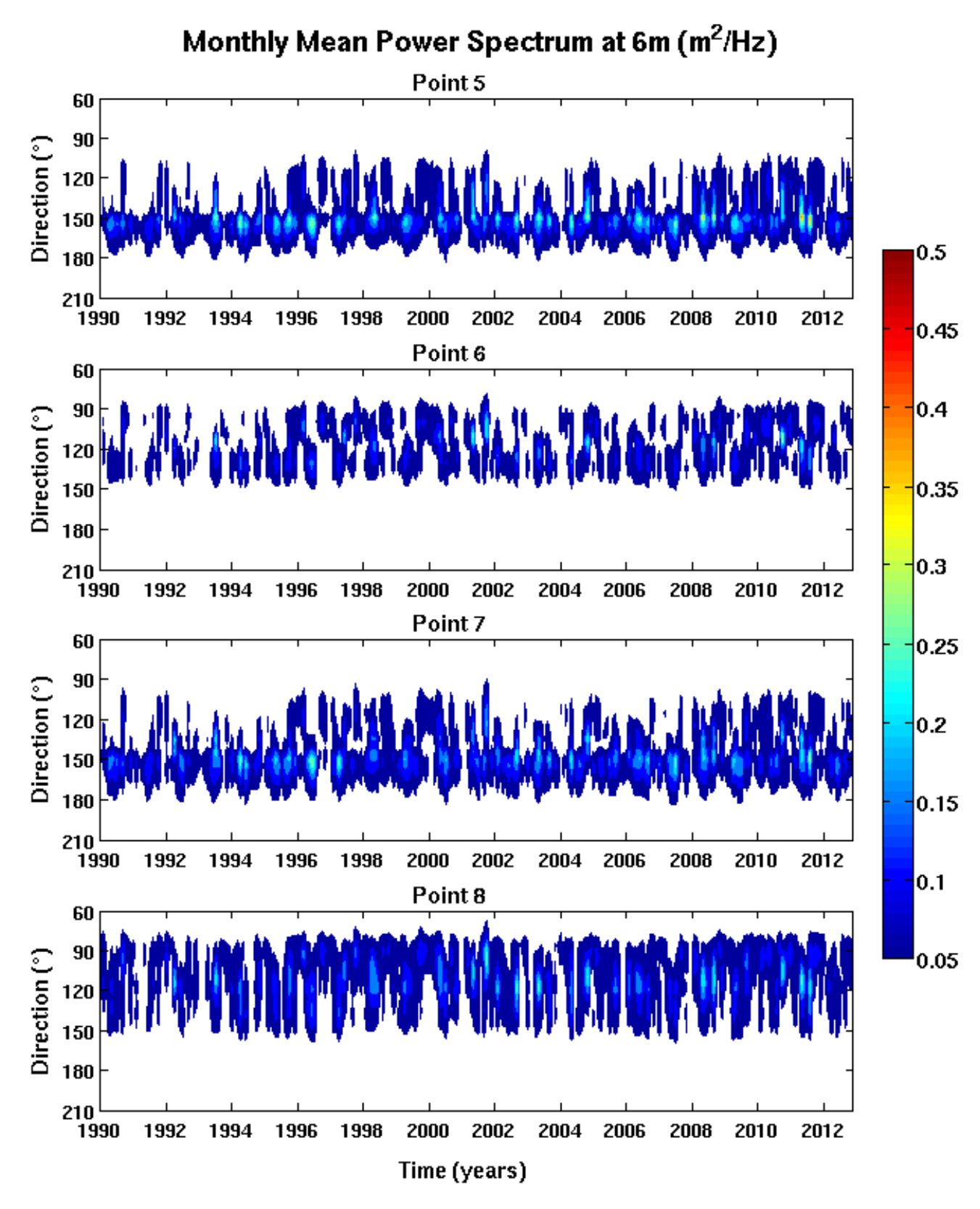


Figure 4.30: Long-term distribution (1990-2012) of the monthly mean power spectrum (m2/Hz) as obtained with our SWAN experiment number two on the curvilinear coastal grid, integrated over frequencies, for the points 5 (top) to 8 (bottom) at upper shoreface (6 m).

These higher temporal resolution results show us how large it is the variability of wave events over the SBS. In both figures it is possible to see that wave powers actually occur as isolated peaks over favored directions rather than as a straight line like in the annual means. The north/south power differences are still very clear as much as the asymmetry between adjacent points and the maximum attenuation on point 6.

Moreover, it is also possible to see that point 1 and especially points 5 and 7 are most times sheltered from the ESE and SE waves, which only appear with low power during La Niña years. On the other hand, in points 6 and 8 the SSE waves are almost inexistent and even E waves are seen with significant powers.

4.4 Concluding remarks

Initially, we used our long-term wave model results to show how the South America blocks the waves generated by the westerlies, which only become high again well within the South Atlantic, characterizing the western and southwestern South Atlantic shelves with a general low energy mean wave climate. Lower long-term mean peak wave periods were also found over and around the SBS indicating two important wave generation regions that result from the winds of the SAH and from the winds of extratropical cyclones and the associated frontal systems.

We then showed examples of the extreme wave patterns induced by the presence of cyclones around the three clearly distinguishable regions of cyclogenesis maxima over the western South Atlantic. Particular pre and post frontal conditions were also shown to fully characterize the synoptic-scale changes in the wave directions.

The long-term mean offshore spectra showed a predominance of the SSE/SW waves with power peak between S/SSW, generated by the cyclones and fronts, with a secondary power peak composed by ENE/E waves that were generated by the post-frontal winds, corroborating with the statement that the SBS is essentially bimodal in wave directions. The power of S/SSW waves diminish northward and the power of ENE/E waves secondarily diminish southward, allowing us to state that the SBS is located in the encounter between the influence of the westerlies and cyclones and the influence of the SAH, at least regarding wind-waves generation and in present day atmospheric conditions.

The interannual distribution as annual means showed a distinctive rise in ENE/E wave power and secondarily in the ESE wave power. The coincidence between these rising periods and the known peaks of La Ninã lead us to the comparison between the ENE/ESE offshore wave power spectra and the Southern Oscillation index for the 23 years of the experiments. Subjective comparison and a correlation of 0.667 allowed us to state that the annual mean wave power from ENE/ESE, as obtained in the model, is actually modulated by the El Niño Southern Oscillation.

The interannual distribution as monthly means showed, as expected, strong month-to-month variations confirming the natural aliasing of information of an annual mean. During the winters, it is possible to see over the shelf-break the occurrence of SW waves and even W waves at the

southern points. Most of the winters showed in fact a pattern of two maxima with a minimum in the center, which is related to the atmosphere reaching equilibrium near the solstice.

The six-hourly intra-annual distribution showed a core of S/SSW waves occurring centered in wintertime between April and September, but especially in the south there are secondary high waves occurrences in the rest of the year too. In this time resolution it was clearly possible to see how some waves do occur at shelf-break coming from the continent. There is also an ENE/E core that occurs mainly during the springs in opposition to the lower powers found during wintertime. Highest SE waves occur mainly during April and May and secondarily during the springs and are associated with the cyclones.

The long-term mean map of sig. wave height over the SBS was used to define the mean wave energy distribution. Along-shelf wave energy gradients near the coast are already seen on the 2 km resolution shelf grid, with higher energy located off both capes and off the northern coastal projection and only secondarily off the southern coastal projection. On the other hand, energy minimum is found between coastal projections off Rio Grande (32.5 °S) and secondarily between capes and coastal projections.

The offshore outer and mid-shelf declivities are not reflected on this energy pattern as tiny differences were found between the mean energies over the northern and southern parts of SBS. Nearer to the coast, however, over depths shallower than 40 m the energy pattern does follow the bathymetric contours after a considerable drop of wave energy caused by bottom friction.

Based on these results, we suggest the 40 m depth as the present day mean wave base and consequently the lower limit of the present SBS shoreface. In this sense, we can also state that the general absence of the finer sediments near the coast acts then like a proxy of the elevated wave shear stress exerted by the fluid on the bottom and thus corroborates with the definition of the 40 m isobath as the present lower limit of the SBS shoreface.

In the four maps of long-term mean sig. wave height over the SBS, as obtained with our SWAN model results from the four experiments on the higher-resolution curvilinear coastal grid, it is possible to see this considerable drop of wave energy over depths shallower than 40 m with the energy pattern approximately following the bathymetric contours. The increased resolution, however, allowed us to recognize that the Polonio cape and especially the southern coastal projection are under lower mean wave energy than the Santa Marta cape and the northern coastal projection, in a more direct relation with the local shoreface width.

The four maps of long-term mean relative sig. wave height over the SBS then addressed the proper significance of the mean wave height obtained and made clear the geomorphological separation between the huge lower shoreface and the greater declivities of the tiny upper shoreface and the Albardão ridge.

While offshore mean wave power showed a small and smooth northward decrease, the upper shoreface mean wave power, on the contrary, varies abruptly decreasing from the half north to the half south points, in a clear response to offshore mid-shelf declivities. This is because during higher-energy events considerable bottom friction may occur way offshore making the energy of those waves to decrease differentially between the northern and southern portions

of the mid-shelf, thus affecting the shoreface widths and also the mean wave power at upper shoreface.

This finding corroborates the previous statement that the mean energy of the waves reaching the upper shoreface of the SBS appears to be inversely proportional to shoreface width. This lead us to the important conclusion that the geological inheritance expressed through the shoreface width and the offshore mid-shelf declivities might indeed most times be more important to generate wave variability than the offshore wave power along-shelf variations itself.

The more remarkable finding, however, was the almost full refraction observed between the previous found bimodal offshore spectra and these upper shoreface spectra that were mostly found as ESE/SSE waves with increased SE wave importance and in an almost unimodal spectra, which is in absolute accordance with the local wave measurements. These results showed how the large and shallow SBS shoreface is responsible for an intense refraction of the waves (over 45°), thus forcing them to approach the beach system with very small angles of attack (< 10°) in relation to the shore normal.

Additionally, the similarity between the long-term mean power spectra of upper shoreface points facing SSE, which present a clear focus of SSE waves and almost none ESE wave power, together with the similarity between the power spectra of upper shoreface points facing ESE, where the more energetic SSE waves are absent and the ESE wave power is enhanced, indicated the sheltering effect caused by the capes and coastal projections.

We strongly believe that this phenomenon is caused by a windowing on the wave propagation until the shore. Once the greater is the refraction the greater is also the travelled distance of the wave, the immediate consequence is that shore normal waves reach the coast with higher energy than angled incoming waves.

The final consequence is that at the spaces between capes and coastal projections, where lower wave energies were found, there is a remarkable north/south asymmetry with higher energies to the north because of this refraction windowing. Implications for coastal evolution will be dealt with in a future experiment, but this north/south asymmetry pattern closely fits the relative positioning of the different types of Holocene coastal barriers, as described in Dillenburg et al. (2009).

Altogether, it is possible to state that bottom friction plays a major role on wave differentiation along the SBS shoreface either by acting over different amounts of refraction or by acting over the different shoreface widths. In this sense, these results allow us to define the shoreline orientation, the shoreface width and the offshore mid-shelf declivities as the key factors determining the wave power spectra that ultimately reach the shore of the SBS.

Chapter 5

Conclusion

The general patterns of the SBS wave climate could indeed be successfully determined here with the use of numerical models, allowing the quantification of the wave gradients over the SBS and the argumentation about the reasons of their existence.

In this sense, unlike initially hypothesized, the large-scale wave energy gradients over the SBS do not seem to be direct related to divergences or convergences respectively due to coastal concave or convex geometry but rather seem related to the attenuation by bottom friction, either by acting over different amounts of refraction or by acting over the different shoreface widths. Hence, the shoreline orientation, the shoreface width and the offshore mid-shelf declivities were defined here as the key factors determining the wave power spectra that ultimately reach the shore of the SBS.

Nonetheless, due to intense interannual power changes of the waves generated by the synoptic-scale eastward moving high and the mean South Atlantic subtropical high, one simple condition or period that could be used as a climatological field on geological time scale modeling efforts could not be achieved. Up to here, our results indicate the necessity for the use of at least two periods in order to represent the ENSO variability.

This work, therefore, is thought as a first step toward understanding the present SBS wave climate variability and its impacts on the coastal evolution. Future works shall achieve a better model validation skill and a sediment transport model is currently under implementation using the wave results obtained here.

Chapter 6

References

- Almeida, L. E. S. B.; Rosauro, N. L.; Toldo Jr., E. E. e Gruber, N. L. S. (1999): Avaliação da profundidade de fechamento para o litoral norte do Rio Grande do Sul. XIII Simpósio Brasileiro de Recursos Hídricos, Belo Horizonte, 11p.
- Ambrizzi, T. and Hoskins, B. J. (1997): Stationary Rossby wave propagation in a baroclinic atmosphere. Q. J. Royal Meteorological Society, 123, 919-928.
- Ambrizzi, T.; Hoskins, B. J. and Hsu, H. H. (1995): Rossby wave propagation and teleconnection patterns in the austral winter. J. Atmospheric Sciences, 52, 3661-3672.
- Andrade, K. (2005): Climatologia e comportamento dos sistemas frontais sobre a América do Sul. Dissertação de Mestrado em Meteorologia, Instituto Nacional de Pesquisas Espaciais, Brasil, 187 pp.
- Angulo, R. J.; Giannini, P. C. F.; Suguio, K. and Pessenda, L. C. R. (1999): Relative sea-level changes in the last 5500 years in southern Brazil (Laguna-Imbituba region, Santa Catarina State) based on vermetid 14C ages. Marine Geology, 159, 323-339.
- Angulo, R. J.; Lessa, G. C. and Souza, M. C. (2006): A critical review of the Mid-to-Late Holocene sea-level fluctuations on the eastern Brazilian coastline. Quaternary Science Reviews, 25(5), 486-506.
- Araujo, C. E. S.; Franco, D.; Melo, E. and Pimenta, F. M. (2003): Wave Regime Characteristics of the Southern Brazilian Coast, Proc. COPEDEC VI, Colombo, Sri Lanka.
- Barletta, R. C. (2000): Efeito da interação oceano-atmosfera sobre a morfodinâmica das praias do litoral central do Rio Grande do Sul, Brasil. Dissertação de mestrado, Fundação Universidade Federal de Rio Grande (FURG), 134 p.

- Berbery, E. H.; Nogués-Paegle, J. and Horel, J. D. (1992): Wavelike Southern Hemisphere extratropical teleconnections. J. Atmospheric Sciences, 49, 155-177.
- Birkemeier, W. A. (1985): Field Data on Seaward Limit of Profile Change. Journal of Waterway, Port, Coastal and Ocean Engineering, 111 (3): 598-602.
- Bjornsson, H. and Venegas, S. A. (1997): A manual for EOF and SVD analyses of climate data. McGill University, CCGCR Report 97-1, 52 pp.
- Booij, N.; Ris, R. C. and Holthuijsen, L. H. (1999): A third generation wave model for coastal regions. Part 1: Model description and validation. J. Geophys. Res., 104 (C4), 7649-7666.
- Calliari, L. J. and Klein, A. H. F. (1993): Características morfodinâmicas e sedimentológicas das praias oceânicas entre Rio Grande e Chuí, RS. Pesquisas, 20(1), 48-56.
- Calliari, L.J.; Tozzi, H.A.M. and Klein, A.H.F. (1998): Beach morphology and coastline erosion associated with storm surges in southern Brazil Rio Grande to Chuí, RS. Anais da Academia Brasileira de Ciências, 70 (2), 231-247.
- Campetella, C. M. and Vera, C. S. (2002): The influence of the Andes Mountains on the South American low-level flow. Geophys. Res. Lett., 29, 1826.
- Carvalho, L. M. V.; Jones, C. and Liebmann, B. (2004): The South Atlantic convergence zone: Intensity, form, persistence and relationships with intraseasonal to interannual activity and extreme rainfall. J. Climate, 17, 88-108.
- Carvalho, L. M. V; Jones, C. and Silva Dias, M. A. F. (2002): Intraseasonal large-scale circulations and mesoscale convective activity in tropical South America during TRMM-LBA campaign. Journal of Geophysical Research, 107(D20), 9-19.
- Casarin, D. P. and Kousky, V. E. (1986): Anomalias de precipitação no sul do Brasil e variações na circulação atmosférica. Revista Brasileira de Meteorologia, 01, 83-90.
- Cavalcanti, I. F. A. and Kousky, V. E. (2009): Frentes frias sobre o Brasil. In: Cavalcanti, I. F. A.; Ferreira, N. J.; Justi da Silva, M. G.; Silva Dias, M. A. F. (eds), Tempo e Clima no Brasil, Ed. Oficina de Textos, São Paulo, Ch. 9, 353-374.
- Corrêa, I. C. S; Martins, L. R. S.; Ketzer, J. M. M.; Elias, A. R. D. e Martins, R. (1996): Evolução sedimentológica e paleogeográfica da plataforma continental sul e sudeste do Brasil. Notas Técnicas, CECO/UFRGS, 9: 51-61.
- Cuchiara, D. C.; Fernandes, E. H. L; Strauch, J. C.; Winterwerp, J. C. and Calliari, L. J. (2009): Determination of the wave climate for the southern Brazilian shelf. Continental Shelf Res., 29, 545-555.

- Dean, R. G. and Dalrymple, R. A. (1991): Water Wave Mechanics for Engineers and Scientists. World Scientific, Singapore, 353 pp.
- Dillenburg, S. R.; Barboza, E. G.; Tomazelli, L. J.; Hesp, P. A.; Clerot, L. C. P. and Ayup-Zouain, R. N. (2009): The Holocene coastal barriers of Rio Grande do Sul. In: Dillenburg, S. R. andHesp, P. A. (eds), Geology and Geomorphology of Holocene Coastal Barriers of Brazil. Lecture Notes in Earth Sciences, Springer, Berlin, 107, 53-91.
- Dillenburg, S. R.; Tomazelli, L. J. and Clerot, L. C. P. (2003): Gradients of wave energy as the main factor controlling the evolution of the coast of Rio Grande do Sul in southern Brazil during the Late Holocene. In: Proceedings of the 5th International Symposium on Coastal Engineering and Science of Coastal Sediment Process. New York. American Society of Civil Engineers.
- Dragani, W.; Cerne, B.; Campetella, C.; Possia, N. and Campos, M. I. (2013): Synoptic patterns associated with the highest wind-waves at the mouth of the Río de la Plata estuary. Dynamics of Atmospheres and Oceans, 1-13.
- Dragani, W.; Garavento, E.; Simionato, C.; Nuñez, M.; Martín, P. and Campos, M.I. (2008): Wave simulation in the outer Río de la Plata estuary: an evaluation of SWAN model. J. Waterw. Port Coastal Ocean Eng. 134 (5), 299-305.
- Fachin, S. (1998): Caracterização do Perfil de Equilíbrio da Antepraia na costa do Rio Grande do Sul. Dissertação de Mestrado, UFRGS, Porto Alegre, 114 p.
- Figueiredo Jr, A. G. e Tessler, M. G. (2004): Topografia e composição do substrato marinho da região Sudeste-Sul do Brasil. Série Documentos REVIZEE/SCORE SUL. Instituto Oceanográfico USP. 64 pp.
- Figueroa, S. N.; Satyamurty, P. and Silva Dias, P. L. (1995): Simulations of the summer circulation over the South American region with an ETA coordinate model. J. Atmospheric Sciences, 52, 1573-1584.
- Gan, M. A. (1992): Ciclogêneses e Ciclones sobre a América do Sul. Tese de Doutorado em Meteorologia, Instituto Nacional de Pesquisas Espaciais (INPE), 225 pg.
- Gan, M. A. and Rao, B. V. (1991): Surface cyclogenesis over South America. Monthly Weather Review, 119, 1293-1302.
- Gan, M. A. and Rao, V. B. (1994): The influence of the Andes Cordillera on transient disturbances. Monthly Weather Review, 122, 1141-1157.
- Gandu, A. W. and Silva Dias, P. L. (1998): Impact of tropical heat sources on the South American tropospheric circulation and subsidence. J. Geophysical Research, 103 (D6), 6001-6015.

- Garreaud, R. D. (2000): Cold air incursions over Subtropical and Tropical South America: mean structure and dynamics. Monthly Weather Review, 127, 2823-2853.
- Garreaud, R. D. and Aceituno, P. (2007): Atmospheric circulation over South America: Mean features and variability. In: The Physical Geography of South America. T. Veblen, K. Young and A. Orme (eds). Oxford University Press.
- Gruber, N. L. S.; Toldo Jr., E. E.; Barboza, E. G. and Nicolodi, J. L. (2003): Equilibrium beach and shoreface profile of Rio Grande do Sul coast south of Brazil. Journal of Coastal Research, SI 35, 253-259.
- Guimarães, P. V.; Farina, L. and Toldo, E. E. (2014): Analysis of extreme wave events in the southern coast of Brazil Nat. Hazards Earth Syst. Sci. Discuss., 2, 4363-4391.
- Hallermeier, R.J. (1981a): Seaward Limit of Significant Sediment Transport by Waves: An Annual Zonation for Seasonal Profiles. CETA 81-2, U.S. Army Corps of Engineers, Coastal Engineering Research Center, Fort Belvoir, VA.
- Hallermeier, R.J. (1981b): A Profile Zonation for Seasonal Sand Beach from Wave Climate. Coastal Engineering, 4: 253-277.
- Hashimoto, N. (1997): Analysis of the directional wave spectra from field data. Advances in Coastal and Ocean Engineering, v.3. Liu, P.L-F. (ed.). World Scientific, Singapore, 103-143.
- Hendon, H. H.; Wheeler, M. and Zhang, C. (2007): Seasonal dependence of the MJO-ENSO Relationship. J. Climate, 20, 531-543.
- Hendon, H. H.; Zhang, C. and Glick, J. (1999): Interannual variation of the Madden-Julian oscillation during austral summer. J. Climate, 12, 2538-2550.
- Herdies, D. L.; Silva, A.; Silva Dias, M. A. and Nieto-Ferreira, R. (2002): Moisture budget of the bimodal pattern of the summer circulation over South America. J. Geophys. Research, 107, 8075.
- Hoell, A.; Barlow, M.; Wheeler, M. C. and Funk, C. (2014): Disruptions of El Niño-Southern Oscillation Teleconnections by the Madden-Julian Oscillation. Geophys. Res. Letters, 41, doi:10.1002/2013GL058648.
- Hoskins, B. J. and Ambrizzi, T. (1993): Rossby wave propagation on a realistic longitudinally varying flow. J. Atmospheric Sciences, 50, 1661-1671.
- Hoskins, B. J. and Hodges, K. I. (2005): A New Perspective on Southern Hemisphere Storm Tracks. J. Climate, 18, 4108-4129.

- Ingle, J. C. (1966): The Movement of Beach Sand: An Analysis Using Fluorescent Grains. Developments in Sedimentology, v. 5. Amsterdam. Elsevier.
- Jones, C. and Carvalho, L. M. V. (2002): Active and break phases in the South American monsoon system. Journal of Climate, 15, 905-914.
- Kalnay, E.; Kanamitsu, M.; Kistler, R.; Collins, W.; Deaven, D.; Gandin, L.; Iredell, M.; Saha, S.; Woollen, J.; Zhu, Y.; Chelliah, M.; Ebisuzaki, W.; Higgins, W.; Janowiak, J.; Mo, K.C.; Ropelewski, C.; Wang, J; Leetmaa, A; Reynolds, R.; Jenne, R. and Joseph, D. (1996): The NCEP-NCAR 40 year reanalysis project. Bulletin of the American Meteorological Society, 77, 437-471.
- Kessler, W. S. (2001): EOF representations of the Madden-Julian oscillation and its connection with ENSO. J. Climate, 14, 3055-3061.
- Kessler, W. S. and Kleeman, R. (2000): Rectification of the Madden-Julian Oscillation into the ENSO cycle. J. Climate, 13, 3560-3575.
- Kodama, Y-M. (1992): Large-scale common features of sub-tropical precipitation zones (the Baiu Frontal Zone, the SPCZ, and the SACZ). Part I: characteristics of subtropical frontal zones. J. Meteorological Society of Japan, 70, 813-835.
- Kodama, Y-M. (1993): Large-scale common features of sub-tropical precipitation zones (the Baiu Frontal Zone, the SPCZ, and the SACZ). Part II: Conditions of the circulations for generating the STCZs. J. Meteorological Society of Japan, 71, 581-610.
- Komar, P. D. (1998): Beach Processes and Sedimentation. 2nd edition. New Jersey, Prentice Hall, 544 pp.
- Komen, G. J.; Cavaleri, L.; Doneland, M.; Hasselmann, K.; Hasselmann, S. and Janssen, P. A.E. M. (1994): Dynamics and Modelling of Ocean Waves. Cambridge University Press, 532 pp.
- Lau, W. K. M. (2005): El Niño Southern Oscillation connection. In: Intraseasonal Variability in the Atmosphere-Ocean Climate System, W. K. M. Lau and D. E. Waliser (eds.), Praxis Publishing, 271-300.
- Liebmann, B. and Mechoso, C. R. (2011): The South American Monsoon System. In: The Global Monsoon System: Research and Forecast. Chang, C P.; Y. Ding; N. C. Lau; R. H. Johnson; B. Wang and T. Yasunari (eds.). World Scientific Series on Asia-Pacific Weather and Climate, v 5, World Scientific Publication Company, 608 pp.
- Liebmann, B.; Kiladis, G. N.; Marengo, J. A.; Ambrizzi, T. and Glick, J. D. (1999): Submonthly

- convective variability over South America and the South Atlantic convergence zone. J. Climate, 12, 1877-1891.
- Madden, R. A. and Julian, P. R. (1994): Observations of the 40-50 day tropical oscillation A review. Monthly Weather Review, 122, 814-837.
- Marengo, J. A.; Ambrizzi, T.; Kiladis, G. and Liebmann, B. (2002): Upper-air wave trains over the Pacific Ocean and wintertime cold surges in tropical-subtropical South America leading to freezes in southern and southeastern Brazil. Theoretical and Applied Climatology, 73, 223-242.
- Marengo, J. A.; Liebmann, B.; Grimm, A. M.; Misra, V.; Silva Dias, P. L.; Cavalcanti, I. F. A.; Carvalho, L. M. V.; Berbery, E. H.; Ambrizzi, T.; Vera, C. S.; Saulo, A. C.; Nogues-Paegle, J.; Zipser, E.; Seth, A. and Alves, L. M. (2010): Review Recent developments on the South American monsoon system. International Journal of Climatology.
- Marengo, J. A.; Soares, W. R.; Saulo, A. C. and Nicolini, M. (2004): Climatology of the low level jet east of the Andes as derived from the NCEP-NCAR reanalysis: Characteristics and temporal variability. J. Climate, 17, 2261-2280.
- Marshall, J. and Plumb, R. A. (2008): Atmosphere, ocean and climate dynamics: an introductory text. International Geophysics Series, v. 93, Elsevier Academic Press, 319 pp.
- Martinho, C. T.; Dillenburg, S. R. and Hesp, P. A. (2009): Wave energy and longshore sediment transport gradients controlling barrier evolution in Rio Grande do Sul, Brazil. Journal of Coastal Research, 25, 285-293.
- Martins, L. R. (1967): Aspectos texturais e deposicionais dos sedimentos praiais e eólicos da Planície Costeira do Rio Grande do Sul. Publicação especial 13. UFRGS, Brazil, 100 pp.
- Martins, L. R. and Corrêa, I. C. (1996): Morphology and Sedimentology of Southwest Atlantic Coastal Zone and Continental Shelf from Cabo Frio (Brazil) to Peninsula Valdez (Argentina). UNESCO/MCT/CPRM Publication. Porto Alegre, Brazil, 74 pp.
- Martins, L. R. e Urien, C. M. (1977): Atlas sedimentológico da Plataforma Continental do Rio Grande do Sul. Série Mapas, CECO/UFRGS.
- May, J. P. and Tanner, W. F. (1973): The littoral power gradient and shoreline changes. In: Coates, D. R. (ed.), Publications in Geomorphology. Binghamton. State University of New York, 43-60.
- McPhaden, M. J.; Zhang, X.; Hendon, H. H. and Wheeler, M. C. (2006): Large scale dynamics and MJO forcing of ENSO variability, Geophys. Res. Lett., 33, L16702, doi:10.1029/2006GL026786.

- Mo, K. C. (2000): Relationships between low-frequency variability in the Southern Hemisphere and sea surface temperature anomalies. J. Clim., 13, 3599-3620.
- Mo, K. C. and Paegle, J. N. (2001): The Pacific-South American modes and their downstream effects. International Journal of Climatology, 21, 1211-1229.
- Moon, J.-Y.; Wang, B. and Ha, K.-J. (2011): ENSO regulation of MJO teleconnection, Clim. Dyn., 37(5), 1133-1149, doi:10.1007/s00382-010-0902-3.
- Müller, G. V. and Ambrizzi, T. (2007): Teleconnection patterns and Rossby wave propagation associated to generalized frosts over southern South America. Clim. Dyn. 29, 633-645.
- Müller, G. V. and Ambrizzi, T. (2010): Rossby wave propagation tracks in southern hemisphere mean basic flows associated to generalized frosts over southern South America. Atmósfera, 23(1), 25-35.
- Murray, R. J. and Simmonds, I. (1991a): A numerical scheme for tracking cyclone centers from digital data. Part I: Development and operation of the scheme. Aust. Meteor. Mag., 39, 155-166.
- Murray, R. J. and Simmonds, I. (1991b): A numerical scheme for tracking cyclone centers from digital data. Part II: Application to January and July general circulation model simulations. Aust. Meteor. Mag., 39, 167-180.
- Necco, G. V. (1982a): Behavior of the cyclonic vortices in the South American region during FGGE: Cyclogenesis. Meteorologica, 13, 7-20.
- Necco, G. V. (1982b): Behavior of the cyclonic vortices in the South American region during FGGE: Tracks and developments. Meteorologica, 13, 21-34.
- Nogués-Paegle, J. and Mo, K. C. (1997): Alternating wet and dry conditions over South America during summer. Mon. Weather Rev., 125, 279-291.
- Nogués-Paegle, J.; Byerle, L. A. and Mo, K. C. (2000): Intraseasonal modulation of South American summer precipitation. Mon. Weather Rev., 128, 837-850.
- Nogués-Paegle, J.; Mechoso, C. R.; Fu, R.; Berbery, E. H.; Chao, W. C.; Chen, T. C.; Cook, K.; Diaz, A. F; Enfield, D.; Ferreira, R.; Grimm, A. M.; Kousky, V.; Liebmann, B.; Marengo, J.; Mo, K.; Neelin, J.; Paegle, D J.; Robertson, A. W.; Seth, A.; Vera, C. S. and Zhou, J. (2002): Progress in Pan American CLIVAR research: Understanding the South American monsoon. Meteorologica, 27, 3-32.
- Paegle, J. (1998): A comparative review of South American low level jets. Meteorologica, 23, 73-81.

- Parise, C. K.; Calliari, L. J. and Krusche, N. (2009): Extreme storm surges in the south of Brazil: atmospheric conditions and shore erosion. Brazilian J. Oceanography, 57 (3), 175-188.
- Patterson, D. C. and Blair, R. J. (1983): Visually determined wave parameters. In: Sixth Australian Conference on Coastal and Ocean Engineering (Gold Coast), 151-155.
- Pezza, A. B. and Ambrizzi, T. (2003): Variability of Southern Hemisphere Cyclone and Anticyclone Behavior: Further Analysis. J. Climate, 16, 1075-1083.
- Reboita, M. S. (2008): Ciclones Extratropicais sobre o Atlântico Sul: Simulação Climática e Experimentos de Sensibilidade. Tese de Doutorado em Meteorologia, Instituto de Astronomia, Geofísica e Ciências Atmosféricas, IAG-USP, 359 pg.
- Ris, R. C.; Holthuijsen, L. H. and Booij, N. (1999): A third-generation wave model for coastal regions. Part 2: Verification. J. Geophys. Res., 104 (C4), 7667-7681.
- Rusu, E. (2011): Strategies in using numerical wave models in ocean/coastal applications. Journal of Marine Science and Technology, 19 (1), 58-75.
- Salio, P.; Nicolini, M. and Saulo, A. C. (2002): Chaco low-level jet events characterization during the austral summer season. J. Geophysical Research, 107, 4816.
- Saraiva, J. M. B.; Bedran, C. and Carneiro, C. (2003): Monitoring of storm surges at Cassino Beach. J. Coastal Res., SI 35, 323-331.
- Satyamurty, P.; Ferreira, C. C. and Gan, M. A. (1990): Cyclonic Vortices over South América. Tellus, 42A, 194-201.
- Saulo, A. C.; Nicolini, M. and Chou, S. C. (2000): Model characterization of the South American low-level flow during the 1997-1998 spring-summer seasons. Climate Dynamics, 16, 867-881.
- Saulo, C.; Ruiz, J. and Skabar, Y. G. (2007): Synergism between the Low-Level Jet and organized convection in its exit region. Mon. Wea. Rev., 135, 1310-1326.
- Seluchi, M. E.; Garreaud, R. D.; Norte, F. A. and Saulo, A. C. (2006): Influence of the subtropical Andes on Baroclinic Disturbances: A cold-front case study. Monthly Weather Review, 134, 3317-3335.
- Silva Dias, P. L. (2000): The role of latent heat release in the dynamics of the LLJs along the Andes. Preprints, Sixth Int. Conf. on Southern Hemisphere Meteorology and Oceanography, Santiago, Chile, Amer. Meteor. Soc., 163-164.

- Silvestri, G. E. and Vera, C. S. (2003): Antarctic Oscillation signal on precipitation anomalies over southeastern South America, Geophys. Res. Lett., 30(21), 2115, doi:10.1029/2003GL018277.
- Simmonds, I. and Keay, K. (2000a): Variability of Southern Hemisphere Extratropical Cyclone Behavior, 1958 1997. J. Climate, 13, 550-561.
- Simmonds, I. and Keay, K. (2000b): Mean Southern Extratropical Cyclone Behavior in the 40-Year NCEPNCAR Reanalysis. J Climate, 13, 873-885.
- Sinclair, M. R. (1994): An Objective Cyclone Climatology for the Southern Hemisphere. Monthly Weather Review, 122, 2239-2256.
- Sinclair, M. R. (1995): A climatology of cyclogenesis for the Southern Hemisphere. Monthly Weather Review, 123, 1601-1619.
- Sinclair, M. R. (1997): Objective Identification of Cyclones and Their Circulation Intensity and Climatology. Weather and Forecasting, 12, 595-612.
- Souza, E. B. and Ambrizzi, T. (2006): Modulation of the intraseasonal rainfall over tropical Brazil by the Madden-Julian Oscillation. Int. J. Climatol., 26 (13), 1759-1776.
- Strauch, J. C. (2001): Caracterização do Estado do Mar em Rio Grande. XIV Simpósio Brasileiro de Recursos Hídricos, Aracajú, SE.
- Strauch, J. C.; Cuchiara, D. C.; Toldo Jr., E. E. e Almeida, L. E. S. B. (2009): O Padrão das Ondas de Verão e Outono no Litoral Sul e Norte do Rio Grande do Sul. Revista Brasileira de Recursos Hídricos, 14 (4), 29-37.
- Taljaard, J. J. (1967): Development, distribution and movement of cyclones and anticyclones in the Southern Hemisphere during IGY. J. Appl. Meteor., 6, 973-987.
- Tang, Y. and Yu, B. (2008): MJO and its relationship to ENSO. J. Geophys. Res., 113, D14106, doi:10.1029/2007JD009230.
- Thompson, D. W. J. and Wallace, J. M. (2000): Annular modes in the extratropical circulation. Part I: month-to-month variability. J. Clim., 13, 1000-1016.
- Toldo Jr., E. E.; Nicolodi, J. L.; Almeida, L. E. S. B.; Corrêa, I. C. S. and Esteves, L. S. (2006): Coastal Dunes and Shoreface Width as a Function of Longshore Transport. Journal of Coastal Research, SI-39, 390-394.
- Tolman, H. L. (2002): User manual and system documentation of WAVEWATCH-III version 2.22. NOAA / NWS / NCEP / MMAB Tech. Note 222, 133 pp.

- Tolman, H. L.; Balasubramaniyan, B.; Burroughs, L. D.; Chalikov, D. V.; Chao, Y. Y.; Chen, H. S. and Gerald, V. M. (2002): Development and implementation of wind generated ocean surface wave models at NCEP. Weather and Forecasting, 17, 311-333.
- Tomazelli, L.J.; Dillenburg, S.R. and Villwock, J.A. (2000): Late Quaternary geological history of Rio Grande do Sul coastal plain, southern Brazil. Revista Brasileira de Geociências, 30(3), 474-476.
- Tucker, M. J. and Pitt, E. G. (2001): Waves in ocean engineering. Ocean engineering book series, v. 5. Elsevier, Amsterdam, 521 p.
- van Loon, H. A. (1965): Climatological Study of the Atmospheric Circulation in the Southern Hemisphere during the IGY, Part I: July 1957 31 March 1958. J. Appl. Meteor., 4, 479-491.
- Vera, C. S.; Vigliarolo, P. K. and Berbery, E. H. (2002): Cold season waves over subtropical South America. Monthly Weather Review, 130, 684-699.
- Vera, C.; Higgins, W.; Amador, J.; Ambrizzi, T.; Garreaud, R. D.; Gochis, D.; Gutzler, O. D.; Lettenmaier, D.; Marengo, J.; Mechoso, C.; Nogues-Paegle, J.; Silva Diaz, P.L. and Zhang, C. (2006): Towards a unified view of the American Monsoon System. Journal of Climate, 19, 4977-5000.
- Villwock, J. A.; Tomazelli, L. J.; Loss, E. L.; Dehnhardt, E. A.; Horn Filho, N. O.; Bachi, F. A. and Dehnhardt, B. A. (1986): Geology of the Rio Grande do Sul Coastal Province. Quaternary of South America and Antarctic Peninsula, 04, 79-97.
- Wainer, I. J. (1963): Relatório Técnico Análise e Previsão das Alturas de Onda em Tramandaí. UFRGS, Instituto de Pesquisas Hidráulicas, IPH, Porto Alegre, 30 p.
- Zhang, C. (2005): Madden-Julian oscillations. Rev. Geophysics, 43, RG2003, 1-36.
- Zhou, J. and Lau, K. M. (1998): Does a monsoon climate exist over South America? Journal of Climate, 11, 1020-1040.